Numerical calculation of beam Coupling Impedances in Synchrotron Accelerators

Numerische Berechnung von Strahlkoppelimpedanzen in Synchrotronbeschleunigern
Zur Erlangung des akademischen Grades Doktor-Ingenieur (Dr.-Ing.)
genehmigte Dissertation von Dipl.-Ing. Lukas Hänichen aus Dresden
2016 — Darmstadt — D 17

TECHNISCHE
UNIVERSITÄT
DARMSTADT

Fachbereich Elektrotechnik und Informationstechnik
Institut für Theorie
Elektromagnetischer Felder (TEMF)

Numerical calculation of beam Coupling Impedances in Synchrotron Accelerators
Numerische Berechnung von Strahlkoppelimpedanzen in Synchrotronbeschleunigern

Genehmigte Dissertation von Dipl.-Ing. Lukas Hänichen aus Dresden

1. Gutachten: Prof. Dr.-Ing. Thomas Weiland
2. Gutachten: Prof. Dr.-Ing. Harald Klingbeil

Tag der Einreichung: 25.09.2015
Tag der Prüfung: 02.12.2015

Darmstadt — D 17

Bitte zitieren Sie dieses Dokument als:
URN: `urn:nbn:de:tuda-tuprints-53673`
URL: `http://tuprints.ulb.tu-darmstadt.de/5367/`

Kurzfassung

Strahlen geladener Teilchen sind in vielen Forschungsbereichen von Interesse, wie zum Beispiel der Teilchen- und Kernphysik, Materialwissenschaften, Medizin und vielen mehr. In Synchrotronbeschleunigern wird die Beschleunigungsstrecke zyklisch durchlaufen. Eine Teilchenbahn mit konstantem Radius wird erreicht, indem die Frequenz des beschleunigenden elektrischen Feldes und die Amplitude des magnetischen Feldes synchron erhöht werden. Ein Synchrotron besteht demnach aus einer ringförmigen Anordnung verschiedener Komponenten entlang des Strahlverlaufs, die der Beschleunigung und Führung des Teilchenstrahls dienen. Für die einwandfreie Funktion einer solchen Anlage muss sichergestellt werden, dass die Teilchen einer kontrollierten Bewegung entlang vordefinierter Bahnen folgen. Die Erfüllung der entsprechenden Stabilitätskriterien steht unter Anderem im Zusammenhang mit den sogenannten Strahlkoppelimpedanzen, welche eine wichtige Zielgröße für kollektive Effekte in Synchrotronbeschleunigern darstellen.

Diese Arbeit befasst sich mit analytischen und numerischen Methoden zur Berechnung der Strahlkoppelimpedanzen. Eines der Ziele ist dabei, die Elektrodynamik geladener Teilchenstrahlen besser zu verstehen, ihre mathematische Beschreibung im Zeit- und Frequenzbereich zu rekapitulieren, und den Zusammenhang zwischen physikalischer Realität und numerischer Simulation herzustellen. Analytische Methoden sind in der Regel auf symmetrische Geometrien beschränkt und können daher allenfalls der Abschätzung von Feldverteilungen in real existierenden Baugruppen oder der Validierung bestimmter Simulationsmethoden dienen. Letzten Endes lassen sich genauere Prognosen nur mit Hilfe räumlicher Simulationsmodelle machen.

Numerische Berechnungsmethoden zur Simulation geladener Teilchenstrahlen haben sich in der zweiten Hälfte des letzten Jahrhunderts etabliert und den Bau großer Teilchenbeschleuniger begleitet. Dabei kamen vor allem klassische Wakefield-Simulationen zum Einsatz, wobei der tatsächliche zeitliche Bewegungsablauf geladener Teilchen in der Simulation nachgebildet wird. Für den hier vorliegenden Fall eines Schwerionensynchrotrons sind auch Teilchengeschwindigkeiten von Bedeutung, die signifikant niedriger sind als die Lichtgeschwindigkeit im Vakuum und wo die häufig angewandte ultrarelativistische Näherung nicht immer praktikabel ist.

Ferritbasierte Kickermagnete, die zur abrupten Auslenkung des Teilchenstrahls benötigt werden, tragen durch die Hystereseigenschaft des Ferritmaterials zur Koppelimpedanz bei. Um die Rückwirkung auf den passierenden Teilchenstrahl abzuschätzen, müssen die Koppelimpedanzbeiträge berechnet werden.

Nach Einführung einiger wichtiger mathematischer Beziehungen und Vorstellung zweier Berechnungsverfahren werden Referenzgeometrien betrachtet, deren Koppelimpedanzbeiträge sich mit den Methoden der klassischen Feldtheorie berechnen lassen. Nachdem gezeigt wurde, dass die analytisch und numerisch gewonnenen Ergebnisse im Einklang stehen, werden anschließend Simulationsmodelle benutzt, die sich an realen Baugruppen des FAIR (Facility for Antiproton and Ion Research GmbH) SIS100 Synchrotronbeschleunigers orientieren.

Abstract

Beams of charged particles are of interest in various fields of research including particle and nuclear physics, material and medical science and many more. In synchrotron accelerators the accelerating section is passed periodically. A closed loop trajectory is enforced, by increasing the frequency of the accelerating electric field and the magnitude of the dipolar magnetic guide field synchronously. A synchrotron therefore consists of a circular assembly of various beamline elements which serve the purposes of accelerating and guiding the particle beam. For the flawless operation of such a machine it has to be assured that the particles perform a controlled motion along predefined trajectories. Amongst others, the fulfillment of the corresponding stability criteria is in close conjuction with the so-called beam coupling impedances which are an important figure of merit for collective effects in synchrotron accelerators.

This work focuses on analytical and numerical methods for the calculation of beam coupling impedances. One of the primary objectives is to gain a better understanding of the electrodynamics related to charged particle beams, furthermore to recapitulate the mathematical description of charged particle beams in both time and frequency domain and finally establish the links between actual physics and numerical modeling. Analytical methods are usually restricted to symmetrical geometry and may solely serve for the approximate determination of the field distribution in real geometries or to validate certain numerical methods. More accurate prognosis is only possible with three-dimensional simulation models.

Numerical simulation techniques have been established in the second half of the last century accompanying the evolution of many particle accelerators. Classical time domain codes were the prevailing simulation tools where the actual process of the particle motion sequence is reproduced. For the present case of a heavy ion synchrotron accelerator, particle velocities significantly lower than the speed of light occur and the commonly applied ultra-relativistic limit case may no longer be practicable.

Ferrite-loaded kicker magnets are commonly used to achieve abrupt changes of the beam direction of motion and contribute to the coupling impedance due to hysteresis properties of the ferrite material. These coupling impedance contributions must be determined in order to assess the feedback action on the traversing particles of the beam. After introducing important mathematical relations and presentation of two calculation methods, a few reference examples are discussed, which can be treated by means of the classical electromagnetic field theory.

After showing that the simulation results are in accordance with the corresponding analytical results, the focus is put on simulation models that represent actual components of the FAIR (Facility for Antiproton and Ion Research GmbH) SIS100 synchrotron accelerator.

Contents

1. Introduction **1**
- 1.1. Motivation 1
- 1.2. Application 3
- 1.3. Outline 3

2. Electrodynamics of Moving Charge **5**
- 2.1. Maxwell's Equations 5
- 2.2. Constitutive Equations 7
  - 2.2.1. Conductors 8
  - 2.2.2. Dielectrics 8
  - 2.2.3. Ferromagnets and Ferrimagnets 10
- 2.3. Poynting's theorem 12
- 2.4. Commonly used coordinate systems 14
- 2.5. Sources 16
- 2.6. Point charge in uniform motion 19
- 2.7. Inhomogenous wave equation 21

3. Wake Function and Coupling Impedance **23**
- 3.1. Prerequisites 24
- 3.2. Wake function 24
- 3.3. Coupling impedances 27
- 3.4. Consequences arising from the PANOFSKY-WENZEL theorem 28
- 3.5. Coupling impedances in synchrotron accelerators 30
- 3.6. Characterization of techniques for coupling impedance analysis . . . 31
  - 3.6.1. Analytical methods 31
  - 3.6.2. Numerical methods 32
  - 3.6.3. Experimental methods 33

4. Analytical methods for coupling impedance analysis **39**
- 4.1. Rotational-symmetric multi-layer problem 39
- 4.2. Rotational-symmetric half-space problem in the ultra-relativistic limit 47
- 4.3. Planar-symmetric half-space in the ultra-relativistic limit 52

5. Numerical methods for coupling impedance analysis 63
- 5.1. Simulation tools 63
- 5.2. Finite Integration Technique 65
- 5.3. Time domain analysis 70
  - 5.3.1. Rotational symmetry 76
  - 5.3.2. Planar symmetry 79
- 5.4. Frequency domain analysis 80
  - 5.4.1. Rotational symmetry 82
- 5.5. Conclusive remarks 83

6. Application: Coupling Impedance analysis for the SIS100 kicker system 85
- 6.1. The SIS100 kicker system 85
  - 6.1.1. Bipolar window frame kicker magnet 87
  - 6.1.2. Power supply 89
- 6.2. Mutual coupling 92
- 6.3. Coupling impedance contributions caused by the SIS100 kicker magnet 99
  - 6.3.1. Coupling Impedance contribution of a single kicker module with cuboid chamber in the ultra-relativistic limit. 99
  - 6.3.2. Coupling Impedance contribution of a single kicker module with cylindrical chamber in the ultra-relativistic limit. 103
  - 6.3.3. Coupling Impedance contribution of a single kicker module with cuboid chamber and moderate beam velocity. 105
- 6.4. Beam induced heating 107
- 6.5. Further applications 109

7. Conclusion 111

A. Deduction of source terms 113

B. Deduction of the inhomogenous wave equation 117

C. Solutions for cylindrical geometry 119

D. Transforms and identities 121
- D.1. FOURIER transform 121
- D.2. LORENTZ transform 122
- D.3. Selected properties of the (modified) BESSEL functions 123

E. Green function property of coupling impedances 125

F. Circuit analysis **127**

G. Bunch profile and bunch spectrum **131**

H. Datasheets **135**
H.1. Material specifications 135

I. Register **137**
Acronyms 137
Coordinate systems 139
Electrodynamics 139
General 140
Electrical Engineering 141
Wakefields and Coupling Impedances 143
Physical constants 143
Computational Electrodynamics FIT notation 144

1 Introduction

Charged particle beams have been of interest for various fields of research including particle and nuclear physics, material and medical science and many more. Experiments which employ a special apparatus to accelerate charged particles date back almost 100 years. To overcome the limitations of electrostatic acceleration, machines which use alternating electric fields have been developed. In recirculating accelerators the accelerating section is passed multiple times. A dipolar magnetic field can be used to enforce a spiral trajectory whereupon the radius increases proportionally with the kinetic energy of the particles. A closed loop trajectory of constant radius can be enforced, if the magnitude of the dipolar magnetic field and the frequency of the accelerating electric field are increased synchronously. This type of particle accelerator is therefore called synchrotron.

Such a synchrotron is a circular assembly of various beamline elements which are passed repeatedly during acceleration and storage of the particle beam. For reliable operation it has to be assured that the particles perform a controlled motion along predefined trajectories. Otherwise degradation or even loss of the particle beam may result which makes the machine unusable for research or even poses safety issues for its operation. The state of controlled motion is referred to as stable state. Since the construction of the first synchrotron accelerators in the 50s, observations have been made and stability criteria have been formulated.

The design of a synchrotron accelerator is a rather complex and multidisciplinary engineering task. The increased capabilities in computational electrodynamics allow for accurate design and investigation of possible issues prior to construction. This work focuses on analytical and numerical methods for the calculation of beam coupling impedances which are an important figure of merit for collective effects in synchrotron accelerators.

1.1 Motivation

A particle beam is accompanied by an Electromagnetic (EM) field. This *wakefield* depends on the beam parameters and the immediate environment which is given by the geometry and the material properties of the beamline elements. In the first place, the direct and the scattered field affect the motion of the particles and therefore the stability of the particle beam. In the second place, different loss mechanisms lead to heat deposition in beamline elements and affect machine integrity.

All particles perform oscillations with respect to a reference trajectory of an ideal particle, called the orbit. The oscillation can be decomposed into a transverse oscillation called *betatron oscillation* and a longitudinal oscillation called *synchrotron oscillation*. This state of controlled motion is continuously perturbed by the deflecting EM field which depends on the interplay of the particle beam and its immediate environment. These perturbations might lead to uncontrolled motion and must be described by appropriate means in order to verify the fulfillment of the stability criteria. The secondary effect is related to the dissipation of EM energy. The heat load may affect the operation of critical components such as superconducting cavities or magnets. Many of the earlier studies rely on the assumption of light particles such as electrons under highly relativistic conditions. But especially in the case of protons and heavy ions these mechanisms become important.

Both effects may be described through beam *coupling impedances* which may be determined by either analytical, numerical or experimental methods. The transverse and longitudinal case are treated separately and lead to the corresponding target figures of *longitudinal coupling impedance* and *transverse coupling impedance.* Apparently, a direct measurement of the deflecting EM field in the presence of a particle beam poses insuperable technical problems, such as access of the vacuum chamber and field probe design. Furthermore, any modification of the beamline geometry will impact the distribution of the deflecting field and modify the result significantly. By measuring the growth rate of stimulated instabilities, the total impedance of a synchrotron accelerator may be determined indirectly. However, it is difficult if not impossible to retrace certain impedance contributions to particular beamline elements. Bench measurement methods usually replace the particle beam with a wire. Doing so implies a change of the electrical properties and care must be taken during the interpretation of the results. The validity of such a transmissionline setup has been discussed controversially. Analytical methods are limited to very few geometries only, but are suitable to study basic principles and gain understanding of the actual physics. On the contrary, numerical methods are flexible with respect to geometry and limited mainly by computational cost.

Therefore analytical methods are used to complement and validate numerical methods. After studying selected examples an actual beamline device is studied which is connected with the synchrotron accelerator of the Facility for Antiproton and Ion Research GmbH (FAIR).

1.2 Application

The Helmholtz Center for Heavy Ion Research GmbH (GSI) is a member of the German HELMHOLTZ association and was founded in 1969 in order to combine the efforts of several research groups at a central facility. At present the UNIversal Linear ACcelerator (UNILAC) allows to inject protons and various types of heavy ions into the Heavy Ion Synchrotron (SIS)18. The SIS18 has a circumference of 216 m and a maximum magnetic rigidity of 18 Tm. For the international FAIR project the new synchrotron SIS100 is currently under construction, with a designated circumference of 1080 m and a maximum magnetic rigidity of 100 Tm. The bending magnets are conventional iron-dominated dipoles fitted with superconducting cable technology to cope with increased current demands in the windings. Several sections are operated around 10 K to act as cryo-adsorption pumps to maintain the vacuum. Both technologies are sensitive towards additional dissipation, since the coolant can only transport a certain amount of heat. Additional heating may violate the system specifications or put additional stress on certain components.
Not every component has reached its final design state. Certain components are expected to have significant impact on the coupling impedance and therefore beam stability. Numerical calculation of the coupling impedance is used to confirm, reveal, reduce and gain better understanding about beam interaction with its environment.

1.3 Outline

This thesis is structured as follows: The introductory chapter describes the motivation behind this work and familiarizes with the area of application after providing a summary of the historical development in the field of particle accelerators. In the second chapter the electromagnetic field quantities are introduced as well as the fundamental equations of classical electrodynamics. The third chapter deals with the description of collective effects by means of coupling impedances. The basic definitions are summarized and the connection between wakefields and coupling impedances is explained. The fourth chapter is devoted to coupling impedance calculation for selected examples by means of analytical methods. These examples are resumed by means of numerical methods in the fifth chapter after providing an overview on suitable computational methods. The sixth chapter is devoted to the calculation of the coupling impedance contributions of the fast extraction kicker system for the future SIS100 accelerator. The last chapter closes with a summary and conclusive remarks.

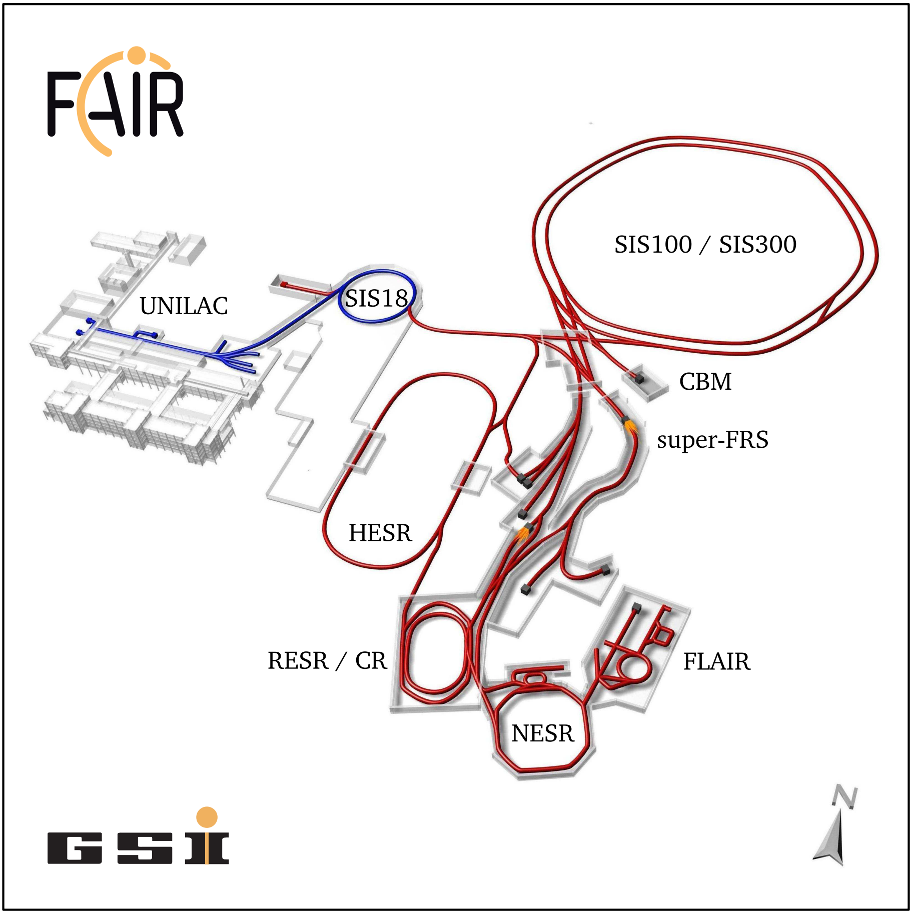

Figure 1.1.: The schematic shows the facility site of the GSI Helmholtzzentrum für Schwerionenforschung. The existing accelerator complex is marked in blue, while the extensions for the FAIR project are marked in red. The completion is scheduled for 2019.
The subject of interest are the collective effects caused by beam-induced electromagnetic fields in certain components of the synchrotron accelerators (SIS18 / SIS100 / SIS300). Graphics by courtesy of: GSI GmbH and FAIR GmbH.

2 Electrodynamics of Moving Charge

The total EM field occurring along the beamline of a particle accelerator as it is seen by a test particle, can be understood as a superposition of an externally applied guide field and the wakefield which is generated by the particle beam itself [Ng06]. The guide field mainly serves two purposes: The first purpose is to increase (or at least retain) the kinetic energy of the particles through acceleration. The second purpose is to enforce predefined trajectories for the particle beam.

$$\left\{ \begin{array}{c} \vec{E} \\ \vec{H} \end{array} \right\}_{total} = \left\{ \begin{array}{c} \vec{E} \\ \vec{H} \end{array} \right\}_{guide} + \left\{ \begin{array}{c} \vec{E} \\ \vec{H} \end{array} \right\}_{wake}$$

If the guide field does not change at all or changes slowly compared to the wakefield, it may be regarded as static and either field may be treated separately. The entire work focuses on the analysis of the second part therefore explicit marking will be abandoned.

2.1 Maxwell's Equations

The electric field is described by the electric field intensity $\vec{E}$ and the electric displacement (or electric flux density) $\vec{D}$. The magnetic field is described by the magnetic field intensity $\vec{H}$ and the magnetic induction (or magnetic flux density) $\vec{B}$, respectively. The distribution of sources is provided through the volume charge density q_V and the current density $\vec{J}$. All these quantities are connected through MAXWELL's equations which consist of FARADAY's law of induction, the generalized AMPERE's law and GAUSS' laws for the electric and magnetic field. In combination with the LORENTZ force equation (3.1a), this set of equations permits the mathematical treatment of all macroscopic phenomena in the sense of classical electrodynamics. In this order, the differential forms in Time Domain (TD) and Frequency Domain (FD) for linear media read [Jac99]:

$$\begin{array}{llr}
\textit{Time Domain} & \textit{Frequency Domain} & \\
\operatorname{curl}\vec{E}(\vec{r},t) = -\frac{\partial}{\partial t}\vec{B}(\vec{r},t) & \operatorname{curl}\underline{\vec{E}}(\vec{r},\omega) = -j\omega\underline{\vec{B}}(\vec{r},\omega) & (2.1a) \\
\operatorname{curl}\vec{H}(\vec{r},t) = \frac{\partial}{\partial t}\vec{D}(\vec{r},t) + \vec{J}(\vec{r},t) & \operatorname{curl}\underline{\vec{H}}(\vec{r},\omega) = j\omega\underline{\vec{D}}(\vec{r},\omega) + \underline{\vec{J}}(\vec{r},\omega) & (2.1b) \\
\operatorname{div}\vec{D}(\vec{r},t) = q_V(\vec{r},t) & \operatorname{div}\underline{\vec{D}}(\vec{r},\omega) = \underline{q}_V(\vec{r},\omega) & (2.1c) \\
\operatorname{div}\vec{B}(\vec{r},t) = 0 & \operatorname{div}\underline{\vec{B}}(\vec{r},\omega) = 0 & (2.1d)
\end{array}$$

The variable $\vec{r}$ denotes the position vector in the underlying coordinate system. If the arrow symbol is omitted, the absolute value is shown: $r = |\vec{r}|$. The variables t and ω mark the dependency on time and frequency respectively. In frequency domain, vectors are replaced by phasors and the derivative with respect to time is replaced by $j\omega$. Complex-valued quantities are marked with an underline. The underlying conventions for the Fourier transform are listed in Appendix D.1. For the sake of readability, certain dependencies such as t, ω and $\vec{r}$ will be omitted where it is self-explanatory.

The current density $\vec{J}$ can be split into three parts. The conduction current density $\vec{J}_\kappa$ is related to charge carriers that are bound to electric conductors while the convection current density $\vec{J}_\beta$ is related to unbound charge carriers which are subject to Coulomb or Lorentz forces. Finally the impressed current density $\vec{J}_\iota$ represents an externally forced flow of charge independent of Coulomb or Lorentz forces:

$$\vec{J} = \vec{J}_\kappa + \vec{J}_\beta + \vec{J}_\iota$$

with the conduction current density

$$\vec{J}_\kappa = \kappa\vec{E} \tag{2.2a}$$

and the convection current density

$$\vec{J}_\beta = \vec{v}q_V \tag{2.2b}$$

The charge carriers that contribute to the convection current move with the velocity v which is often expressed through the relative velocity β and the velocity of light in vacuum c_0.

$$v = \beta c_0$$

Another fundamental equation namely the continuity equation for charge is obtained by applying the divergence operator to equation 2.1b and substituting with the use of equation 2.1c:

$$0 = \frac{\partial}{\partial t} q_V + \operatorname{div} \vec{J} \tag{2.3}$$

The continuity equation relates the net current flow into a differential volume with the change of charge over time and therefore enforces the conservation of charge.

2.2 Constitutive Equations

A constitutive equation relates two physical quantities to account for the response of a medium towards an external force. In the case of electrodynamics this applies to the field intensities $\vec{E}$, $\vec{H}$ and the corresponding flux densities $\vec{D}$, $\vec{J}$, $\vec{B}$ which behave differently in media other than vacuum due to physical principles on sub-molecular level. The constitutive equations are as follows, including the polarization density $\vec{P}$ and magnetization $\vec{M}$ of the medium which in the most general case may depend on $\vec{r}$, t and $\vec{E}$, $\vec{B}$, respectively:

$$\vec{D} = \varepsilon_0 \vec{E} + \vec{P} \tag{2.4a}$$

$$\vec{H} = \frac{\vec{B}}{\mu_0} - \vec{M} \tag{2.4b}$$

(2.4c)

In engineering practice, the material parameters mostly appear in the shape of proportionality constants between two physical quantities [ITvM04] as phenomenological relations $\vec{D} = \varepsilon \vec{E}$, $\vec{B} = \mu \vec{H}$ and $\vec{J}_\kappa = \kappa \vec{E}$. For the following considerations isotropic and linear materials will be assumed. The entire volume shall be composed of subdomains which have a homogenous material distribution. Material parameters may in addition depend on environmental conditions such as aggregate state, temperature or pressure. If not stated otherwise these dependencies are neglected for the underlying conditions. In order to deal with different types of materials, the predominant macroscopic properties will be explained separately in the following.

2.2.1 Conductors

The electrical conductivity κ measures the ability to conduct an electrical current by allowing the circulation of charge carriers through the atomic lattice. It is the reciprocal of the resistivity and determines whether a particular material counts as a conductor, semiconductor or insulator. In the case of metallic conductors, the so-called conduction electrons allow the flow of electric current. Counteracting forces of the lattice determine the mobility of the charge carriers and cause energy loss. Metallic conductors show a linear relationship between current flow and voltage drop which is known as OHM's law. The equation $\vec{J}_\kappa = \kappa \vec{E}$ therefore is the representation of OHM's law in the context of field quantities. The scalar product of $\vec{E}$ and $\vec{J}_\kappa$ is directly related to the resistive losses P_κ:

$$P_\kappa = \int_V \vec{E} \cdot \vec{J}_\kappa dV \tag{2.5}$$

Material	Symbol	κ / Sm^{-1}
stainless steel	SS	1.4×10^6
aluminum	AL	38×10^6
copper	CU	59×10^6
perfect conductor	PEC	$\rightarrow \infty$

Table 2.1.: Commonly used materials for electric conductors and their electric conductivity.
The term perfect electric conductor is commonly used in the context of computational electrodynamics.

2.2.2 Dielectrics

Materials where the conductivity falls below 10^{-8} S/m are called dielectrics [ITvM04]. An external electric field may polarize the material by inducing temporary dipoles or through the alignment of permanental dipoles. The obtained degree of polarization, is described by the relative permittivity ε_r in reference to vacuum which has the permittivity ε_0 (relative permittivity $\varepsilon_\mathrm{r} = 1$):

$$\varepsilon(\vec{r}) = \varepsilon_0 \varepsilon_\mathrm{r}(\vec{r}) \tag{2.6}$$

The ability of the dipoles to follow the polarizing field is frequency-dependent. An alternating field results in a periodic change of polarization, which requires energy. These frequency-dependent dielectric losses can be included by introducing a complex-valued relative permittivity $\underline{\varepsilon}_\mathrm{r}$:

$$\underline{\varepsilon}_{\mathrm{r}}(\vec{r},\omega) = \varepsilon'_{\mathrm{r}}(\vec{r},\omega) - j\varepsilon''_{\mathrm{r}}(\vec{r},\omega) \tag{2.7}$$

The frequency domain representation of equation 2.1b can now be rearranged to:

$$\begin{aligned}
\operatorname{curl}\underline{\vec{H}}(\vec{r},\omega) &= \big(j\omega\varepsilon_0\underline{\varepsilon}_{\mathrm{r}}(\vec{r},\omega) + \kappa(\vec{r},\omega)\big)\,\underline{\vec{E}}(\vec{r},\omega) && (2.8)\\
&= j\omega\left(\varepsilon_0\left(\varepsilon'_{\mathrm{r}}(\vec{r},\omega) - j\varepsilon''_{\mathrm{r}}(\vec{r},\omega)\right) - j\frac{\kappa(\vec{r})}{\omega}\right)\underline{\vec{E}}(\vec{r},\omega) && (2.9)\\
&= j\omega\left(\varepsilon_0\varepsilon'_{\mathrm{r}}(\vec{r},\omega) - j\left(\varepsilon_0\varepsilon''_{\mathrm{r}}(\vec{r},\omega) + \frac{\kappa(\vec{r})}{\omega}\right)\right)\underline{\vec{E}}(\vec{r},\omega) && (2.10)\\
&= j\omega\underline{\varepsilon}(\vec{r},\omega)\underline{\vec{E}}(\vec{r},\omega) && (2.11)
\end{aligned}$$

Conveniently, the imaginary part of the complex permittivity in AMPERE's law is generalized for the combined dielectric and conductive losses. Depending on the frequency range certain materials may rather act as dielectric ($\kappa = 0$) or conductor ($\varepsilon'_{\mathrm{r}} = 1, \varepsilon''_{\mathrm{r}} = 0$) such that only one of the loss mechanisms is relevant at a time. The permittivity in GAUSS' law for the electric field relates the electric field with the electric displacement and must not be replaced with the generalized complex-valued permittivity if the imaginary part is related to conductive losses ($\underline{\vec{D}} = \varepsilon_0\underline{\varepsilon}_{\mathrm{r}}\underline{\vec{E}}$).

The resistive loss reads P_κ:

$$P_\kappa = \int\limits_V \frac{1}{2}\kappa\left|\underline{\vec{E}}\right|^2 dV \tag{2.12a}$$

and the spectral dielectric loss :

$$P_{\varepsilon,\omega} = \omega\int\limits_V \frac{1}{2}\varepsilon_0\varepsilon''_{\mathrm{r}}\left|\underline{\vec{E}}\right|^2 dV \tag{2.12b}$$

The average dielectric loss is determined through integration over a full period T. In the context of capacitive devices that employ dielectrics, these losses are sometimes referred to as *dielectric hysteresis* and *dielectric leakage*.

2.2.3 Ferromagnets and Ferrimagnets

All atoms have permanental magnetic dipole moments, whose magnitude and orientation depends on the electron configuration of the underlying compound [ITvM04]. The field enhancing property of ferromagnetic and ferrimagnetic materials originates from the spontaneous alignment of these dipole moments under the influence of an externally applied magnetic field. This property is used in accelerator components which serve to concentrate and shape magnetic fields such as iron-dominated magnets, kickers or ferrite cavities. For ferromagnetic material the effect depends on the availability of conduction electrons, thus ferromagnets are a subcategory of metals. Ferrites in contrast, who belong to the group of ferrimagnetic materials, are typically insulators. The degree of magnetization that a ferromagnet or ferrimagnet obtains in response to an external field, is described by the relative permeability μ_r in reference to vacuum which has the permeability μ_0 (relative permeability $\mu_\mathrm{r} = 1$):

$$\mu(\vec{r}) = \mu_0 \mu_\mathrm{r}(\vec{r}) \tag{2.13}$$

In the following, only ferrites will be quoted due to their later relevance for application. Nevertheless, the provided information is equally valid for ferromagnets. In the most simple approach, μ_r is assumed as constant, providing a linear relation between $\vec{H}$ and $\vec{B}$. This ignores the fact that in practice most materials exhibit nonlinearity and hysteresis. Depending on the magnitude of the magnetic field under operation, linearization may be acceptable.

When the external field has been reduced to zero, a residual flux remains (remanence or remanent magnetization B_r). An external field of reverse polarity is required, to diminish this flux to zero (coercitivity or coercitive field H_c). After passing through the initial magnetization curve, the B-H graph shows a closed loop. Reversing the polarization process requires energy which is measured by the area enclosed by the hysteresis loop. Similar to the case of dielectrics, it is convenient to include magnetic losses by means of a complex material parameter, namely the complex relative permeability $\underline{\mu}_\mathrm{r}$:

$$\begin{aligned} \mu(\vec{r}, \omega) &= \mu_0 \underline{\mu}_\mathrm{r}(\vec{r}, \omega) && (2.14\mathrm{a}) \\ &= \mu_0 \left(\mu_\mathrm{r}'(\vec{r}, \omega) - j \mu_\mathrm{r}''(\vec{r}, \omega) \right) && (2.14\mathrm{b}) \end{aligned}$$

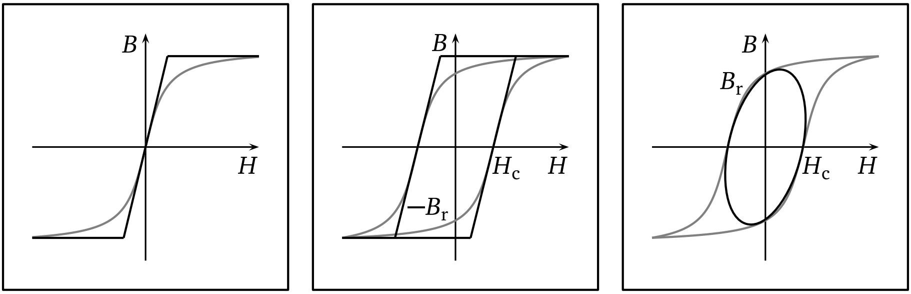

(a) no hysteresis **(b)** linear approximation **(c)** ellipse approximation

Figure 2.1.: The figures illustrate the dependency of the magnetic flux density B on the magnetic field intensity H. Figure (a) shows the case of a non-linear material without hysteresis which can be linearized for small amplitudes. Figures (b) and (c) show a piecewise linear and an ellipse approximation for a non-linear material with hysteresis.

According 2.4b, the magnetic induction for a given field intensity $\underline{\vec{H}} = \vec{H}_0 e^{j0}$ reads:

$$\begin{aligned}\vec{B}(t) &= \mathrm{Re}\left\{\underline{\vec{B}} e^{j\omega t}\right\} && (2.15a)\\ &= \mathrm{Re}\left\{\underline{\mu}\underline{\vec{H}} e^{j\omega t}\right\} \\ &= \mu_0 \vec{H}_0 \mathrm{Re}\left\{\mu_r' \cos\omega t + \mu_r'' \sin\omega t + j\left(\mu_r' \sin\omega t - \mu_r'' \cos\omega t\right)\right\} \\ &= \mu_0 \vec{H}_0 \left(\mu_r' \cos\omega t + \mu_r'' \sin\omega t\right) && (2.15b)\end{aligned}$$

If $B(t)$ is plotted versus $H(t)$, a sheared ellipse is formed - a LISSAJOUS figure of lowest order. This means that the losses created by the frequency ω are taken into account, but not higher harmonics as they usually occur due to non-linearity (distortion). The difference results in an underestimation of the losses. The sum of the two trigonomic functions can also be interpreted as a frequency dependent phase shift, which originates from the frequency-dependent ability of the dipoles to follow the external polarizing field. The spectral magnetic loss reads:

$$P_{\mu,\omega} = \omega \int\limits_V \frac{1}{2} \mu_0 \mu_r'' \left|\underline{\vec{H}}\right|^2 dV \tag{2.16}$$

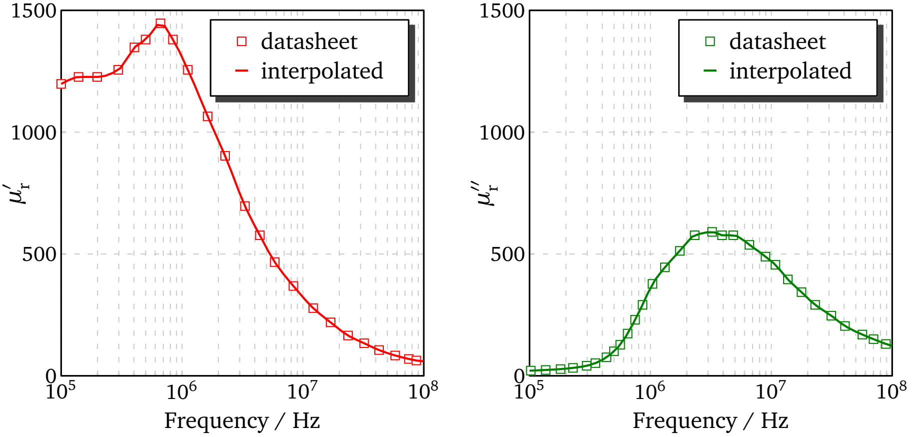

(a) **(b)**

Figure 2.2.: Typical characteristics for a NiZn based ferrite [45]: Figures (a) and (b) show the real and imaginary parts of the relative permeability versus frequency.

The average magnetic loss is determined through integration over a full period T. Therefore the maximum dissipation for a probe volume with homogenous field distribution occurs for the frequency where μ_{r}'' reaches its maximum value. Generally this is not true for a practical device, since the distribution of the magnetic field inside the ferrite is frequency dependent as well.

2.3 Poynting's theorem

In the previous sections, loss mechanisms of different kind have been introduced. The complex form of Poynting's theorem is derived from Maxwell's equations 2.1a and 2.1b in frequency domain. It resembles the central conservation law for EM energy.

$$\operatorname{curl}\underline{\vec{E}} = -j\omega\underline{\mu}\underline{\vec{H}} \xrightarrow{\cdot\,\underline{\vec{H}}^*} \underline{\vec{H}}^* \cdot \operatorname{curl}\underline{\vec{E}} = -j\omega\underline{\mu}\underline{\vec{H}}\cdot\underline{\vec{H}}^* \tag{2.17a}$$

$$\operatorname{curl}\underline{\vec{H}}^* = -j\omega\underline{\varepsilon}^*\underline{\vec{E}}^* \xrightarrow{\cdot\,\underline{\vec{E}}} \underline{\vec{E}} \cdot \operatorname{curl}\underline{\vec{H}}^* = -j\omega\underline{\varepsilon}^*\underline{\vec{E}}\cdot\underline{\vec{E}}^* \tag{2.17b}$$

Adding both equations, multiplying by factor 1/2 and applying a vector identity [1] yields:

$$\underbrace{\frac{1}{2}\underline{\vec{H}}^{*}\cdot\mathrm{curl}\,\underline{\vec{E}}-\frac{1}{2}\underline{\vec{E}}\cdot\mathrm{curl}\,\underline{\vec{H}}^{*}}=\frac{1}{2}j\omega\underline{\varepsilon}^{*}\underline{\vec{E}}\cdot\underline{\vec{E}}^{*}-\frac{1}{2}j\omega\underline{\mu}\underline{\vec{H}}\cdot\underline{\vec{H}}^{*}\tag{2.18a}$$

$$\mathrm{div}\left(\frac{1}{2}\underline{\vec{E}}\times\underline{\vec{H}}^{*}\right)=\frac{1}{2}j\omega\left(\underline{\varepsilon}^{*}\left|\underline{\vec{E}}\right|^{2}-\underline{\mu}\left|\underline{\vec{H}}\right|^{2}\right)\tag{2.18b}$$

The cross product on the left hand side is identified as the Poynting vector $\underline{\vec{S}}:=\frac{1}{2}\underline{\vec{E}}\times\underline{\vec{H}}^{*}$. With the use of the definitions for the complex material parameters, the individual components can be written separately:

$$\begin{aligned}\mathrm{div}\,\underline{\vec{S}}&=\frac{1}{2}j\omega\left[\varepsilon_0\varepsilon_{\mathrm{r}}'+j\left(\varepsilon_0\varepsilon_{\mathrm{r}}''+\frac{\kappa}{\omega}\right)\left|\underline{\vec{E}}\right|^{2}-\left(\mu_0\mu_{\mathrm{r}}'-j\mu_0\mu_{\mathrm{r}}''\right)\left|\underline{\vec{H}}\right|^{2}\right]\\&=\underbrace{\frac{1}{2}j\omega\varepsilon_0\varepsilon_{\mathrm{r}}'\left|\underline{\vec{E}}\right|^{2}-\frac{1}{2}j\omega\mu_0\mu_{\mathrm{r}}'\left|\underline{\vec{H}}\right|^{2}}_{\text{stored EM energy}}\underbrace{-\frac{1}{2}\kappa\left|\underline{\vec{E}}\right|^{2}-\frac{1}{2}\omega\varepsilon_0\varepsilon_{\mathrm{r}}''\left|\underline{\vec{E}}\right|^{2}-\frac{1}{2}\omega\mu_0\mu_{\mathrm{r}}''\left|\underline{\vec{H}}\right|^{2}}_{\text{dissipated EM energy}}\end{aligned}\tag{2.19}$$

For the stored energy the following densities are defined:

$$\bar{w}_E:=\frac{1}{2}\left(\frac{1}{2}\varepsilon_0\varepsilon_{\mathrm{r}}'\left|\underline{\vec{E}}\right|^{2}\right)=\frac{1}{4}\mathrm{Re}\left\{\varepsilon_0\underline{\varepsilon}_{\mathrm{r}}\right\}\left|\underline{\vec{E}}\right|^{2}\qquad\text{electric energy density}\tag{2.20a}$$

$$\bar{w}_H:=\frac{1}{2}\left(\frac{1}{2}\mu_0\mu_{\mathrm{r}}'\left|\underline{\vec{H}}\right|^{2}\right)=\frac{1}{4}\mathrm{Re}\left\{\mu_0\underline{\mu}_{\mathrm{r}}\right\}\left|\underline{\vec{H}}\right|^{2}\qquad\text{magnetic energy density}\tag{2.20b}$$

Loss densities are defined for the dissipative terms:

$$p_\kappa:=\frac{1}{2}\kappa\left|\underline{\vec{E}}\right|^{2}\qquad\text{resistive loss density}\tag{2.20c}$$

$$p_\varepsilon:=\frac{1}{2}\omega\varepsilon_0\varepsilon_{\mathrm{r}}''\left|\underline{\vec{E}}\right|^{2}=-\frac{1}{2}\omega\mathrm{Im}\left\{\varepsilon_0\underline{\varepsilon}_{\mathrm{r}}\right\}\left|\underline{\vec{E}}\right|^{2}\qquad\text{dielectric loss density}\tag{2.20d}$$

$$p_\mu:=\frac{1}{2}\omega\mu_0\mu_{\mathrm{r}}''\left|\underline{\vec{H}}\right|^{2}=-\frac{1}{2}\omega\mathrm{Im}\left\{\mu_0\underline{\mu}_{\mathrm{r}}\right\}\left|\underline{\vec{H}}\right|^{2}\qquad\text{magnetic loss density}\tag{2.20e}$$

---

[1] $\mathrm{div}\left(\vec{A}\times\vec{B}\right)=\vec{B}\cdot\mathrm{curl}\vec{A}-\vec{A}\cdot\mathrm{curl}\vec{B}$

Consequently, the (spectral) losses occurring from the three different mechanisms are obtained by integration:

$$P_{\kappa} = \frac{1}{2} \int\limits_{V} \kappa \left|\underline{\vec{E}}\right|^{2} dV = \int\limits_{V} p_{\kappa} dV \tag{2.21a}$$

$$P_{\varepsilon,\omega} = \frac{1}{2} \int\limits_{V} \omega \varepsilon_{0} \varepsilon_{\mathrm{r}}'' \left|\underline{\vec{E}}\right|^{2} dV = \int\limits_{V} p_{\varepsilon} dV \tag{2.21b}$$

$$P_{\mu,\omega} = \frac{1}{2} \int\limits_{V} \omega \mu_{0} \mu_{\mathrm{r}}'' \left|\underline{\vec{H}}\right|^{2} dV = \int\limits_{V} p_{\mu} dV \tag{2.21c}$$

The integral formulation of Poynting's theorem presents the power balance for a finite volume V.

$$\int\limits_{\partial V} \underline{\vec{S}} \cdot d\vec{A} = -\int\limits_{V} \left(p_{\kappa} + p_{\varepsilon} + p_{\mu}\right) dV - 2j\omega \int\limits_{V} \left(\bar{w}_{H} - \bar{w}_{E}\right) dV \tag{2.22}$$

The particle beam, which is identified as the source of the EM fields in one of the following sections should therefore loose energy. However, for the definition of coupling impedances a rigid beam is assumed. The momentum of the particles remains unchanged while traversing the volume V. Strictly-speaking, this presents a violation of the conservation law.

2.4 Commonly used coordinate systems

Throughout this work two coordinate systems will be used, namely cartesian coordinates $\{x, y, z\}$ and circular cylindrical coordinates $\{\varrho, \varphi, z\}$. The corresponding sets of unit vectors are $\left\{\vec{e}_{x}, \vec{e}_{y}, \vec{e}_{z}\right\}$ and $\left\{\vec{e}_{\varrho}, \vec{e}_{\varphi}, \vec{e}_{z}\right\}$ respectively. It must be distinguished between two inertial systems of reference. Firstly, a coordinate system K which is at rest (laboratory frame), and secondly a coordinate system K' following the motion of the ideal particle (center of mass frame). Most calculations are carried out in the laboratory frame. Coordinates and physical quantities in the center of mass frame are marked with a prime such as $\{x', y', z'\}$ and $\left\{\vec{E}', \vec{H}'\right\}$, respectively.

Generally, the orbit exhibits curvature, particularly in the case of synchrotron accelerators. If the radius of the section of interest is large compared to its length, this section may be treated as a straight line. The ideal particle virtually performs a uniform motion along the z- axis of the coordinate system.

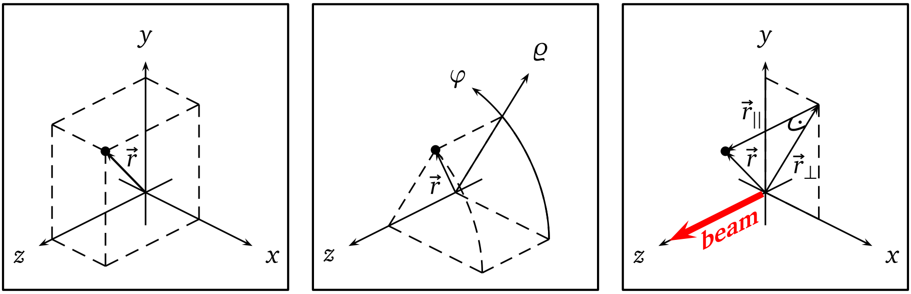

(a) Cartesian **(b)** Cylindrical **(c)** Transverse/Longitudinal

Figure 2.3.: (a) and (b) display the commonly used coordinate conventions; (c) displays the coordinate system in the context of the particle beam.

It is convenient to distinguish between the *longitudinal direction* which is parallel to the direction of particle motion and the *transverse directions* which are perpendicular to the direction of particle motion. Therefore z denotes the *longitudinal coordinate* while x and y (ϱ and φ in cylindrical coordinates) denote the *transverse coordinates*.[2] Additionally, a transverse position vector $\vec{r}_\perp$, a longitudinal position vector $\vec{r}_{||}$ and the corresponding unit vectors $\{\vec{e}_\perp, \vec{e}_{||}\}$ are defined:

$$\vec{r} = \vec{r}_\perp + \vec{r}_{||} \tag{2.23}$$

$$= r_\perp \vec{e}_\perp + r_{||}\vec{e}_{||} \tag{2.24}$$

$$= \underbrace{\overbrace{x\vec{e}_x + y\vec{e}_y}} + \overbrace{z\vec{e}_z} \tag{2.25}$$

$$= \varrho\vec{e}_\varrho + z\vec{e}_z \tag{2.26}$$

The orbit determines the transverse reference position for all particles which coincides with the center of the cross-section in most beamline elements. However, in practice the orbit may already have an unknown transverse displacement from the geometrical center of the aperture (closed orbit deviation).

---

[2] This is the most convenient convention, a different convention is used in [Wil96].

2.5 Sources

The *beam* in a particle accelerator typically consists of a *bunch* sequence with a predefined spacing and an average number of charged particles per bunch (bunched beam). Such a particle beam represents unbound charge and current at the same time. Consequently, it contributes both to the charge density q_V and to the current density $\vec{J}_\beta$. The charge Q_{beam} transported by the beam and the beam current I_{beam} read:

$$Q_{\text{beam}} = \int_{V_{\text{beam}}} q_V \, dV \tag{2.27a}$$

$$I_{\text{beam}} = \int_{A_{\text{beam}}} \vec{J}_\beta \cdot d\vec{A} \tag{2.27b}$$

The particles perform a uniform motion in the longitudinal direction, transverse motion is neglected as is much slower in comparison. In the context of the previously given coordinate convention, the velocity and the current density exhibit a z-component only. The *bunch profile* is characterized by the longitudinal and transverse charge distribution with respect to the barycenter of the bunch. This can be expressed as the product of a surface charge density $q_\perp$ in the transverse plane and a line density $q_{||}$ along the longitudinal axis:

$$q_V(\vec{r}, t) = q_\perp(\vec{r}_\perp) q_{||}(\vec{r}_{||}, t) \tag{2.28a}$$

$$\vec{J}_\beta(\vec{r}, t) = v q_\perp(\vec{r}_\perp) q_{||}(\vec{r}_{||}, t) \vec{e}_z \tag{2.28b}$$

Obviously, the source terms in MAXWELL's equations do not vanish in the presence of a charged particle beam causing a system of inhomogenous partial differential equations. Without loss of generality, the line density is replaced with a DIRAC delta function. The effect of an arbitrary line density can be studied by using the GREEN function property of the solution (Appendix E).

$$q_V(\vec{r}, t) = q_\perp(\vec{r}_\perp) \delta(z - vt) \tag{2.29a}$$

$$\vec{J}_\beta(\vec{r}, t) = v q_\perp(\vec{r}_\perp) \delta(z - vt) \vec{e}_z \tag{2.29b}$$

In the context of proton and heavy ion beams, the transverse profile is conveniently approximated as a circular disc of radius a with homogenous charge distribution. This can be expressed with the HEAVISIDE step function:

$$q_\perp = \frac{Q}{\pi a^2}\Theta(a - r_\perp) = \begin{cases} \frac{Q}{\pi a^2} & \text{, for } 0 \leq r_\perp \leq a \\ 0 & \text{, for } a < r_\perp \end{cases} \tag{2.30}$$

The current density and the charge density read:

$$q_V(\vec{r}_\perp, z, t) = \frac{Q}{\pi a^2}\Theta(a - r_\perp)\delta(z - vt) \tag{2.31a}$$

$$\vec{J}_\beta(\vec{r}_\perp, z, t) = v\frac{Q}{\pi a^2}\Theta(a - r_\perp)\delta(z - vt)\vec{e}_z \tag{2.31b}$$

The distribution of the sources given in equation 2.31b is symmetrical with respect to the z- axis. In general, the particle beam may have a transverse displacement, which requires an appropriate modification to account for the asymmetry. A detailed deduction of the source terms is presented in Appendix 2.5. To first order the displacement may be approximated by a superposition of the original distribution and an additional line density proportional to the cosine of the azimuthal angle φ:

$$q_V(\vec{r}_\perp, z, t) \approx \frac{Q}{\pi a^2}\left(\Theta(a - r_\perp) + d_x \cos\varphi\, \delta(a - r_\perp)\right)\delta(z - vt) \tag{2.32a}$$

$$\vec{J}_\beta(\vec{r}_\perp, z, t) \approx v\frac{Q}{\pi a^2}\left(\Theta(a - r_\perp) + d_x \cos\varphi\, \delta(a - r_\perp)\right)\delta(z - vt)\vec{e}_z \tag{2.32b}$$

The transverse displacement in x- and y- direction is given by d_x and d_y, respectively. Thus a similar expression exists for a beam which is displaced in the y-direction. Furthermore, the following moments are defined:

$$\mathcal{Q}^0 := Qd^0 \qquad (0^{th} \text{ order, monopolar}) \tag{2.33a}$$

$$\mathcal{Q}^1 := Qd^1 \qquad (1^{st} \text{ order, dipolar}) \tag{2.33b}$$

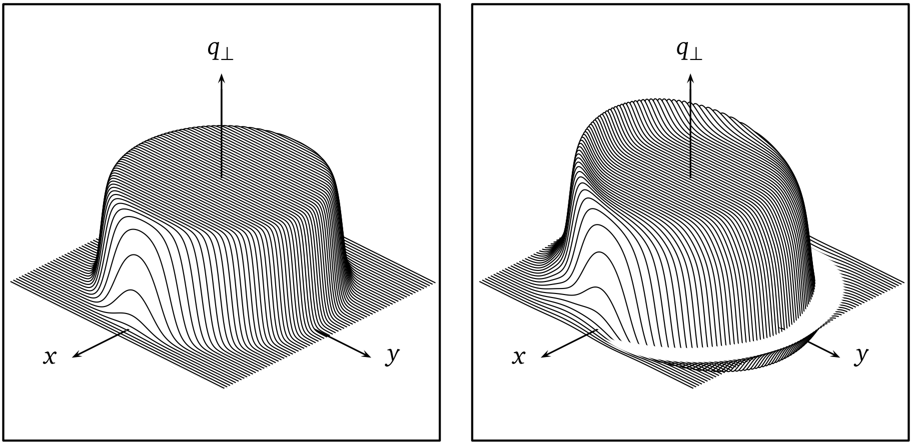

(a) centered beam **(b)** displaced beam

Figure 2.4.: The figures illustrate the charge distribution in the transverse plane. Figure (a) pictures the constant density for a centered beam, while figure (b) pictures a tilted distribution for a beam displacement in the direction of the y- coordinate.

To obtain a frequency domain representation, the FOURIER transform is applied to the line density:

$$\mathfrak{F}\{\delta(z - vt)\} = \int_{-\infty}^{+\infty} \delta(z - vt) e^{-j\omega t} \,\mathrm{d}t \tag{2.34a}$$

Substituting $z' = z - vt,\ \mathrm{d}z' = -v\,\mathrm{d}t$ and $t = -(z' - z)/v$, yields:

$$\begin{aligned} &= -\frac{1}{v} e^{-j\frac{\omega}{v}z} \underbrace{\int_{+\infty}^{-\infty} \delta(z') e^{j\frac{\omega}{v}z'} \,\mathrm{d}z'} \\ &= -\frac{1}{v} e^{-j\frac{\omega}{v}z} \qquad \cdot(-1) \\ &= \frac{1}{v} e^{-j\frac{\omega}{v}z} \end{aligned} \tag{2.34b}$$

Thus, the frequency domain formulation for the sources reads:

$$\underline{q}_V(\vec{r}_\perp, z, \omega) \approx \frac{Q}{\pi a^2}\left(\Theta(a - r_\perp) + d_x \cos\varphi\,\delta(a - r_\perp)\right)\frac{1}{v}e^{-j\frac{\omega}{v}z} \tag{2.35a}$$

$$\underline{\vec{J}}_\beta(\vec{r}_\perp, z, \omega) \approx \frac{Q}{\pi a^2}\left(\Theta(a - r_\perp) + d_x \cos\varphi\,\delta(a - r_\perp)\right)e^{-j\frac{\omega}{v}z}\vec{e}_z \tag{2.35b}$$

All source terms that are used in the scope of this work are based on the above formulation or related expressions.

2.6 Point charge in uniform motion

Equation 2.29 provides the source terms for the case of a point charge travelling along the z-axis at constant velocity v. The EM field is obtained by solving the inhomogenous wave equation. The solutions are known as LIÉNARD-WIECHERT potentials, a special case of the retarded potentials [Jac99].

The same solution can be obtained by applying the LORENTZ transform to the well-known solution for the static limit ($v \to 0$). For single point charge Q_0 at rest located at the origin of the inertial system K', solution for the electric potential Φ' reads:

$$\Phi'(\vec{r}\,') = \frac{Q_0}{4\pi\varepsilon_0}\frac{1}{\sqrt{x'^2 + y'^2 + z'^2}} \tag{2.36a}$$

$$= \frac{Q_0}{4\pi\varepsilon_0}\frac{1}{\sqrt{\varrho'^2 + z'^2}} \tag{2.36b}$$

From this potential the electric field is obtained:

$$\vec{E}'(\vec{r}\,') = -\operatorname{grad}\Phi'(\vec{r}\,') \tag{2.37a}$$

$$= \frac{Q_0}{4\pi\varepsilon_0}\frac{x'\vec{e}_x + y'\vec{e}_y + z'\vec{e}_z}{\sqrt{x'^2 + y'^2 + z'^2}^3} \tag{2.37b}$$

$$= \frac{Q_0}{4\pi\varepsilon_0}\frac{\varrho'\vec{e}_\varrho + z'\vec{e}_z}{\sqrt{\varrho'^2 + z'^2}^3} \tag{2.37c}$$

All coordinate axes of the system K' are aligned in parallel to the corresponding axes of the system K. K' performs a uniform motion with velocity v in the positive z direction of system K. The relative motion of the two inertial systems deforms the electric field and produces and additional magnetic field for an observer that is located in K. The EM field which is observed in system K is obtained by applying the LORENTZ transform [Jac99]:

$$\vec{E}(\vec{r}) = \frac{Q_0\gamma}{4\pi\varepsilon_0} \frac{x\vec{e}_x + y\vec{e}_y + (z - vt)\vec{e}_z}{\sqrt{x^2 + y^2 + \gamma^2 (z - vt)^2}^3} \tag{2.38a}$$

$$= \frac{Q_0\gamma}{4\pi\varepsilon_0} \frac{\varrho\vec{e}_\varrho + (z - vt)\vec{e}_z}{\sqrt{\varrho^2 + \gamma^2 (z - vt)^2}^3} \tag{2.38b}$$

The magnetic field reads:

$$\vec{B}(\vec{r}) = \frac{Q_0\beta\gamma}{4\pi\varepsilon_0 c_0} \frac{-y\vec{e}_x + x\vec{e}_y}{\sqrt{x^2 + y^2 + \gamma^2 (z - vt)^2}^3} \tag{2.38c}$$

$$= \frac{Q_0\beta\gamma}{4\pi\varepsilon_0 c_0} \frac{\varrho\vec{e}_\varphi}{\sqrt{\varrho^2 + \gamma^2 (z - vt)^2}^3} \tag{2.38d}$$

$$= \frac{\beta}{c_0} E_\varrho \vec{e}_\varphi \tag{2.38e}$$

The EM field of a point charge in uniform motion consists of a radial electric field and an azimuthal magnetic field. The electric field reduces to the well-known COULOMB solution in the static limit $v \to 0$. In the ultra-relativistic limit $v \to c_0$ the EM field approaches the field of a Transverse Electromagnetic (TEM) wave. These results allow to draw several conclusions for the ultrarelativistic case :

- The longitudinal field vanishes in the entire transverse plane. This is also true for the case of a perfectly conducting environment.
- There is no feedback action on the beam through the self-field.
- Feedback action may only occur through the induced secondary fields in the environment caused by variations of the geometry or specific material properties including finite conductivity.

Further conclusions for the non-ultrarelativistic case:

- The feedback action through the longitudinal self-field increases with decreasing velocity.
- Feedback action occurs through the induced secondary fields.

2.7 Inhomogenous wave equation

The source fields that have been introduced in the previous sections can be interpreted as plane waves. Consequently, the general approach must allow for wave solutions. A detailed deduction of the wave equations in TD and FD is listed in Appendix B. For analytical studies the FD formulation has many advantages such as complex-valued material parameters to account for lossy materials. The current density $\underline{\vec{J}}$ consists of the convection current density $\underline{\vec{J}}_\beta = v\underline{q}_V\vec{e}_z$, which is given by the beam current. The source fields are non-vanishing in vacuum region only, thus μ and ε can be replaced with μ_0 and ε_0 on the Right Hand Side (RHS). Under consideration of the source terms, the wave equations for the field intensities read:

$$\nabla^2\underline{\vec{E}} + \omega^2\underline{\varepsilon}\underline{\mu}\underline{\vec{E}} = j\omega\mu_0 v\underline{q}_V\vec{e}_z + \operatorname{grad}\left(\frac{\underline{q}_V}{\varepsilon_0}\right) \tag{2.39a}$$

$$\nabla^2\left(\underline{\mu}\underline{\vec{H}}\right) + \omega^2\underline{\varepsilon}\underline{\mu}\left(\underline{\mu}\underline{\vec{H}}\right) = -\mu_0\operatorname{curl}\left(v\underline{q}_V\vec{e}_z\right) \tag{2.39b}$$

In the following the z- axis shall be the center of a waveguide. In order to obtain only field components that are synchronous with the particles, the field solution must share the same longitudinal dependency as the source of excitation:

$$\left\{\begin{array}{c}\underline{\vec{E}}\\ \underline{\vec{H}}\end{array}\right\} \propto e^{-jk_z z} \Rightarrow \frac{\partial}{\partial z} \rightarrow -jk_z \tag{2.40}$$

The wave number $k_z = \omega/v$ has been introduced. The wave equation can be reduced to a Two dimensional (2D) problem in the transverse plane by separating the dependency on the longitudinal coordinate.

$$\underline{\vec{E}}(\vec{r},\omega) = \underline{\vec{E}}_{2D}(\vec{r}_\perp,\omega)e^{-jk_z z} \tag{2.41a}$$

$$\underline{\vec{H}}(\vec{r},\omega) = \underline{\vec{H}}_{2D}(\vec{r}_\perp,\omega)e^{-jk_z z} \tag{2.41b}$$

With the transverse Laplace operator $\Delta_\perp = \Delta - \frac{\partial^2}{\partial z^2}$ the wave equations read:

$$\left(\Delta_\perp + \omega^2\left(\underline{\varepsilon}\underline{\mu} - \frac{1}{v^2}\right)\right)\underline{\vec{E}} = j\omega\mu_0 v \underline{q}_V \vec{e}_z + \operatorname{grad}\left(\frac{\underline{q}_V}{\varepsilon_0}\right) \tag{2.42a}$$

$$\left(\Delta_\perp + \omega^2\left(\underline{\varepsilon}\underline{\mu} - \frac{1}{v^2}\right)\right)\underline{\vec{H}} = -\operatorname{curl}\left(v \underline{q}_V \vec{e}_z\right) \tag{2.42b}$$

In chapter 4 the focus is put on solving these equations for selected examples with either rotational or planar symmetry.

3 Wake Function and Coupling Impedance

Following up the previous chapter, this chapter will introduce to the concept of describing the interaction between a charged particle beam with its immediate environment by means of coupling impedances and wakefields. The starting point is set by the LORENTZ *force equation*[1]*, which describes the force acting on a point charge due to an electromagnetic field [Jac99]:*

$$\begin{aligned}\vec{F}_{\mathrm{L}} &= \vec{F}_E + \vec{F}_B \\ &= q\left(\vec{E} + \vec{v} \times \vec{B}\right) \qquad (3.1a)\end{aligned}$$

Since the sole interest lies in the net effect of the electromagnetic fields on the particle beam, it is convenient to deal with a more compact formulation instead of a full field solution. Coupling impedances provide a standardized measure by relating the longitudinal and transverse forces experienced by a trailing probe charge with the excitation given by a leading source charge. Coupling impedances are an integral quantity, which implies that the effect is calculated for a certain interval in which the perturbation of the average particle motion is negligible [ZK98]. The consequence of this abstraction with respect to synchrotron accelerators will be illustrated and the central definitions will be summarized. Finally the problem of determining the coupling impedances will be adressed, providing an introduction to the different approaches and the different types of impedance contributions.

---

[1] In some publications the electric force $\vec{F}_E$ is named COULOMB force, whereas the magnetic force $\vec{F}_B$ is named LORENTZ force for historical reasons.

3.1 Prerequisites

A non-vanishing LORENTZ force causes an instantaneous change of particle momentum, which in turn leads to an altered trajectory and therefore a different electromagnetic source field. Hence, in the most general case a bi-directional coupling between the equations that describe the particle motion and the equations that describe the EM field must be considered.

In the context of wakefields and impedances it is assumed that the perturbation of the average particle motion remains small in a predefined interval, such that the source fields remain practically unaltered. This abstraction is known as *rigid beam approximation* [Ng06, ZK98]. Furthermore, the effect of the LORENTZ force is captured as the total change of momentum $\Delta\vec{p}$ which is known as the *impulse approximation* [Ng06]. In the field of proton and heavy-ion synchrotron accelerators the interval is chosen as the path of a single revolution with period T_0. In this context the change of momentum is sometimes referred to as *kick per turn*.

$$\Delta\vec{p} = \int\limits_{\Delta t} \vec{F}_\mathrm{L}\,\mathrm{d}t \xrightarrow{\Delta t \to T_0} \Delta\vec{p} = \int\limits_{T_0} \vec{F}_\mathrm{L}\,\mathrm{d}t \tag{3.2}$$

3.2 Wake function

In the following a source charge q_1 is assumed followed by a probe charge q_2 at some distance s. Both charges are point-like and move with constant velocity v in the direction of the positive z- axis while the leading charge produces an EM force field which impacts the trailing probe charge.

The LORENTZ force acting on the probe charge can be split into a longitudinal component and a transverse component. Each component is integrated along the path of motion and normalized with respect to the charge which gives rise to the definition of the *wake function*. The longitudinal wake function $G_{||}$ is defined as follows [ZK98][2]:

$$G_{||}(\vec{r}_{\perp 1}, \vec{r}_{\perp 2}, s) = \frac{1}{q} \int\limits_{-\infty}^{\infty} E_z(\vec{r}_{\perp 1}, \vec{r}_{\perp 2}, z, t = \tfrac{z+s}{v})\,\mathrm{d}z \tag{3.3}$$

---

[2] The algebraic sign convention may vary.

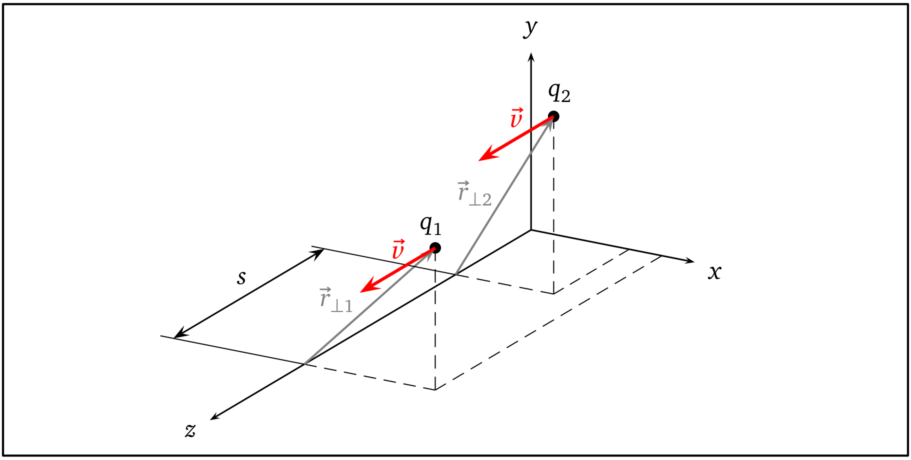

Figure 3.1.: Leading source charge q_1 and trailing probe charge q_2 moving at constant velocity v and distance s in a cartesian coordinate system.

The EM field at the location of the probe charge depends both on the location of the leading source charge $\vec{r}_1$ and the location of the trailing probe charge $\vec{r}_2$. The longitudinal wake function itself depends on the transverse coordinates $\vec{r}_{\perp 1}$ and $\vec{r}_{\perp 2}$ and the distance s. The wake function has the unit V/C and can be interpreted as the decelerating voltage per unit charge or the energy loss per unit charge squared. By analogy with equation 3.3 the transverse wake function $G_\perp$ is defined as follows [ZK98][3]:

$$\begin{aligned} G_\perp(\vec{r}_{\perp 1}, \vec{r}_{\perp 2}, s) &= \frac{1}{q} \int\limits_{-\infty}^{\infty} \left[\vec{E}_\perp(\vec{r}_{\perp 1}, \vec{r}_{\perp 2}, z, t = \tfrac{z+s}{v}) + \vec{v} \times \vec{B}_\perp(\vec{r}_{\perp 1}, \vec{r}_{\perp 2}, z, t = \tfrac{z+s}{v}) \right] \mathrm{d}z \\ &= \left\{ \begin{array}{c} G_x(\vec{r}_{\perp 1}, \vec{r}_{\perp 2}, z, t = \tfrac{z+s}{v}) \\ G_y(\vec{r}_{\perp 1}, \vec{r}_{\perp 2}, z, t = \tfrac{z+s}{v}) \end{array} \right\} \end{aligned} \tag{3.4}$$

Close to an axis of symmetry the wakefield is dominated by the monopolar field which exists regardless of a transverse displacement of the beam. Therefore the longitudinal wake function is commonly calculated while assuming a centered par-

---

[3] Vector or tensor notation is sometimes used for the transverse wake function.

ticle beam ($\vec{r}_{\perp 1} = \vec{r}_{\perp 2} = 0$). The remaining dependency is the distance s between source charge and probe charge:

$$G_{||}(s) = \frac{1}{q} \int_{-\infty}^{\infty} E_z(z, t = \tfrac{z+s}{v})\,\mathrm{d}z \tag{3.5}$$

The transverse wakefield is dominated by the dipolar field which to first approximation depends linearly on the transverse displacement of the particle beam. Close to an axis of symmetry a dipolar field exists only for a displaced beam. Therefore the longitudinal wake function is calculated while assuming a displaced beam ($\vec{r}_{\perp 1} = \vec{r}_{\perp 2} = \vec{d}$). In addition the integral is normalized with respect to the displacement d which is done separately for the horizontal and vertical direction.

$$\begin{aligned} G_x(d_x, s) &= \frac{1}{q d_x} \int_{-\infty}^{\infty} E_x(d_x, z, t = \tfrac{z+s}{v}) - v B_y(d_x, z, t = \tfrac{z+s}{v})\,\mathrm{d}z \\ G_y(d_y, s) &= \frac{1}{q d_y} \int_{-\infty}^{\infty} E_y(d_y, z, t = \tfrac{z+s}{v}) + v B_x(d_y, z, t = \tfrac{z+s}{v})\,\mathrm{d}z \end{aligned} \tag{3.6}$$

In practice charge distributions always have finite dimensions and the wake function is mostly relevant for theoretical considerations. The *wake potential* W[4] is given by the convolution of the wake function G with the line charge density q_L [ZK98] and therefore represents a measure for the feedback acting on a whole distribution:

$$W_{||}(s) = \int_{-\infty}^{s} G_{||}(s - \tilde{s}) q_L(\tilde{s})\mathrm{d}\tilde{s} \tag{3.7}$$

$$W_{\perp}(s) = \int_{-\infty}^{s} G_{\perp}(s - \tilde{s}) q_L(\tilde{s})\mathrm{d}\tilde{s} \tag{3.8}$$

If only the wake potential is known, this relation is used to obtain the wake function by inverse convolution [ZK98].

---

[4] Various publications use the symbol W for the wake function. The wake function represents a special case where the charge distribution is given by the DIRAC delta function.

3.3 Coupling impedances

Due to the periodicity of the particle motion it is advantageous to fall back on frequency domain for the underlying electrodynamics as well. This accomplished by introducing the concept of *coupling impedances*. In the field of circuit theory an impedance relates the voltage across a *passive*, *linear* and *time-invariant* one-port network with the current flowing in and out of the terminals. Through interpretation of the electric field along a predefined path as a voltage U and the particle beam as a current I an *impedance* can be defined:

$$\underline{Z} = \frac{\underline{U}}{\underline{I}} = \frac{\int\limits_L \underline{E}\,\mathrm{d}l}{\int\limits_A \underline{J}\,\mathrm{d}A} \tag{3.9}$$

This interpretation is not limited to the longitudinal electric field and may be generalized to the remaining components of the wakefield [Ng06, ZK98]. This concept was initially proposed in [51]. By analogy with equation 3.5, the longitudinal coupling impedance is defined as [ZK98]:

$$\underline{Z}_{||}(\omega) = -\frac{1}{q}\int\limits_{-\infty}^{\infty} \underline{E}_z(\vec{r}_\perp = 0, z)e^{j\frac{\omega}{v}z}\,\mathrm{d}z \tag{3.10}$$

Similarly and by analogy with equation 3.6, the transverse coupling impedances are defined as [ZK98]:

$$\begin{aligned}\underline{Z}_x(d_x,\omega) &= -\frac{j}{qd_x}\int\limits_{-\infty}^{\infty}\Big(\underline{E}_x(d_x,\omega) - v\underline{B}_y(d_x,\omega)\Big)e^{j\frac{\omega}{v}z}\,\mathrm{d}z\\ \underline{Z}_y(d_y,\omega) &= -\frac{j}{qd_y}\int\limits_{-\infty}^{\infty}\Big(\underline{E}_y(d_y,\omega) + v\underline{B}_x(d_y,\omega)\Big)e^{j\frac{\omega}{v}z}\,\mathrm{d}z\end{aligned} \tag{3.11}$$

It can be shown that the coupling impedance is the FOURIER transform of the previously defined wake function. The proof is provided in appendix D.1. Thus, the following relations exist:

$$\underline{Z}(\vec{r}_\perp,\omega) = \mathfrak{F}\{G(\vec{r}_\perp, vt)\} \tag{3.12a}$$

$$G(\vec{r}_\perp, s) = \mathfrak{F}^{-1}\left\{\underline{Z}(\vec{r}_\perp,\omega)\right\} \tag{3.12b}$$

The definitions given so far assume a point-like charge distribution in the center of the transverse plane ($\vec{r}_\perp = 0$) or a transverse displacement ($\vec{r}_\perp \neq 0$). For the study of space-charge-dependent effects these definitions can be generalized to arbitrary charge distributions.

Accordingly, the integration must be performed over the entire volume V_{beam} that is occupied by the beam. The generalized definition for the longitudinal coupling impedance reads [20]:

$$\underline{Z}_{||}(\omega) = -\frac{1}{q^2} \int\limits_{V_{\text{beam}}} \underline{\vec{E}}(\vec{r}_\perp, z) \cdot \underline{\vec{J}}^*(\vec{r}_\perp, z)\, \mathrm{d}V \tag{3.13}$$

And the generalized definitions for the transverse coupling impedances read [20]:

$$\begin{aligned} \underline{Z}_x(d_x,\omega) &= -\frac{j}{qd_x} \int\limits_{-\infty}^{\infty} \left(\underline{E}_x(d_x,\omega) - v\underline{B}_y(d_x,\omega)\right) e^{j\frac{\omega}{v}z}\, \mathrm{d}z \\ \underline{Z}_y(d_y,\omega) &= -\frac{j}{qd_y} \int\limits_{-\infty}^{\infty} \left(\underline{E}_y(d_y,\omega) + v\underline{B}_x(d_y,\omega)\right) e^{j\frac{\omega}{v}z}\, \mathrm{d}z \end{aligned} \tag{3.14}$$

3.4 Consequences arising from the PANOFSKY-WENZEL theorem

Under the premise that $v = c_0$ and that the electromagnetic fields vanish in infinity, it can be shown that the impulse is irrotational which is known as the generalized PANOFSKY-WENZEL theorem [Ng06] [52]:

$$\operatorname{curl}(\Delta\vec{p}) = 0 \tag{3.15}$$

By considering either the longitudinal or the transverse component of equation 3.15, two more relations are obtained of which the second is usually referred to as the PANOFSKY-WENZEL theorem [34]:

$$\frac{\partial}{\partial x}\Delta p_y = \frac{\partial}{\partial y}\Delta p_x \tag{3.16a}$$

$$\frac{\partial}{\partial z}\Delta \vec{p}_\perp = \nabla_\perp p_z \tag{3.16b}$$

The latter reads in terms of the wake function:

$$\frac{\partial}{\partial z}G_\perp(\vec{r}_\perp, s) = \nabla_\perp G_{||}(\vec{r}_\perp, s) \tag{3.17}$$

This can be formulated in terms of coupling impedances as well [Ng06]. The horizontal and vertical coupling impedance related to the dipolar source fields read:

$$\underline{Z}_x(d_x, \omega) = \frac{v}{\omega}\underline{Z}_{||}(\vec{r}_\perp = d_x\vec{e}_x) \tag{3.18a}$$

$$\underline{Z}_y(d_y, \omega) = \frac{v}{\omega}\underline{Z}_{||}(\vec{r}_\perp = d_y\vec{e}_y) \tag{3.18b}$$

The PANOFSKY-WENZEL theorem directly results from MAXWELL's equations and puts constraints on the relations between transverse and longitudinal field components. This relation is commonly used to derive the transverse wake functions and coupling impedances from their longitudinal counterparts.

3.5 Coupling impedances in synchrotron accelerators

Different effects may contribute to coupling impedances. In a freespace environment, the electromagnetic field produced by the beam remains unperturbed. The transverse electric and magnetic forces compensate each other in the ultrarelativistic limit ($\beta \rightarrow 1$). In the case of an axis-symmetric charge distribution including the case of a point charge, the transverse components of the electric and magnetic force on a test particle vanish for symmetry reasons. The transverse components of the electric and magnetic force do not vanish for an off-axis test charge. The *self-field* acts as a radially defocusing lens [40]. This is the most basic collective effect originating from *direct space charge*.

Typically the particle beam is contained inside a metallic vacuum chamber. Electrostatic induction produces charges on the surface of the vacuum chamber which lead to a current in the opposite direction of the beam current. This wall current is often called *image current*[5] and affects the defocusing forces as *indirect space charge*, depending on geometry and material properties of the vacuum chamber. These effects are summarized under the term *space charge impedance* and contribute to the imaginary part of the coupling impedance.

Apart from geometrical changes of the beam environment such as variations of the cross-section, different dissipative effects contribute to the real part of the coupling impedance. Energy losses may be attributed to resistive material (finite conductivity κ) as well as hysteresis in ferrite or dielectric material. While the resistive losses are commonly summarized under the term *resistive wall impedance* there is no agreed term for magnetic and dielectric losses.

Finally the vacuum chamber represents a waveguide with adjacent cavity structures allowing for wave propagation and standing wave patterns (resonant modes). If the spectrum of the excitation remains below the cut-off frequency f_c of the lowest order waveguide mode, all electromagnetic fields appear in the form of evanescent waves. As a rule of thumb, f_c can be estimated from the maximum aperture and the freespace wavelength or the cut-off frequency of a cylindrical waveguide of similar dimensions. In the scope of this work it is assumed, that the frequency range of interest lies below cut-off of the lowest-order mode.

---

[5] Some authors have claimed that this term is misleading. Image charges and image currents are part of a strategy to solve boundary value problems in the field of classical electrodynamics with the superposition principle ([Jac99], method of images). While the image current is physical reality in the context of wall current, it is introduced as an auxiliary means in the method of images.

Thus, only evanescent waves moving in phase with the source field are taken into account (synchronous fields).

In particular cases such as magnet coils or pickup electrodes, certain components of the wake field may couple inductively or capacitively to lumped element networks that are located outside the vacuum chamber. The network is connected through a reference port for which an equivalent impedance can be determined by conventional methods of circuit analysis or bench measurements using a network analyzer. The network impedance transforms into an effective impedance which contributes to the coupling impedance.

The total coupling impedance is a combination of all the above, while particular contributions may outweigh others. If a budget has been set for the coupling impedance contributions, a priori knowledge about the predominant mechanisms is necessary. Different techniques have established to determine the coupling impedance contributions caused by different beamline elements. The fundamental properties of these techniques will be introduced in the next section.

3.6 Characterization of techniques for coupling impedance analysis

The different techniques to determine coupling impedances can be put into one of three categories. In the case of analytical and numerical methods an electromagnetic problem must be solved either analytically or numerically. On the contrary, experimental methods derive the coupling impedances from measurement data that has been obtained with an experimental setup. Under the premise that the technique of choice represents the actual physics correctly, all of the mentioned techniques have different properties in terms of requirements, applicability and achievable accuracy. In the following, a short introduction is provided for each category.

3.6.1 Analytical methods

Prior to the calculation of the coupling impedances, the electromagnetic field has to be determined, which requires solving MAXWELL's equations for the given source fields and boundary conditions. The application of analytical methods is typically limited to geometries which exhibit rotational or planar symmetry in combination with translational symmetry.

By choosing an adequate coordinate system, a Partial Differential Equation (PDE) (the wave equation for instance) can be split into multiple Ordinary Differential Equation (ODE)s. These remain connected through a separation equation but can be solved independently. Furthermore, in most analytical approaches the solution space is narrowed by a priori assuming time-harmonic solutions and a predefined direction of propagation in the case of wave solutions. In many cases where no closed-form solution can be obtained, the formulae must be evaluated numerically. Despite the fact that these approaches are rather semi-analytical, all methods where a continuous formulation of MAXWELL's equations is solved and no discretization method is applied, are called analytical methods in the scope of this work. The accuracy of the solution depends only on the precision that is used to evaluate the analytical expression. For this reason analytical approaches are commonly used to cross-check results that have been obtained experimentally or numerically. For two selected geometries an analytical procedure will be presented in chapter 4.

3.6.2 Numerical methods

For practical applications analytical methods are insufficient: in most cases it is not possible to adapt the coordinate system to the complex geometry of actual beamline devices and/or the solution can not be obtained as a closed-form expression. To overcome this limitation, numerical simulation methods come into play which allow to treat almost any geometry. A numerical method allows to find an approximate solution of arbitrary accuracy, provided the method of choice converges. Numerical methods employ discretization schemes for time and space. The problem volume is subdivided into a sufficiently large number of volume elements where a discrete formulation of MAXWELL's equations is used to approximate the problem solution. Each operator can be assigned a discrete counterpart, such that an operator equation in continuous space can be expressed through a matrix-vector equation in discrete space. This typically leads to solving a large system of linear equations which is accomplished with the help of numerical algorithms [Saa03]:

$$\mathfrak{L} u(\vec{r}, t) = f(\vec{r}, t) \tag{3.19}$$

Different types of simulation codes have established for the solution of particle accelerator related electromagnetic problems, which differ with regard to the simulated physics and implementation. In chapter 5 an overview is given on the different categories of simulation tools. This is followed by an introduction on the Finite Integration Technique (FIT) which is the discretization technique on which the simulation tools are based, that have been used in the context of this work.

3.6.3 Experimental methods

Apparently, it is not possible to determine the coupling impedances through direct measurement of the EM field in the presence of a real particle beam: additional measuring equipment would interact with the particle beam or make beam operation impossible at all. Thus, all experimental techniques either rely on studying the effect of coupling impedances on the motion of a real particle beam [4, 35] or on bench measurement setups where the particle beam is replaced with an alternate EM field source. The bench measurement approach is typically referred to as *coaxial wire measurement technique* and will be discussed more detailed in the following.

Originally this technique stems from the approach to quantify the energy loss of a stored electron beam during its transit through an Radio Frequency (RF) cavity [18, 39]. The major challenge is to produce source fields similar to those of a charged particle beam, namely the monopolar and dipolar components. The particle beam is simulated by placing a wire on the beam axis inside the Device Under Test (DUT) creating a *coaxial line* which permits the propagation of TEM waves. Therefore it was claimed that this method applies to the approximation of an ultra-relativistic source field only [39]. There have been attempts to reproduce the source field of a non-ultrarelativistic particle beam based on slow-wave structures. Apart from being delicate in practical realization, these attempts have proven more or less promising [10].

The source field is excited by feeding a current pulse into the transmission line. The pulse shape may simulate an actual bunch profile but any pulse shape with the desired bandwidth may be used. To obtain results that are independent of the pulse shape, deconvolution must be done upon post-processing of the measured waveforms. The current in the wire must be interpreted as an impressed current J_ι not as a convection current $J_\beta = v q_V$ anymore. Consequently there is no space charge associated with the source field ($q_V = 0$ in the vacuum region).

This setup is known as *single wire measurement* which produces a pure monopolar mode if the wire runs along the axis of symmetry. A dipolar mode is created by transverse displacement of the single wire or by placing two wires with opposite displacement and opposite phase in parallel to the beam axis. This setup is known as *twin wire measurement*.

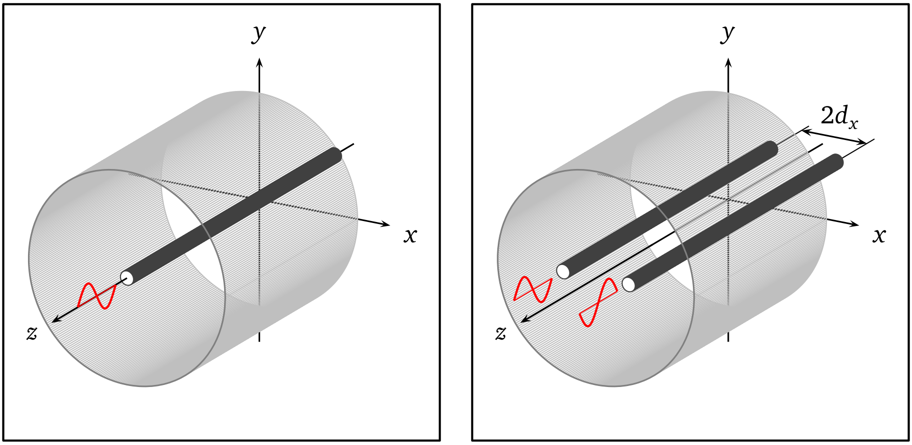

(a) single wire **(b)** twin wire

Figure 3.2.: Schematic setup for bench measurement of coupling impedance: Figures (a) and (b) illustrate the setup for a monopolar and a dipolar source field, respectively. The vacuum chamber which may contain different beamline devices under test is represented by a hollow cylinder. The twin wires are supplied with RF signals of opposite phase using 180 degree hybrid junctions [9].

Given the typical dimensions for the wire (≈ 1 mm) and the circular vacuum chamber (≈ 0.5 m), a characteristic impedance in the region of several hundreds of ohms is obtained[6] which represents a mismatch for standard laboratory equipment (50 Ω). An impedance mismatch will cause reflections which can spoil the measurement and therefore must be avoided. Impedance matching is accomplished with the help of tapered line sections or discrete resistive matching networks [9, 26].
For a Perfect Electric Conductor (PEC) with translationally invariant cross-section TEM waves propagate along the line. Lossy material or changes of the cross-section affect the transmission/reflection characteristics and withdraw energy from the pulse. Thus, it seems likely to relate these effects to the reflection and transmission coefficients $\underline{S}_{11}$ and $\underline{S}_{21}$, respectively. A differential setup can be used to study the influence of particular beamline devices by eliminating the contribution of the unloaded line. Such setup requires an additional line which serves as reference and hybrid junctions to split the input signal and subtract the output signals.

---

[6] For a cylindrical vaccum chamber made from good conducting material ($\kappa > 10^6$ S/m), the characteristic impedance of a coaxial line may be used: $\underline{Z}_{\text{coax line}} = \frac{Z_0}{2\pi} \ln\left(\frac{\varrho_2}{\varrho_1}\right)$, $\varrho_1 < \varrho_2$

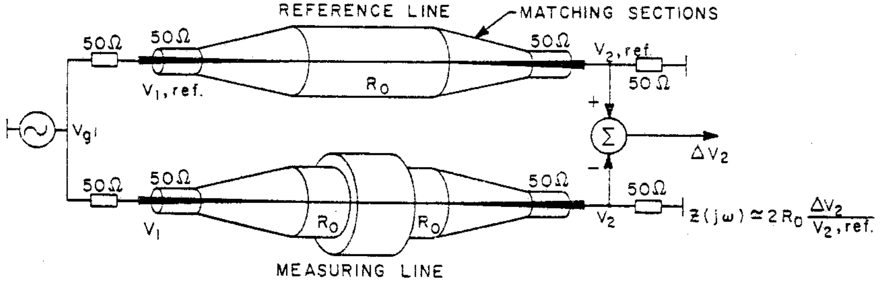

Figure 3.3.: Practical realization of a bench setup for the measurement of the longitudinal coupling impedance [26]: The schematic shows a coaxial line with the DUT attached and an optional reference line which can be used for differential measurement to study the influence of the DUT.

In the course of technical development pulse generators and analog oscilloscopes have been replaced by fully-automated vector network analyzers which allow for waveform storage and mathematical post-processing. Thus, all measurements can be performed sequencially and time domain gating can be used to suppress reflected pulses.

The interpretation and validity of coupling impedance measurement results using the coaxial wire technique has been discussed by many authors including [9, 15, 21, 23, 24, 26]. Most authors agree that this method is a useful tool if certain criteria are met. A priori knowledge is required about the type and order of magnitude of the expected impedance contributions. These measurements are mechanically and electrically sensitive towards perturbation caused by vibration, wire sag and temperature changes. Thus, expertise is required upon practical realization. When establishing a correlation between the influence of the DUT and the S-parameters of the coaxial line it is necessary to distinguish between two different situations in terms of *electrical length*. The electrical length $\theta_L = 2\pi L/\lambda$ corresponds to the phase advance for a physical dimension L referenced to a given wavelength λ and thus describes the relative size of an electrical component.

- lumped element impedances, $\theta_L/2\pi << 1$: The lossy section has negligible length and may therefore be treated as a single localized element between ideal line sections.

- distributed impedances, $\theta_L/2\pi >> 1$: The lossy section has non-neglible length and must be accounted for as lossy line.

For the sake of completeness the most commonly used relations are listed in the following. By cascading the scattering matrices of multiple 2-port devices the following expression is obtained for a single lumped element [26]:

$$\underline{Z}_{||\mathrm{meas}} = 2\underline{Z}_{\mathrm{line}} \left(\frac{1 - \underline{S}_{21}}{\underline{S}_{21}} \right) \tag{3.20}$$

By using a reference setup a modified expression is obtained for the normalized transmission coefficient $\underline{S}_{21,\mathrm{norm}} = \underline{S}_{21,\mathrm{DUT}}/\underline{S}_{21,\mathrm{REF}}$:

$$\underline{Z}_{||\mathrm{meas}} = 2\underline{Z}_{\mathrm{line}} \left(\frac{1 - \frac{\underline{S}_{21,\mathrm{DUT}}}{\underline{S}_{21,\mathrm{REF}}}}{\frac{\underline{S}_{21,\mathrm{DUT}}}{\underline{S}_{21,\mathrm{REF}}}} \right) = 2\underline{Z}_{\mathrm{line}} \left(\frac{\underline{S}_{21,\mathrm{REF}} - \underline{S}_{21,\mathrm{DUT}}}{\underline{S}_{21,\mathrm{DUT}}} \right) \tag{3.21}$$

For distributed impedances a different expression is obtained [53]:

$$\underline{Z}_{||\mathrm{meas}} = -2\underline{Z}_{\mathrm{line}} \ln \underline{S}_{21} \tag{3.22}$$

By analogy with 3.21 this expression can be modified for the normalized transmission coefficient:

$$\underline{Z}_{||\mathrm{meas}} = -2\underline{Z}_{\mathrm{line}} \ln \left(\frac{\underline{S}_{21,\mathrm{DUT}}}{\underline{S}_{21,\mathrm{REF}}} \right) \tag{3.23}$$

The previous expressions are approximations under the premise that the impedance contribution of the DUT is small compared to the characteristic impedance of the coaxial line. A more general expression reads [28]:

$$\underline{Z}_{||\mathrm{meas}} = -2\underline{Z}_{\mathrm{line}} \ln \underline{S}_{21} \left(1 + j \frac{\ln \underline{S}_{21}}{2 \frac{\omega}{c_0} L} \right) \tag{3.24}$$

The corresponding expression for the normalized transmission coefficient reads:

$$\underline{Z}_{||\mathrm{meas}} = -2\underline{Z}_{\mathrm{line}} \ln\left(\frac{\underline{S}_{21,\mathrm{DUT}}}{\underline{S}_{21,\mathrm{REF}}}\right)\left(1 + j\frac{\ln\left(\frac{\underline{S}_{21,\mathrm{DUT}}}{\underline{S}_{21,\mathrm{REF}}}\right)}{2\frac{\omega}{c_0}L}\right) \tag{3.25}$$

Most of the recently published results that originate from coaxial wire measurements have been interpreted in the sense of these formulae. For the measurement of the transverse impedance the procedure is similar except that a dipolar source field must be created and the PANOFSKY-WENZEL theorem is applied. In the case of an off-center single wire source the source field is usually dominated by the zeroth order moment which may complicate the extraction of the effect created by the dipolar source field. For low frequencies transformer-coupling using a planar coil as representation for the dipolar source fields has been suggested as an alternate approach [32].

4 Analytical methods for coupling impedance analysis

In the previous chapter the concept of coupling impedances has been introduced which requires solving an inhomogenous EM problem. Three techniques have been characterized to address this problem whereof analytical methods are in the focus of the present chapter. The application of analytical methods is typically limited to symmetric structures; two examples each having either rotational symmetry or planar symmetry are discussed. The results serve as an a priori estimate on the one hand and as validation for results that are obtained with numerical techniques on the other hand.
Most analytical approaches have in common that a partial differential equation is transformed into a system of multiple ordinary differential equations following a method known as separation of variables. The solution is expressed as product of functions that each depend on a single variable of the underlying coordinate system:

$$\begin{aligned} &\underline{F}(x)\underline{G}(y)\underline{L}(z) && \text{(cartesian)} \\ &\underline{R}(\varrho)\underline{\Theta}(\varphi)\underline{L}(z) && \text{(circular-cylindrical)} \end{aligned}$$

The sole interest lies in wave solutions that propagate synchronously with the excitation and therefore must have the same z-dependency as the source fields. The source fields must be taken into account through suitable matching conditions.

4.1 Rotational-symmetric multi-layer problem

The multi-layer problem with rotational symmetry has been widely addressed by different authors ([36, 37, 30, 25, 31]. The procedure is introduced here for the sake of completeness only. Less general expressions follow in the subsequent sections. Cylindrical coordinates are used to adapt to the rotational-symmetric geometry of the problem, thus $\vec{r}_\perp = \varrho\vec{e}_\varrho$ and $r_\perp = \varrho$. The wave equations are separately formulated for the longitudinal electric and magnetic field to distinguish between E_z- modes and H_z- modes:

$$\left(\frac{1}{\varrho}\frac{\partial}{\partial\varrho}\left(\varrho\frac{\partial}{\partial\varrho}\right)+\frac{1}{\varrho^2}\frac{\partial^2}{\partial\varphi^2}+\frac{\partial^2}{\partial z^2}+\omega^2\underline{\mu\varepsilon}\right)\underline{E}_z=\frac{1}{\varepsilon_0}\frac{\partial}{\partial z}\underline{q}_V+j\omega\mu_0 v\underline{q}_V \tag{4.1a}$$

$$\left(\frac{1}{\varrho}\frac{\partial}{\partial\varrho}\left(\varrho\frac{\partial}{\partial\varrho}\right)+\frac{1}{\varrho^2}\frac{\partial^2}{\partial\varphi^2}+\frac{\partial^2}{\partial z^2}+\omega^2\underline{\mu\varepsilon}\right)\underline{H}_z=0 \tag{4.1b}$$

The RHS vanishes for domains that are free of sources. The homogenous solution can be found through separation of variables [Jac99], which results in the following expression for both the electric and magnetic field:

$$\underline{\Theta}\,\underline{L}\frac{1}{\varrho}\frac{\partial}{\partial\varrho}\left(\varrho\frac{\partial}{\partial\varrho}\underline{R}\right)+\underline{R}\,\underline{L}\frac{1}{\varrho^2}\frac{\partial^2}{\partial\varphi^2}\underline{\Theta}+\underline{R}\,\underline{\Theta}\frac{\partial^2}{\partial z^2}\underline{L}+\omega^2\underline{\mu\varepsilon}\,\underline{R}\,\underline{\Theta}\,\underline{L}=0 \tag{4.2}$$

Separation of the variables yields the following differential equations:

$$\frac{1}{\underline{\Theta}}\frac{\partial^2}{\partial\varphi^2}\underline{\Theta}=\varrho^2\left(-\frac{1}{\underline{R}}\frac{1}{\varrho}\frac{\partial}{\partial\varrho}\left(\varrho\frac{\partial}{\partial\varrho}\underline{R}\right)-\frac{1}{\underline{L}}\frac{\partial^2}{\partial z^2}\underline{L}-\omega^2\underline{\mu\varepsilon}\right)=-m^2 \tag{4.3a}$$

$$\frac{1}{\underline{L}}\frac{\partial^2}{\partial z^2}\underline{L}=-\frac{1}{\underline{R}}\frac{1}{\varrho}\frac{\partial}{\partial\varrho}\left(\varrho\frac{\partial}{\partial\varrho}\underline{R}\right)-\frac{1}{\varrho^2}\frac{1}{\underline{\Theta}}\frac{\partial^2}{\partial\varphi^2}\underline{\Theta}-\omega^2\underline{\mu\varepsilon}=-k_z^2 \tag{4.3b}$$

Wave solutions that propagate sychronously with the source fields must have the same dependency on the longitudinal coordinate, thus $\underline{L}$ is predetermined by the previously defined sources. $\underline{\Theta}$ must be periodic with respect to integer multiples of 2π due to the rotational symmetry. The symmetry planes of the dipolar magnetic and electric fields are orthogonal to each other. Without loss of generality, the cosine function is chosen for $\underline{\Theta}_E$ leaving the sine function for $\underline{\Theta}_H$:

$$\underline{L}_{E,H}(z)\propto e^{-jk_z z} \tag{4.4a}$$

$$\underline{\Theta}_E(\varphi)\propto\cos(m_E\varphi) \tag{4.4b}$$

$$\underline{\Theta}_H(\varphi)\propto\sin(m_H\varphi) \tag{4.4c}$$

The parameter m is called azimuthal mode number or azimuthal order. m must be a natural number including zero ($m\in\mathbb{N}^{\geq 0}$). The radial dependency of the solution is given by the modified BESSEL differential equation of azimuthal order

m after substituting $\underline{L}$ and $\underline{\Theta}$ with the corresponding expressions in equation 4.2 ($\partial^2/\partial z^2 = -k_z^2$ and $\partial^2/\partial\varphi^2 = -m^2$):

$$\underbrace{\frac{1}{\varrho}\frac{\partial}{\partial\varrho}\left(\varrho\frac{\partial}{\partial\varrho}\underline{R}\right)}-\frac{m^2}{\varrho^2}\underline{R}-k_z^2\underline{R}+\omega^2\underline{\mu}\,\underline{\varepsilon}\,\underline{R}=0 \tag{4.5a}$$

$$\varrho^2\frac{\partial^2}{\partial\varrho^2}\underline{R}+\varrho\frac{\partial}{\partial\varrho}\underline{R}-\left(m^2+\varrho^2\left(k_z^2-\omega^2\underline{\mu}\underline{\varepsilon}\right)\right)\underline{R}=0 \tag{4.5b}$$

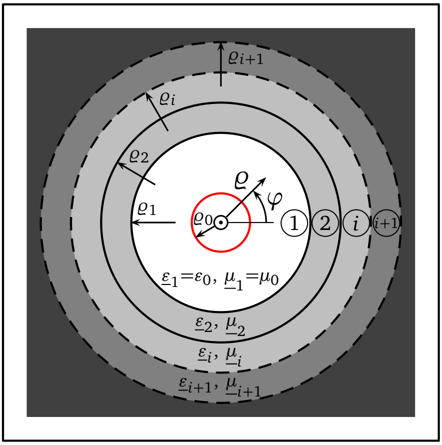

Figure 4.1.: Multilayer problem in circular-cylindrical coordinates containing a vacuum region ($0 \leq \varrho \leq \varrho_1$) in the center and an arbitrary number of concentrical layers which are characterized by index number $i \in \mathbb{N}^{\geq 1}$ and the material parameters $\underline{\varepsilon}_i$, $\underline{\mu}_i$.
The particle beam is represented by a cylinder of radius ϱ_0 extending along the z-axis which emerges perpendicularly from the drawing level.
The structure is translationally invariant and can be treated as a quasi-2D problem.

The radial wave number k_ϱ is obtained through the separation equation:

$$-k_\varrho^2+k_z^2=\omega^2\underline{\mu}\underline{\varepsilon} \;\Rightarrow\; k_\varrho=\sqrt{k_z^2-\omega^2\underline{\mu}\underline{\varepsilon}}=k_z\sqrt{1-\beta^2\underline{\mu}_\mathrm{r}\left(\underline{\varepsilon}_\mathrm{r}-j\frac{\kappa}{\varepsilon_0\omega}\right)} \tag{4.6}$$

Special cases of interest include vacuum ($\underline{\mu}_\mathrm{r}, \underline{\varepsilon}_\mathrm{r}=1,\ \kappa=0$):

$$k_{\varrho,\mathrm{vac}}=k_z\sqrt{1-\beta^2}=\frac{k_z}{\gamma} \tag{4.7a}$$

good conductors (lossy metal) ($\underline{\mu}_\mathrm{r}=1,\ \underline{\varepsilon}_\mathrm{r}=1,\ 0\ll\kappa<\infty$):

$$k_{\varrho,\mathrm{met}}=k_z\sqrt{1-\beta^2\left(1-j\frac{\kappa}{\varepsilon_0\omega}\right)} \tag{4.7b}$$

ferrite material ($\underline{\mu}_\mathrm{r} = \mu'_\mathrm{r} - j\mu''_\mathrm{r}$, $\underline{\varepsilon}_\mathrm{r} = \varepsilon'_\mathrm{r}, \kappa = 0$):

$$k_{\varrho,\mathrm{fer}} = k_z \sqrt{1 - \beta^2 \underline{\mu}_\mathrm{r} \varepsilon'_\mathrm{r}} \tag{4.7c}$$

and dielectric material ($\underline{\mu}_\mathrm{r} = 1$, $\underline{\varepsilon}_\mathrm{r} = \varepsilon'_\mathrm{r} - j\varepsilon''_\mathrm{r}$, $\kappa = 0$):

$$k_{\varrho,\mathrm{iso}} = k_z \sqrt{1 - \beta^2 \underline{\mu}_\mathrm{r} \underline{\varepsilon}_\mathrm{r}} \tag{4.7d}$$

The solutions of the modified Bessel differential equation are given by the modified Bessel functions [AS72]:

$$\underline{R}_{E,H}(\varrho) \propto \left\{ \begin{array}{c} \underline{I}_{m_E,m_H}(k_\varrho \varrho) \\ \underline{K}_{m_E,m_H}(k_\varrho \varrho) \end{array} \right\} \tag{4.8}$$

For each layer i the longitudinal electric and magnetic field reads:

$$\underline{E}_{z,i}(\varrho,\varphi,z) = \left(\underline{C}_{E,I,i}\underline{I}_{m_E}(k_{\varrho,i}\varrho) + \underline{C}_{E,K,i}\underline{K}_{m_E}(k_{\varrho,i}\varrho)\right)\cos(m_E\varphi)e^{-jk_z z} \tag{4.9a}$$

$$\underline{H}_{z,i}(\varrho,\varphi,z) = \left(\underline{C}_{H,I,i}\underline{I}_{m_H}(k_{\varrho,i}\varrho) + \underline{C}_{H,K,i}\underline{K}_{m_H}(k_{\varrho,i}\varrho)\right)\sin(m_H\varphi)e^{-jk_z z} \tag{4.9b}$$

The transverse field components for the two mode types are found by inserting equations 4.9a and 4.9b into Maxwell's equations:

$$\left[\mathrm{curl}\,\underline{\vec{H}}\right]_\varrho = \frac{1}{\varrho}\frac{\partial}{\partial\varphi}\underline{H}_z - \frac{\partial}{\partial z}\underline{H}_\varphi = j\omega\underline{\varepsilon}\underline{E}_\varrho \tag{4.10a}$$

$$\left[\mathrm{curl}\,\underline{\vec{H}}\right]_\varphi = \frac{\partial}{\partial z}\underline{H}_\varrho - \frac{\partial}{\partial\varrho}\underline{H}_z = j\omega\underline{\varepsilon}\underline{E}_\varphi \tag{4.10b}$$

$$\left[\mathrm{curl}\,\underline{\vec{E}}\right]_\varrho = \frac{1}{\varrho}\frac{\partial}{\partial\varphi}\underline{E}_z - \frac{\partial}{\partial z}\underline{E}_\varphi = -j\omega\underline{\mu}\underline{H}_\varrho \tag{4.10c}$$

$$\left[\mathrm{curl}\,\underline{\vec{E}}\right]_\varphi = \frac{\partial}{\partial z}\underline{E}_\varrho - \frac{\partial}{\partial\varrho}\underline{E}_z = -j\omega\underline{\mu}\underline{H}_\varphi \tag{4.10d}$$

The transverse field components can be expressed in terms of the longitudinal field components by pairwise combination of equations 4.10a to 4.10d after differentiating with respect to the longitudinal coordinate z [31]:

$$\left(\frac{\partial^2}{\partial z^2}+\omega^2\underline{\mu\varepsilon}\right)\underline{E}_\varrho = -jk_z\frac{\partial}{\partial\varrho}\underline{E}_z - j\omega\underline{\mu}\frac{1}{\varrho}\frac{\partial}{\partial\varphi}\underline{H}_z \tag{4.11a}$$

$$\left(\frac{\partial^2}{\partial z^2}+\omega^2\underline{\mu\varepsilon}\right)\underline{E}_\varphi = -jk_z\frac{1}{\varrho}\frac{\partial}{\partial\varphi}\underline{E}_z + j\omega\underline{\mu}\frac{\partial}{\partial\varrho}\underline{H}_z \tag{4.11b}$$

$$\left(\frac{\partial^2}{\partial z^2}+\omega^2\underline{\mu\varepsilon}\right)\underline{H}_\varrho = j\omega\underline{\varepsilon}\frac{1}{\varrho}\frac{\partial}{\partial\varphi}\underline{E}_z - jk_z\frac{\partial}{\partial\varrho}\underline{H}_z \tag{4.11c}$$

$$\left(\frac{\partial^2}{\partial z^2}+\omega^2\underline{\mu\varepsilon}\right)\underline{H}_\varphi = -j\omega\underline{\varepsilon}\frac{\partial}{\partial\varrho}\underline{E}_z - jk_z\frac{1}{\varrho}\frac{\partial}{\partial\varphi}\underline{H}_z \tag{4.11d}$$

After substituting $\partial/\partial z \rightarrow -jk_z$ and $k_\varrho = \sqrt{k_z^2 - \omega^2\underline{\mu\varepsilon}}$ the transverse electric and magnetic field for each layer i read:

$$\underline{E}_{\varrho,i} = j\frac{k_z}{k_{\varrho,i}^2}\left(\frac{\partial}{\partial\varrho}\underline{E}_{z,i} + \frac{\nu\underline{\mu}_i}{\varrho}\frac{\partial}{\partial\varphi}\underline{H}_{z,i}\right) \tag{4.12a}$$

$$\underline{E}_{\varphi,i} = j\frac{k_z}{k_{\varrho,i}^2}\left(\frac{1}{\varrho}\frac{\partial}{\partial\varphi}\underline{E}_{z,i} - \nu\underline{\mu}_i\frac{\partial}{\partial\varrho}\underline{H}_{z,i}\right) \tag{4.12b}$$

$$\underline{H}_{\varrho,i} = j\frac{k_z}{k_{\varrho,i}^2}\left(-\frac{\nu\underline{\varepsilon}_i}{\varrho}\frac{\partial}{\partial\varphi}\underline{E}_{z,i} + \frac{\partial}{\partial\varrho}\underline{H}_{z,i}\right) \tag{4.12c}$$

$$\underline{H}_{\varphi,i} = j\frac{k_z}{k_{\varrho,i}^2}\left(\nu\underline{\varepsilon}_i\frac{\partial}{\partial\varrho}\underline{E}_{z,i} + \frac{1}{\varrho}\frac{\partial}{\partial\varphi}\underline{H}_{z,i}\right) \tag{4.12d}$$

In the general case E_z- and H_z- modes are cross-coupled (hybrid modes). E_z- and H_z- modes are decoupled for the special case of $m = 0$ including only the monopolar fields created by a non-displaced beam :

$$\underline{E}_{z,i} = \left(\underline{C}_{I,i}\underline{I}_m(k_{\varrho,i}\varrho) + \underline{C}_{K,i}\underline{K}_m(k_{\varrho,i}\varrho)\right)e^{-jk_zz} \tag{4.13a}$$

$$\underline{E}_{\varrho,i} = j\frac{k_z}{k_{\varrho,i}^2}\frac{\partial}{\partial\varrho}\underline{E}_{z,i} \tag{4.13b}$$

$$\underline{H}_{\varphi,i} = j\frac{k_z}{k_{\varrho,i}^2}\nu\underline{\varepsilon}_i\frac{\partial}{\partial\varrho}\underline{E}_{z,i} \tag{4.13c}$$

The case of $m = 1$ includes the dipolar fields produced by a displaced beam and introduces cross-coupling between the two mode types. Equations 4.9 and 4.12 allow to formulate an EM field solution for each layer that is free of sources. The vacuum region in the center requires special attention to account for the source fields which are defined as follows:

$$\underline{q}_V(\varrho,\varphi,z,\omega) = \sum_{m=0}^{\infty} \frac{Q_{\text{beam}} d^m \cos(m\varphi)}{\pi v d^{m+1}(1+\delta_{m0})} \delta(\varrho-d) e^{-jk_z z} \tag{4.14a}$$

$$\approx \underbrace{\frac{Q_{\text{beam}}}{2\pi v d} \delta(\varrho-d) e^{-jk_z z}}_{\text{monopolar}} + \underbrace{\frac{Q_{\text{beam}}}{\pi v d^2} d \cos(m\varphi) \delta(\varrho-d) e^{-jk_z z}}_{\text{dipolar}} \tag{4.14b}$$

Equation 4.14 slightly differs from the previous notation provided in chapter 2.5. The dipolar contribution matches equation 2.35 for $d \rightarrow d_x$ while the monopolar contribution represents a ring rather than a disc. This notation allows to express all moments of the source distribution by means of a single DIRAC delta function. The difference predominantly affects the result for the space charge impedance. A detailed discussion about the impact of the different source definitions can be found in [3]. The BESSEL functions of the second type show singular behaviour in the limit $\varrho \rightarrow 0$ and must be excluded from the solution in the particle beam region:

$$\lim_{\varrho \to 0} \left| \underline{K}_m \right| \rightarrow \infty \;\; \forall m \in \mathbb{N}^{\geq 0} \Rightarrow \underline{C}_{E,K,0} = \underline{C}_{H,K,0} = 0 \tag{4.15}$$

According 4.14 all moments of the sources are allocated along the perimeter of a circular cylinder. $\underline{E}_z$ and $\underline{H}_z$ represent tangential components which must fulfill certain conditions at the cylinder interface given by $\varrho = \varrho_0$, $z \in \mathbb{R}$. The tangential component of the electric field must always be continuous:

$$\underline{E}_{z,0}(\varrho,\varphi,z)\Big|_{\varrho=\varrho_0} = \underline{E}_{z,1}(\varrho,\varphi,z)\Big|_{\varrho=\varrho_0} \tag{4.16a}$$

$$\cos(m_{E,0}\varphi)\underline{C}_{I,E,0}\underline{I}_{m_{E,0}}(k_{\varrho,0}\varrho_0) = \cos(m_{E,1}\varphi)\left(\underline{C}_{I,E,1}\ \underline{I}_{m_{E,1}}(k_{\varrho,1}\varrho_0) + \underline{C}_{K,E,1}\underline{K}_{m_{E,1}}(k_{\varrho,1}\varrho_0)\right) \tag{4.16b}$$

This condition must apply for any azimuthal angle $\varphi \in [0, 2\pi]$ which is fulfilled for $m_{E,0} = m_{E,1} = m_E$. After substituting $k_{\varrho,0} = k_{\varrho,1} = k_{\varrho,\mathrm{vac}} = k_z/\gamma$, the following relation is obtained:

$$\underline{C}_{I,E,0} - \underline{C}_{I,E,1} = \underline{C}_{K,E,1} \frac{\underline{K}_{m_E}(\frac{k_z}{\gamma}\varrho_0)}{\underline{I}_{m_E}(\frac{k_z}{\gamma}\varrho_0)} \tag{4.17}$$

Rewriting the wave equation for the vacuum region ($\varrho \leq \varrho_1$, $\underline{\varepsilon}_i \underline{\mu}_i = \varepsilon_0 \mu_0 \forall i \leq 1$) yields:

$$\left(\frac{1}{\varrho}\frac{\partial}{\partial\varrho}\left(\varrho\frac{\partial}{\partial\varrho}\right) - \frac{m_E}{\varrho^2} - k_z^2 + k^2\right)\underline{E}_{z,0} = -j\underline{q}_V \frac{\omega}{\varepsilon_0 v \gamma^2} \tag{4.18}$$

Both sides of the equation are multiplied by ϱ and integration is performed along the radial coordinate [20]:

$$\begin{aligned}
&\underbrace{\int\limits_{\varrho_0-\Delta\varrho}^{\varrho_0+\Delta\varrho} \frac{\partial}{\partial\varrho}\left(\varrho\frac{\partial \underline{E}_z}{\partial\varrho}\right)\mathrm{d}\varrho}_{\to\varrho_0\left(\underline{E}'_{z,1}-\underline{E}'_{z,0}\right)} - \underbrace{\int\limits_{\varrho_0-\Delta\varrho}^{\varrho_0+\Delta\varrho} \left(\frac{m_E}{\varrho} + \varrho k_z^2\left(1-\beta^2\right)\right)\underline{E}_z\,\mathrm{d}\varrho}_{\to 0} = \\
&\qquad -j\omega\frac{Q_{\mathrm{beam}}\varrho_0^{m_E}\cos(m_E\varphi)}{\pi\varepsilon_0 v^2\gamma^2\varrho_0^{m_E+1}(1+\delta_{m0})}e^{-jk_z z}\underbrace{\int\limits_{\varrho_0-\Delta\varrho}^{\varrho_0+\Delta\varrho}\varrho\,\delta(\varrho-\varrho_0)\,\mathrm{d}\varrho}_{\to\varrho_0\delta(0)}
\end{aligned} \tag{4.19}$$

In the limit of $\Delta\varrho \to 0$ the first integral on the Left Hand Side (LHS) represents the left-sided and right-sided derivatives of E_z at the interface $\varrho = \varrho_0$ while the second integral vanishes:

$$\varrho_0\left(\left.\frac{\partial \underline{E}_{z,1}}{\partial\varrho}\right|_{\varrho=\varrho_0} - \left.\frac{\partial \underline{E}_{z,0}}{\partial\varrho}\right|_{\varrho=\varrho_0}\right) = -j\omega\frac{Q_{\mathrm{beam}}\cos(m_E\varphi)}{\pi\varepsilon_0 v^2\gamma^2(1+\delta_{m0})}e^{-jk_z z} \tag{4.20}$$

The longitudinal electric field intensity $\underline{E}_{z,i}$ is substituted with the help of equation 4.9a. After substituting $k_{\varrho,0} = k_{\varrho,1} = k_{\varrho,\mathrm{vac}} = k_z/\gamma$ the longitudinal and azimuthal expressions can be omitted.

$$\begin{aligned}\varrho_0 \frac{k_z}{\gamma}\left(\underline{C}_{I,E,1}\underline{I}'_{m_E}(\tfrac{k_z}{\gamma}\varrho_0) + \underline{C}_{K,E,1}\underline{K}'_{m_E}(\tfrac{k_z}{\gamma}\varrho_0) - \underline{C}_{I,E,0}\underline{I}'_{m_E}(\tfrac{k_z}{\gamma}\varrho_0)\right)& \\ = -j\omega \frac{Q_{\text{beam}}}{\pi\varepsilon_0 v^2\gamma^2(1+\delta_{m0})}& \qquad (4.21\text{a})\end{aligned}$$

$$\begin{aligned}\varrho_0 \frac{k_z}{\gamma}\left(\left(\underline{C}_{I,E,0} - \underline{C}_{I,E,1}\right)\underline{I}'_{m_E}(\tfrac{k_z}{\gamma}\varrho_0) - \underline{C}_{K,E,1}\underline{K}'_{m_E}(\tfrac{k_z}{\gamma}\varrho_0)\right)& \\ = j\omega \frac{Q_{\text{beam}}}{\pi\varepsilon_0 v^2\gamma^2(1+\delta_{m0})}& \qquad (4.21\text{b})\end{aligned}$$

$$\begin{aligned}\varrho_0 \frac{k_z}{\gamma}\underline{C}_{K,E,1}\left(\underline{K}_{m_E}(\tfrac{k_z}{\gamma}\varrho_0)\underline{I}'_{m_E}(\tfrac{k_z}{\gamma}\varrho_0) - \underline{K}'_{m_E}(\tfrac{k_z}{\gamma}\varrho_0)\underline{I}_{m_E}(\tfrac{k_z}{\gamma}\varrho_0)\right)& \\ = j\omega \frac{Q_{\text{beam}}}{\pi\varepsilon_0 v^2\gamma^2(1+\delta_{m0})}\underline{I}_{m_E}(\tfrac{k_z}{\gamma}\varrho_0)& \\ (4.21\text{c})&\end{aligned}$$

$\underline{C}_{K,E,1}$ is determined with the help of the BESSEL function identities (Appendix D.3):

$$\underline{C}_{K,E,1} = j\omega \frac{Q_{\text{beam}}}{\pi\varepsilon_0 v^2\gamma^2(1+\delta_{m0})}\underline{I}_{m_E}(\tfrac{k_z}{\gamma}\varrho_0) \qquad (4.22)$$

The tangential component of the the magnetic field intensity may be discontinuous in general due to the presence of surface currents. The current density $\vec{\underline{J}}_\beta = \underline{q}_V v\vec{e}_z$ is only connected with the azimuthal component of the magnetic field, thus $\underline{H}_z$ must also be continuous:

$$\underline{H}_{z,0}(\varrho,\varphi,z)\Big|_{\varrho=\varrho_0} = \underline{H}_{z,1}(\varrho,\varphi,z)\Big|_{\varrho=\varrho_0} \qquad (4.23)$$

By analogy with 4.16, the following relation is obtained:

$$\underline{C}_{I,H,0} - \underline{C}_{I,H,1} = \underline{C}_{K,H,1}\frac{\underline{K}_{m_H}(\tfrac{k_z}{\gamma}\varrho_0)}{\underline{I}_{m_H}(\tfrac{k_z}{\gamma}\varrho_0)} \qquad (4.24)$$

$\underline{C}_{K,H,1}$ is determined by adapting the previous procedure for equation 4.1b:

$$\underline{C}_{K,H,1} = 0 \;\Rightarrow\; \underline{C}_{I,H,0} = \underline{C}_{I,H,1} \qquad (4.25)$$

So far, the field matching procedure has been exemplified for the vacuum region taking the source fields into account. There exist no surface charges and currents at the interfaces for the subsequent layers with $i \geq 1$, therefore E_{tan}, D_{norm}, H_{tan} and B_{norm} must be continuous. The continuity conditions between neighbouring layers i and $i+1$ read:

$$\underline{E}_{z,i}(\varrho,\varphi,z,\omega)\Big|_{\varrho=\varrho_i} = \underline{E}_{z,i+1}(\varrho,\varphi,z,\omega)\Big|_{\varrho=\varrho_i} \tag{4.26a}$$

$$\underline{E}_{\varphi,i}(\varrho,\varphi,z,\omega)\Big|_{\varrho=\varrho_i} = \underline{E}_{\varphi,i+1}(\varrho,\varphi,z,\omega)\Big|_{\varrho=\varrho_i} \tag{4.26b}$$

$$\underline{\varepsilon}_i\underline{E}_{\varrho,i}(\varrho,\varphi,z,\omega)\Big|_{\varrho=\varrho_i} = \underline{\varepsilon}_{i+1}\underline{E}_{\varrho,i+1}(\varrho,\varphi,z,\omega)\Big|_{\varrho=\varrho_i} \tag{4.26c}$$

$$\underline{H}_{z,i}(\varrho,\varphi,z,\omega)\Big|_{\varrho=\varrho_i} = \underline{H}_{z,i+1}(\varrho,\varphi,z,\omega)\Big|_{\varrho=\varrho_i} \tag{4.26d}$$

$$\underline{H}_{\varphi,i}(\varrho,\varphi,z,\omega)\Big|_{\varrho=\varrho_i} = \underline{H}_{\varphi,i+1}(\varrho,\varphi,z,\omega)\Big|_{\varrho=\varrho_i} \tag{4.26e}$$

$$\underline{\mu}_i\underline{H}_{\varrho,i}(\varrho,\varphi,z,\omega)\Big|_{\varrho=\varrho_i} = \underline{\mu}_{i+1}\underline{H}_{\varrho,i+1}(\varrho,\varphi,z,\omega)\Big|_{\varrho=\varrho_i} \tag{4.26f}$$

The addition of each new layer introduces four new coefficients. The underlying numbering scheme (the beam region has index '0') and the previously determined coefficients for layers '0' and '1' yield a total of $4(N_{\text{layers}}-1)$ unknown coefficients remaining. This problem can be addressed by conventional solving strategies, however, an elegant and clear matrix formalism is introduced in [31] which is described more detailed in appendix C.

4.2 Rotational-symmetric half-space problem in the ultra-relativistic limit

The following simplified approach applies to ultra-relativistic beam ($\beta \to 1$) only and was presented in [49, 50]. Only the current density is taken into account as source field produced by the ultra-relativistic beam :

$$\underline{J}_z(\varrho,\varphi) = \frac{I_{\text{beam}}}{2\pi\varrho}\delta(\varrho)e^{-jk_z z} \tag{4.27}$$

The high-relativistic beam creates a pure TEM source field ($k_z \to \frac{\omega}{c_0}$):

$$\left\{ \begin{array}{c} \underline{E}_\varrho \\ \underline{H}_\varphi \end{array} \right\}_{\text{beam}} \propto \frac{1}{\varrho} \tag{4.28}$$

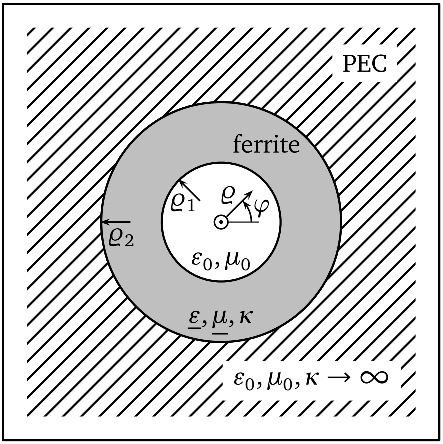

Figure 4.2.: Two-layer problem in circular-cylindrical coordinates containing a vacuum region in the center and a high permeable lossy ferrite layer adjacent to a perfect conducting half space.
The particle beam is located on the z-axis which emerges perpendicularly from the drawing level.
The structure is translationally invariant and can be treated as a quasi-2D problem.

Thus, AMPERE's law is fulfilled by:

$$\int_{\partial A_{\text{beam}}} \underline{\vec{H}} \cdot \mathrm{d}\vec{s} = \int_{A_{\text{beam}}} \underline{\vec{J}} \cdot \mathrm{d}\vec{A} \rightarrow 2\pi\varrho \underline{H}_\varphi = I_{\text{beam}} \tag{4.29}$$

The TEM solution for the source field reads:

$$\underline{H}_{\varphi,\text{beam}}(\varrho, z, \omega) = \frac{I_{\text{beam}}}{2\pi\varrho} e^{-j\frac{\omega}{c_0}z} \tag{4.30a}$$

$$\underline{E}_{\varrho,\text{beam}}(\varrho, z, \omega) = Z_0 \underline{H}_\varphi = \frac{Z_0 I_{\text{beam}}}{2\pi\varrho} e^{-j\frac{\omega}{c_0}z} \tag{4.30b}$$

Furthermore a Transverse Magnetic (TM) mode is assumed for the vacuum region ($\varrho < \varrho_1$) which introduces an additional longitudinal component for the electric field. The radial wave number vanishes in the limit of $k_z \to k_{\text{vac}} = \frac{\omega}{c_0}$ which allows to use small-argument limits for the BESSEL functions [AS72]:

$$\underline{E}_{z,\text{vac}}(z) = \underline{A}_1 e^{-j\frac{\omega}{c_0}z} \tag{4.31a}$$

$$\underline{E}_{\varrho,\text{vac}}(\varrho, z) = j\underline{A}_1 \frac{k\varrho}{2} e^{-j\frac{\omega}{c_0}z} \tag{4.31b}$$

$$\underline{H}_{\varphi,\text{vac}}(\varrho, z) = j\frac{\underline{A}_1}{Z_0}\frac{k\varrho}{2} e^{-j\frac{\omega}{c_0}z} \tag{4.31c}$$

The field solution inside the ferrite region ($\varrho_1 \leq \varrho \leq \varrho_2$) is expressed with HANKEL functions of zeroth and first order. The radial wave number is obtained through the separation equation $k_\varrho = \sqrt{\omega^2 \underline{\mu}\underline{\varepsilon} - k_z^2} = k\sqrt{\underline{\mu}_{\mathrm{r}}\underline{\varepsilon}_{\mathrm{r}} - 1}$:

$$\underline{E}_{z,\mathrm{fer}}(\varrho,z) = \left(\underline{B}_1\, \underline{H}_0^{(2)}(k_\varrho \varrho) + \underline{C}_1\, \underline{H}_0^{(1)}(k_\varrho \varrho)\right) e^{-j\frac{\omega}{c_0}z} \tag{4.32a}$$

$$\underline{E}_{\varrho,\mathrm{fer}}(\varrho,z) = j\frac{k}{k_\varrho}\left(\underline{B}_1\, \underline{H}_1^{(2)}(k_\varrho \varrho) + \underline{C}_1\, \underline{H}_1^{(1)}(k_\varrho \varrho)\right) e^{-j\frac{\omega}{c_0}z} \tag{4.32b}$$

$$\underline{H}_{\varphi,\mathrm{fer}}(\varrho,z) = j\frac{k\underline{\varepsilon}_{\mathrm{r}}}{Z_0 k_\varrho}\left(\underline{B}_1\, \underline{H}_1^{(2)}(k_\varrho \varrho) + \underline{C}_1\, \underline{H}_1^{(1)}(k_\varrho \varrho)\right) e^{-j\frac{\omega}{c_0}z} \tag{4.32c}$$

The coefficients $\underline{A}_1, \underline{B}_1, \underline{C}_1$ are determined by solving the linear equation system given by the boundary and continuity conditions at $\varrho = \varrho_1$ and $\varrho = \varrho_2$.
While the tangential electric field must always be continuous, the azimuthal magnetic field may be discontinuous due to the beam current.

$$\left.\underline{E}_{z,\mathrm{vac}}(\varrho,z)\right|_{\varrho=\varrho_1} = \left.\underline{E}_{z,\mathrm{fer}}(\varrho,z)\right|_{\varrho=\varrho_1} \tag{4.33a}$$

$$\left.\varepsilon \underline{E}_{\varrho,\mathrm{beam}}(\varrho,z) + \varepsilon \underline{E}_{\varrho,\mathrm{vac}}(\varrho,z)\right|_{\varrho=\varrho_1} = \left.\underline{\varepsilon}\, \underline{E}_{\varrho,\mathrm{fer}}(\varrho,z)\right|_{\varrho=\varrho_1} \tag{4.33b}$$

$$\left.\underline{E}_{z,\mathrm{fer}}(\varrho,z)\right|_{\varrho=\varrho_2} = 0 \tag{4.33c}$$

The individual field components are visualized in figure 4.3. The longitudinal coupling impedance is calculated by integrating the longitudinal electric field along the length L of the structure divided by the current:

$$\underline{Z}_{||} = j\frac{Z_0 L}{2\pi\varrho_1}\left[\frac{\underline{H}_0^{(1)}(k_\varrho \varrho_2)\underline{H}_1^{(2)}(k_\varrho \varrho_1) - \underline{H}_0^{(2)}(k_\varrho \varrho_2)\underline{H}_1^{(1)}(k_\varrho \varrho_1)}{\underline{H}_0^{(1)}(k_\varrho \varrho_2)\underline{H}_0^{(2)}(k_\varrho \varrho_1) - \underline{H}_0^{(2)}(k_\varrho \varrho_2)\underline{H}_0^{(1)}(k_\varrho \varrho_1)}\frac{k\underline{\varepsilon}_{\mathrm{r}}}{k_\varrho} - \frac{k\varrho_1}{2}\right]^{-1} \tag{4.34}$$

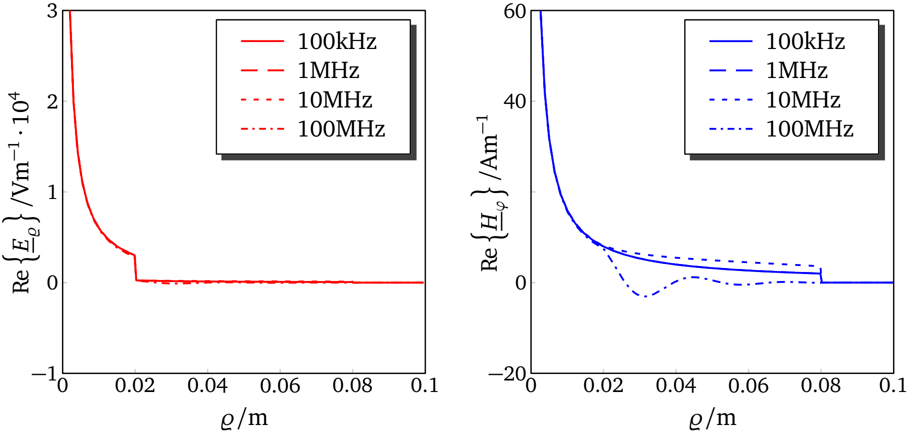

(a) **(b)**

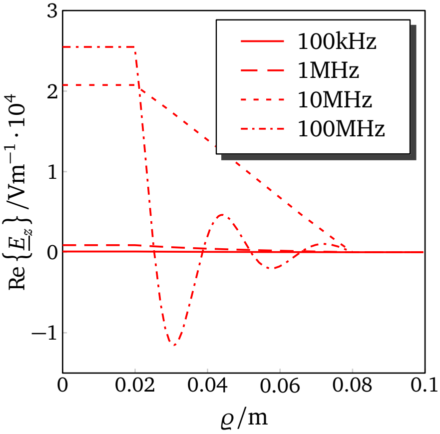

(c)

Figure 4.3.: The radial, azimuthal and longitudinal field components are evaluated in the transverse plane at $z = 0$ and plotted versus the radial coordinate. All components show frequency-dependent penetration into the ferrite material.
The relative complex permeability has been preset to an exemplary value $\underline{\mu}_{\mathrm{r}} = 1000 - j500$ to suppress the influence of material characteristics. The longitudinal electric field $\underline{E}_z$ is of relevance for the longitudinal coupling impedance $\underline{Z}_{||}$.

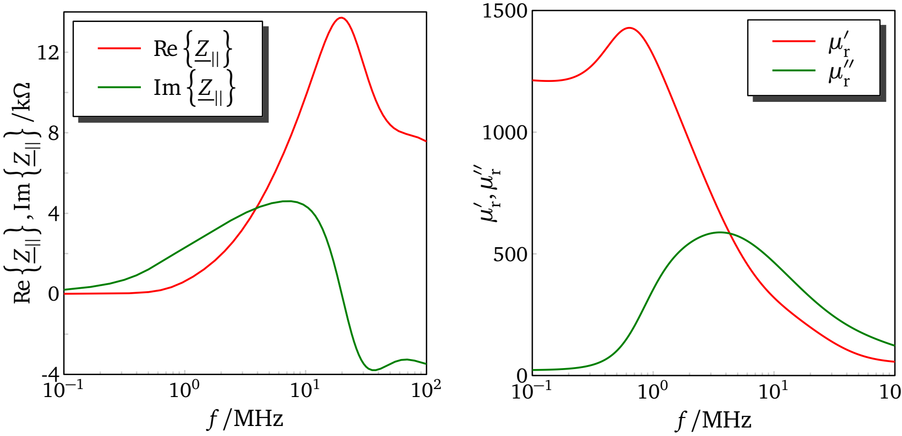

(a) **(b)**

Figure 4.4.: The dimensions have been chosen as $\varrho_1 = 20$ mm and $\varrho_2 = 80$ mm. Figure (a) shows the longitudinal coupling impedance for the rotationally-symmetric two-layer problem of unit length. The peak value is located around 20 MHz. It is correlated with the frequency where the ratio $c_0/(4f\sqrt{|\underline{\varepsilon}_{\mathrm{r}}||\underline{\mu}_{\mathrm{r}}|})$ equals the thickness $\varrho_2 - \varrho_1$ of the ferrite layer.
Figure (b) shows the frequency dependency of the underlying ferrite material (Ferroxcube 8C11). A curve has been fitted to the original manufacturer data using a modified Padé approximant.

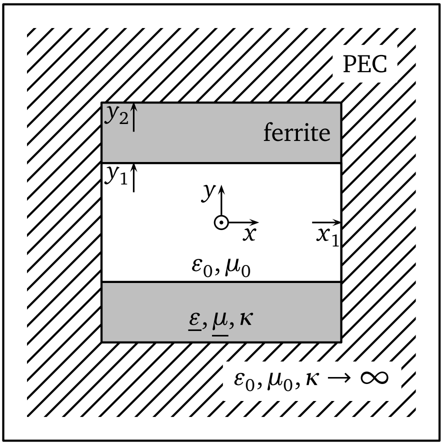

Figure 4.5.: Symmetrical two-layer problem in cartesian coordinates containing a vacuum region in the center and two high permeable lossy ferrite layers adjacent to a perfect conducting half space. The particle beam is located on the z-axis which emerges perpendicularly from the drawing level.
The structure is translationally invariant and can be treated as a quasi-2D problem.

Cartesian coordinates are used to adapt to the planar geometry. The following simplified approach applies to ultra-relativistic beam ($\beta \to 1$) only and was presented in [49, 50]. The current density is taken into account as source field produced by the ultra-relativistic particle beam :

$$\underline{J}_z(x, y) = \frac{I_{\text{beam}}}{2\pi\sqrt{x^2+y^2}}\delta(x)\delta(y)e^{-jk_z z} \tag{4.35}$$

The high-relativistic beam creates a pure TEM source field ($k_z \to \frac{\omega}{c_0}$) which is obtained through coordinate transformation of equations 4.30a and 4.30b:

$$\underline{\vec{H}}_{\text{beam}}(x, y, z, \omega) = \frac{I_{\text{beam}}}{2\pi\,(x^2+y^2)}\left(-y\vec{e}_x + x\vec{e}_y\right)e^{-j\frac{\omega}{c_0}z} \tag{4.36a}$$

$$\underline{\vec{E}}_{\text{beam}}(x, y, z, \omega) = \frac{Z_0 I_{\text{beam}}}{2\pi\,(x^2+y^2)}\left(x\vec{e}_x + y\vec{e}_y\right)e^{-j\frac{\omega}{c_0}z} \tag{4.36b}$$

The perfectly conducting boundaries at $|x| = x_1$ impose that the tangential electric field must vanish:

$$\underline{E}_y(x, y, z, \omega)\Big|_{x=x_1} = \underline{E}_y(x, y, z, \omega)\Big|_{x=-x_1} = 0 \tag{4.37}$$

This can only be accomplished by introducing a series of virtual image charges (method of images) which are located at $P_n(x_n, 0)$ with $x_n = 2nx_1,\ n \in \mathbb{Z}$. The modified source field reads:

$$\begin{pmatrix} \underline{E}_x \\ \underline{E}_y \end{pmatrix}_{\text{beam}} = \begin{pmatrix} Z_0\underline{H}_y \\ -Z_0\underline{H}_x \end{pmatrix}_{\text{beam}} \tag{4.38a}$$

$$= \frac{Z_0 I_{\text{beam}}}{2\pi} \sum_{-\infty}^{\infty} \frac{(-1)^n}{(x-2nx_1)^2 + y^2} \begin{pmatrix} x - 2nx_1 \\ y \end{pmatrix} \tag{4.38b}$$

$$= \frac{Z_0 I_{\text{beam}}}{2x_1} \frac{1}{\cosh\left(\frac{\pi}{x_1} y\right) - \cos\left(\frac{\pi}{x_1} x\right)} \begin{pmatrix} \sin\left(\frac{\pi}{2x_1} x\right) \cosh\left(\frac{\pi}{2x_1} y\right) \\ \cos\left(\frac{\pi}{2x_1} x\right) \sinh\left(\frac{\pi}{2x_1} y\right) \end{pmatrix} \tag{4.38c}$$

The solution of the wave equation is expressed as product of the functions $\underline{F}(x)$, $\underline{G}(y)$ and $\underline{L}(z)$. The scalar wave equation reads by analogy with equation 4.2:

$$\underline{G}\,\underline{L}\frac{\partial^2}{\partial x^2}\underline{F} + \underline{F}\,\underline{L}\frac{\partial^2}{\partial y^2}\underline{G} + \underline{F}\,\underline{G}\frac{\partial^2}{\partial z^2}\underline{L} + \omega^2 \underline{\mu\varepsilon}\,\underline{F}\,\underline{G}\,\underline{L} = 0 \tag{4.39}$$

Separation of the variables yields the following differential equations:

$$\frac{1}{\underline{F}} \frac{\partial^2}{\partial x^2} \underline{F} = -k_x^2 \tag{4.40a}$$

$$\frac{1}{\underline{G}} \frac{\partial^2}{\partial y^2} \underline{G} = -k_y^2 \tag{4.40b}$$

$$\frac{1}{\underline{L}} \frac{\partial^2}{\partial z^2} \underline{L} = -k_z^2 \tag{4.40c}$$

While the dependence of the solution in the longitudinal direction is predetermined by the excitation, the solutions in the transverse are given by trigonometric and hyperbolic functions:

$$\underline{F}(x) \propto \begin{cases} \left\{ \begin{matrix} \sin(k_x x) \\ \cos(k_x x) \end{matrix} \right\} & \text{for } k_x \in \quad \mathbb{R} \\ \left\{ \begin{matrix} \sinh(k_x x) \\ \cosh(k_x x) \end{matrix} \right\} & \text{for } k_x \in \quad \mathbb{C}\backslash\mathbb{R} \end{cases} \tag{4.41a}$$

$$\underline{G}(y) \propto \begin{cases} \left\{ \begin{matrix} \sin(k_y y) \\ \cos(k_y y) \end{matrix} \right\} & \text{for } k_y \in \quad \mathbb{R} \\ \left\{ \begin{matrix} \sinh(k_y y) \\ \cosh(k_y y) \end{matrix} \right\} & \text{for } k_y \in \quad \mathbb{C}\backslash\mathbb{R} \end{cases} \tag{4.41b}$$

$$\underline{L}(z) \propto e^{-j\frac{\omega}{c_0}z} \tag{4.41c}$$

In the previous sections the wave equation was solved separately for the longitudinal component of the electric and magnetic field. However, it may be purposeful to introduce vector potentials from which all components of the EM field are derived. In the limit of $k_z \to k_{\text{vac}} = \omega/c_0$ the separation equation in the vacuum region reduces to:

$$k_x^2 + k_y^2 = 0 \Rightarrow k_y = jk_x \tag{4.42}$$

With a priori knowledge of the source field, the following vector potential is formulated for the vacuum region ($|x| \leq x_1$, $|y| \leq y_1$):

$$\underline{\vec{A}}_H(\vec{r}) = \sum_{n=0}^{\infty} \left(\frac{\underline{A}_n}{k_{x,n}} \sin(k_{x,n}x)\cosh(k_{x,n}y)\vec{e}_y - \frac{\underline{B}_n}{k_{x,n}} \cos(k_{x,n}x)\sinh(k_{x,n}y)\vec{e}_x \right) e^{-jk_z z} \tag{4.43}$$

with $k_{x,n} = (2n+1)\pi/2x_1$ and $n \in \mathbb{N}_0$. The six components of the EM field are obtained through the curl operator:

$$\underline{\vec{E}}_{\text{vac}} = \operatorname{curl} \underline{\vec{A}}_H \tag{4.44a}$$

$$\underline{\vec{H}}_{\text{vac}} = -\frac{1}{j\omega\mu_0} \operatorname{curl}\operatorname{curl} \underline{\vec{A}}_H = -\frac{1}{j\omega\mu_0} \operatorname{curl} \underline{\vec{E}}_{\text{vac}} \tag{4.44b}$$

The hybrid wave solution for the electric field reads:

$$\underline{E}_{x,\mathrm{vac}} = \sum_{n=0}^{\infty} \frac{jk_z}{k_{x,n}} \underline{A}_n \sin(k_{x,n}x)\cosh(k_{x,n}y)e^{-jk_z z} \tag{4.45a}$$

$$\underline{E}_{y,\mathrm{vac}} = \sum_{n=0}^{\infty} \frac{jk_z}{k_{x,n}} \underline{B}_n \cos(k_{x,n}x)\sinh(k_{x,n}y)e^{-jk_z z} \tag{4.45b}$$

$$\underline{E}_{z,\mathrm{vac}} = \sum_{n=0}^{\infty} \left(\underline{A}_n + \underline{B}_n\right) \cos(k_{x,n}x)\cosh(k_{x,n}y)e^{-jk_z z} \tag{4.45c}$$

The hybrid wave solution for the magnetic field reads:

$$\underline{H}_{x,\mathrm{vac}} = \frac{j}{Z_0} \sum_{n=0}^{\infty} \left(\frac{k_{x,n}}{k_z} \underline{A}_n + \left(\frac{k_{x,n}}{k_z} - \frac{k_z}{k_{x,n}} \right) \underline{B}_n \right) \cos(k_{x,n}x)\sinh(k_{x,n}y)e^{-jk_z z} \tag{4.46a}$$

$$\underline{H}_{y,\mathrm{vac}} = \frac{j}{Z_0} \sum_{n=0}^{\infty} \left(\left(\frac{k_{x,n}}{k_z} + \frac{k_z}{k_{x,n}} \right) \underline{A}_n + \frac{k_{x,n}}{k_z} \underline{B}_n \right) \sin(k_{x,n}x)\cosh(k_{x,n}y)e^{-jk_z z} \tag{4.46b}$$

$$\underline{H}_{z,\mathrm{vac}} = \frac{1}{Z_0} \sum_{n=0}^{\infty} \left(\underline{A}_n + \underline{B}_n\right) \sin(k_{x,n}x)\sinh(k_{x,n}y)e^{-jk_z z} \tag{4.46c}$$

For the ferrite region the separation equation reads:

$$k_x^2 + k_y^2 = k_{\mathrm{fer}} - k_z^2 = \underbrace{\varepsilon_0\mu_0}_{c_0^{-2}} \underline{\varepsilon}_{\mathrm{r}}\underline{\mu}_{\mathrm{r}}\,\omega^2 - \frac{\omega^2}{c_0^2} = \left(\underline{\varepsilon}_{\mathrm{r}}\underline{\mu}_{\mathrm{r}} - 1\right) k_z^2 \tag{4.47}$$

The tangential electric field must vanish at the boundaries to the perfectly conducting background at $|x| = x_1$ and $|y| = y_2$:

$$\underline{E}_z(x,y,z,\omega)\Big|_{|x|=x_1} = 0 \tag{4.48a}$$

$$\underline{E}_z(x,y,z,\omega)\Big|_{|x|=x_1} = 0 \tag{4.48b}$$

$$\underline{E}_x(x,y,z,\omega)\Big|_{|y|=y_2} = 0 \tag{4.48c}$$

$$\underline{E}_y(x,y,z,\omega)\Big|_{|y|=y_2} = 0 \tag{4.48d}$$

The EM field in the ferrite region is formulated as E_z- modes and H_z- modes taking the above conditions into account:

$$\underline{E}_{z,\text{fer}}(\vec{r},\omega) = \sum_{n=0}^{\infty} \underline{C}_n \cos(k_{x,n}x)\sin\left(k_{y,n}(y-y_2)\right) \tag{4.49a}$$

$$\underline{H}_{z,\text{fer}}(\vec{r},\omega) = \frac{1}{Z_0}\sum_{n=0}^{\infty} \underline{D}_n \sin(k_{x,n}x)\cos\left(k_{y,n}(y-y_2)\right) \tag{4.49b}$$

The transverse field components for the two mode types are found by inserting equations 4.49a and 4.49b into MAXWELL's equations:

$$\left[\operatorname{curl}\underline{\vec{H}}\right]_x = \frac{\partial}{\partial y}\underline{H}_z - \frac{\partial}{\partial z}\underline{H}_y = j\omega\underline{\varepsilon}\underline{E}_x \tag{4.50a}$$

$$\left[\operatorname{curl}\underline{\vec{H}}\right]_y = \frac{\partial}{\partial z}\underline{H}_x - \frac{\partial}{\partial x}\underline{H}_z = j\omega\underline{\varepsilon}\underline{E}_y \tag{4.50b}$$

$$\left[\operatorname{curl}\underline{\vec{E}}\right]_x = \frac{\partial}{\partial y}\underline{E}_z - \frac{\partial}{\partial z}\underline{E}_y = -j\omega\underline{\mu}\underline{H}_x \tag{4.50c}$$

$$\left[\operatorname{curl}\underline{\vec{E}}\right]_y = \frac{\partial}{\partial z}\underline{E}_x - \frac{\partial}{\partial x}\underline{E}_z = -j\omega\underline{\mu}\underline{H}_y \tag{4.50d}$$

The transverse field components can be expressed in terms of the longitudinal field components by pairwise combination of equations 4.50a to 4.50d after differentiating with respect to the longitudinal coordinate z:

$$\left(\frac{\partial^2}{\partial z^2} + \omega^2\underline{\mu\varepsilon}\right)\underline{E}_x = -jk_z\frac{\partial}{\partial x}\underline{E}_z - j\omega\underline{\mu}\frac{\partial}{\partial y}\underline{H}_z \tag{4.51a}$$

$$\left(\frac{\partial^2}{\partial z^2} + \omega^2\underline{\mu\varepsilon}\right)\underline{E}_y = -jk_z\frac{\partial}{\partial y}\underline{E}_z + j\omega\underline{\mu}\frac{\partial}{\partial x}\underline{H}_z \tag{4.51b}$$

$$\left(\frac{\partial^2}{\partial z^2} + \omega^2\underline{\mu\varepsilon}\right)\underline{H}_x = j\omega\underline{\varepsilon}\frac{\partial}{\partial y}\underline{E}_z - jk_z\frac{\partial}{\partial x}\underline{H}_z \tag{4.51c}$$

$$\left(\frac{\partial^2}{\partial z^2} + \omega^2\underline{\mu\varepsilon}\right)\underline{H}_\varphi = -j\omega\underline{\varepsilon}\frac{\partial}{\partial x}\underline{E}_z - jk_z\frac{\partial}{\partial y}\underline{H}_z \tag{4.51d}$$

The transverse components of the modes in the ferrite region read:

$$\underline{E}_{x,\mathrm{fer}} = \frac{j}{\underline{\varepsilon}_\mathrm{r}\underline{\mu}_\mathrm{r}-1} \sum_{n=0}^{\infty} \left(\frac{k_{x,n}}{k_z}\underline{C}_n + \underline{\mu}_\mathrm{r}\frac{k_{y,n}}{k_z}\underline{D}_n \right) \sin(k_{x,n}x) \sin\left(k_{y,n}(y-d)\right) e^{-jk_z z} \tag{4.52a}$$

$$\underline{E}_{y,\mathrm{fer}} = \frac{j}{\underline{\varepsilon}_\mathrm{r}\underline{\mu}_\mathrm{r}-1} \sum_{n=0}^{\infty} \left(\underline{\mu}_\mathrm{r}\frac{k_{x,n}}{k_z}\underline{D}_n - \frac{k_{y,n}}{k_z}\underline{C}_n \right) \cos(k_{x,n}x) \cos\left(k_{y,n}(y-d)\right) e^{-jk_z z} \tag{4.52b}$$

$$\underline{H}_{x,\mathrm{fer}} = \frac{j}{Z_0\left(\underline{\varepsilon}_\mathrm{r}\underline{\mu}_\mathrm{r}-1\right)} \sum_{n=0}^{\infty} \left(\underline{\varepsilon}_\mathrm{r}\frac{k_{y,n}}{k_z}\underline{C}_n - \frac{k_{x,n}}{k_z}\underline{D}_n \right) \cos(k_{x,n}x) \cos\left(k_{y,n}(y-d)\right) e^{-jk_z z} \tag{4.52c}$$

$$\underline{H}_{y,\mathrm{fer}} = \frac{j}{Z_0\left(\underline{\varepsilon}_\mathrm{r}\underline{\mu}_\mathrm{r}-1\right)} \sum_{n=0}^{\infty} \left(\underline{\varepsilon}_\mathrm{r}\frac{k_{x,n}}{k_z}\underline{C}_n + \frac{k_{y,n}}{k_z}\underline{D}_n \right) \sin(k_{x,n}x) \sin\left(k_{y,n}(y-d)\right) e^{-jk_z z} \tag{4.52d}$$

The tangential electric and magnetic field components and the normal electric displacement at $|y| = y_1$ must be continuous. The continuity conditions for H_x and B_y produce redundant expressions due to the relations between the transverse components of the electric and magnetic field.

$$\underline{E}_{z,\mathrm{vac}}(x,y,z)\Big|_{y=y_1} = \underline{E}_{z,\mathrm{fer}}(x,y,z)\Big|_{y=y_1} \tag{4.53a}$$

$$\underline{E}_{x,\mathrm{beam}}(x,y,z)\Big|_{y=y_1} + \underline{E}_{x,\mathrm{vac}}(x,y,z)\Big|_{y=y_1} = \underline{E}_{x,\mathrm{fer}}(x,y,z)\Big|_{y=y_1} \tag{4.53b}$$

$$\underline{D}_{y,\mathrm{beam}}(x,y,z)\Big|_{y=y_1} + \underline{D}_{y,\mathrm{vac}}(x,y,z)\Big|_{y=y_1} = \underline{E}_{y,\mathrm{fer}}(x,y,z)\Big|_{y=y_1} \tag{4.53c}$$

$$\underline{H}_{z,\mathrm{vac}}(x,y,z)\Big|_{y=y_1} = \underline{H}_{z,\mathrm{fer}}(x,y,z)\Big|_{y=y_1} \tag{4.53d}$$

The coefficients $\underline{A}_n$, $\underline{B}_n$, $\underline{C}_n$ and $\underline{D}_n$ are determined by solving the corresponding system of linear equations. The longitudinal coupling impedance is calculated by integrating the longitudinal electric field along the length L of the structure and normalization with respect to the current [50]:

$$\begin{aligned}\underline{Z}_{\|} = j\frac{Z_0 L}{2x_1}\sum_{n=0}^{\infty}\Bigg[& \frac{\frac{k_{x,n}}{k_z}\left(1+\underline{\varepsilon}_{\mathrm{r}}\underline{\mu}_{\mathrm{r}}\right)\sinh(k_{x,n}y_1)\cosh(k_{x,n}y_1)}{\underline{\varepsilon}_{\mathrm{r}}\underline{\mu}_{\mathrm{r}}-1} \\ & + \frac{\frac{k_{y,n}}{k_z}\left(\underline{\mu}_{\mathrm{r}}\sinh^2(k_{x,n}y_1)\tan\left(k_{y,n}(y_1-y_2)\right)-\underline{\varepsilon}_{\mathrm{r}}\cosh^2(k_{x,n}y_1)\cot\left(k_{y,n}(y_1-y_2)\right)\right)}{\underline{\varepsilon}_{\mathrm{r}}\underline{\mu}_{\mathrm{r}}-1} \\ & - \frac{k_z}{k_{x,n}}\sinh(k_{x,n}y_1)\cosh(k_{x,n}y_1)\Bigg]^{-1}\end{aligned} \tag{4.54}$$

This approach which employs the method of images can be applied to horizontally and vertically displaced particle beams as well yielding similar expressions for the transverse-horizontal and transverse-vertical coupling impedances [48]. Instead of presenting the full formalism only the results are summarized here. The horizontal coupling impedance accounts for deflection caused by $\underline{E}_x$ and $\underline{H}_y$:

$$\begin{aligned}\underline{Z}_{x} = j\frac{Z_0 L}{2x_1}\sum_{n=0}^{\infty}\frac{k_{x,n}^2}{k_z}\Bigg[& \frac{\frac{k_{x,n}}{k_z}\left(1+\underline{\varepsilon}_{\mathrm{r}}\underline{\mu}_{\mathrm{r}}\right)\sinh(k_{x,n}y_1)\cosh(k_{x,n}y_1)}{\underline{\varepsilon}_{\mathrm{r}}\underline{\mu}_{\mathrm{r}}-1} \\ & + \frac{\frac{k_{y,n}}{k_z}\left(\underline{\mu}_{\mathrm{r}}\sinh^2(k_{x,n}y_1)\tan\left(k_{y,n}(y_1-y_2)\right)-\underline{\varepsilon}_{\mathrm{r}}\cosh^2(k_{x,n}y_1)\cot\left(k_{y,n}(y_1-y_2)\right)\right)}{\underline{\varepsilon}_{\mathrm{r}}\underline{\mu}_{\mathrm{r}}-1} \\ & - \frac{k_z}{k_{x,n}}\sinh(k_{x,n}y_1)\cosh(k_{x,n}y_1)\Bigg]^{-1}\end{aligned} \tag{4.55}$$

The vertical coupling impedance accounts for deflection caused by $\underline{E}_y$ and $\underline{H}_x$:

$$\begin{aligned}\underline{Z}_{y} = j\frac{Z_0 L}{2x_1}\sum_{n=0}^{\infty}\frac{k_{x,n}^2}{k_z}\Bigg[& \frac{\frac{k_{x,n}}{k_z}\left(1+\underline{\varepsilon}_{\mathrm{r}}\underline{\mu}_{\mathrm{r}}\right)\sinh(k_{x,n}y_1)\cosh(k_{x,n}y_1)}{\underline{\varepsilon}_{\mathrm{r}}\underline{\mu}_{\mathrm{r}}-1} \\ & + \frac{\frac{k_{y,n}}{k_z}\left(\underline{\mu}_{\mathrm{r}}\cosh^2(k_{x,n}y_1)\tan\left(k_{y,n}(y_1-y_2)\right)-\underline{\varepsilon}_{\mathrm{r}}\sinh^2(k_{x,n}y_1)\cot\left(k_{y,n}(y_1-y_2)\right)\right)}{\underline{\varepsilon}_{\mathrm{r}}\underline{\mu}_{\mathrm{r}}-1} \\ & - \frac{k_z}{k_{x,n}}\sinh(k_{x,n}y_1)\cosh(k_{x,n}y_1)\Bigg]^{-1}\end{aligned} \tag{4.56}$$

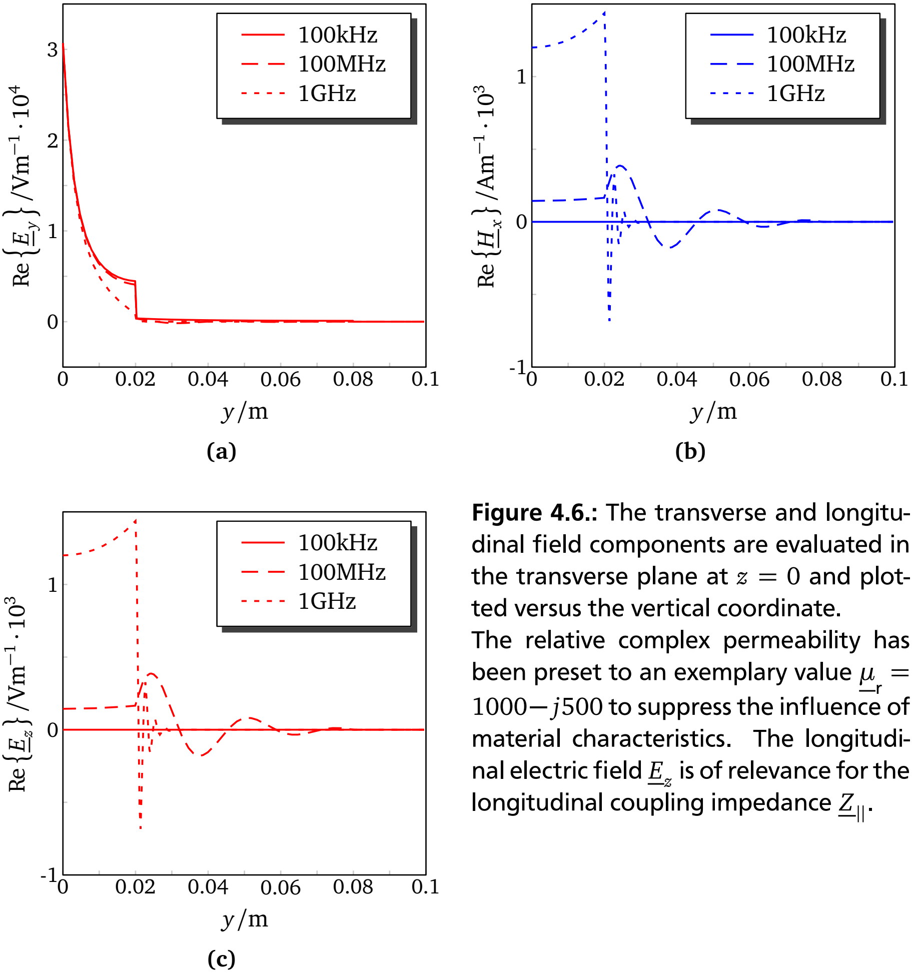

(a)

(b)

(c)

Figure 4.6.: The transverse and longitudinal field components are evaluated in the transverse plane at $z = 0$ and plotted versus the vertical coordinate.
The relative complex permeability has been preset to an exemplary value $\underline{\mu}_{\mathrm{r}} = 1000 - j500$ to suppress the influence of material characteristics. The longitudinal electric field $\underline{E}_z$ is of relevance for the longitudinal coupling impedance $\underline{Z}_{||}$.

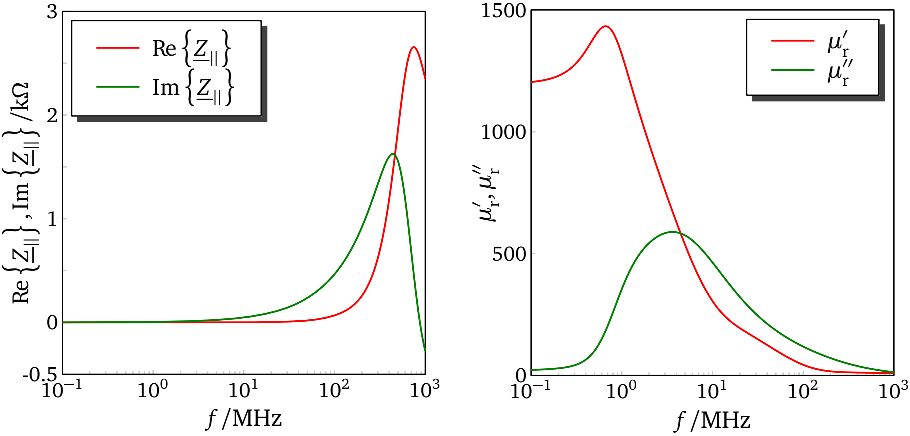

(a)

(b)

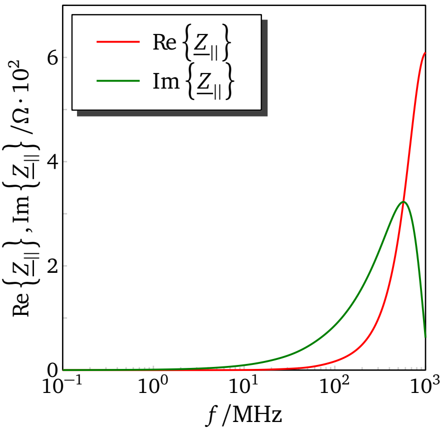

(c)

Figure 4.7.: The dimensions have been chosen as $x_1 = 67.5$ mm, $y_1 = 20$ mm and $y_2 = 80$ mm. Figure (a) shows the longitudinal coupling impedance for unit length.
Figure (c) shows the longitudinal coupling impedance for altered dimensions $y_1 = 50$ mm and $y_2 = 110$ mm to match the expected aperture dimensions of actual beamline devices for the SIS100 accelerator.

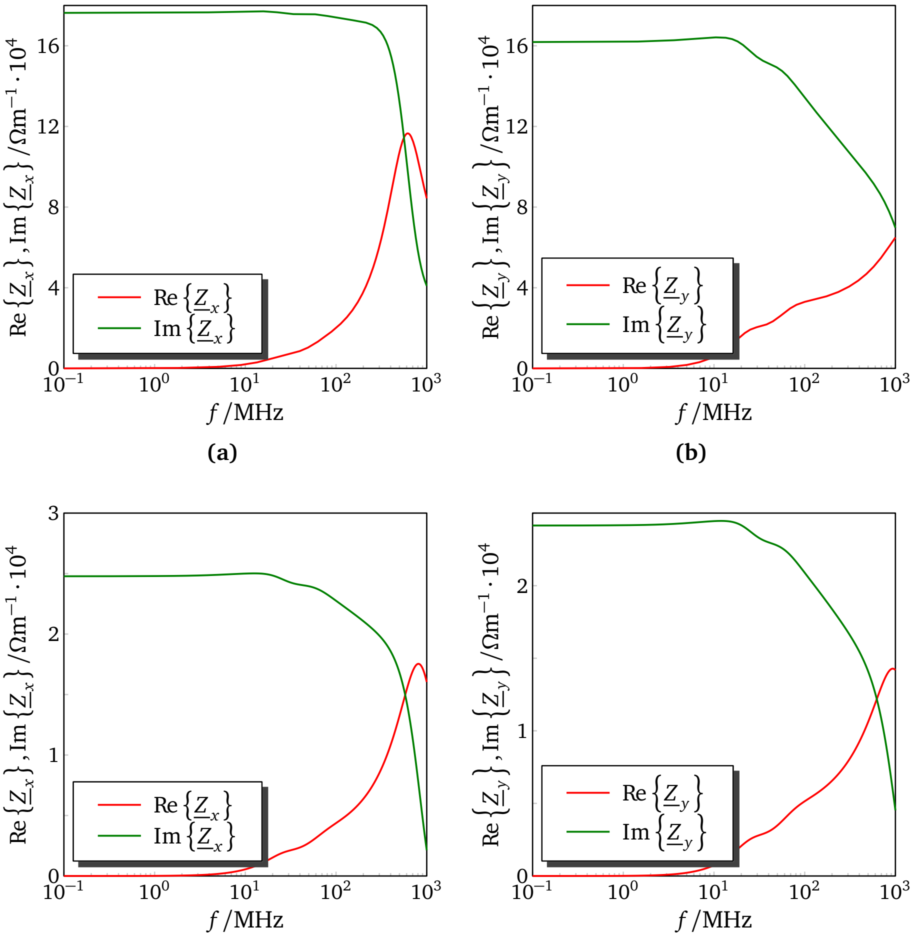

(a) **(b)**

(c) **(d)**

Figure 4.8.: The horizontal and vertical transverse coupling impedance are shown for different vertical aperture dimensions. Figures (a) and (b) refer to $y_1 = 20$ mm and $y_2 = 80$ mm. Figures (c) and (d) refer to $y_1 = 50$ mm and $y_2 = 110$ mm. The increased distance between the beam axis and the ferrite plates reduces the interaction and therefore the coupling impedance.

These examples give an idea about the EM field created by an ultra-relativistic particle beam inside ferrite-loaded beamline devices. The results serve as a first impedance estimate for the relevant components and will be compared to numerical results in the next chapter.

5 Numerical methods for coupling impedance analysis

At first, a general overview on different categories of numerical simulation tools is provided to facilitate the classification of the methods that have been used in the scope of this work. This is followed by an introduction to the FIT - a discretization method - on which the simulation approaches are based upon. A TD and a FD approach for coupling impedance analysis are introduced. The principles behind each approach are explained as well as limitations and applicability. The coupling impedance contributions will be calculated for selected benchmark geometries and compared with analytical results that have been presented in the previous chapter.

5.1 Simulation tools

By treating the particle beam as a collision-free plasma, the dynamics of a charged particle beam are given through the solutions of the VLASOV equation which describes the time evolution of the charge distribution function f (probability density function) in the presence of an EM field acting in the form of the LORENTZ force. The dynamics of the EM field are given by the solutions of MAXWELL's equations which describe the time evolution of the EM field. The sources of the EM field, in turn, are determined through the distribution of charges and currents. Thus, electrodynamics and particle dynamics are bi-directionally coupled. The only category of numerical algorithms that allows for a sufficiently accurate solution of the full six-dimensional VLASOV-MAXWELL formulation with contemporary computing resources are Particle-In-Cell (PIC) algorithms [29].

These *self-consistent* algorithms contain separate blocks for alternately solving the electrodynamics problem and the particle dynamics problem, respectively. The solution of the electrodynamics problem serves as input condition for the particle dynamics problem and vice versa. However, the facts that particle bunches are typically small compared to the beamline geometry and move with relativistic velocities make these algorithms computationally expensive.

By neglecting either type of coupling another two categories of algorithms can be obtained. Tracking algorithms neglect the influence of beam-induced EM fields on

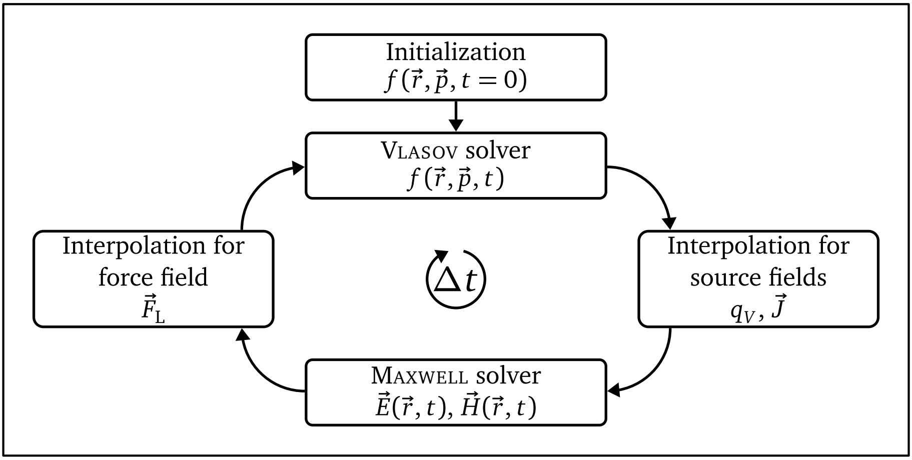

Figure 5.1.: Simplified scheme of the PIC algorithm.

the total field and solve the beam dynamics problem only. This category of algorithms is mainly applied to simulate the trajectories inside beamline components which serve the purposes of acceleration and transportation of the particle beam. There exist several modifications and related algorithms such as moment-based approaches [1, 12] and matrix-based transport algorithms.

Wakefield algorithms neglect the influence of the EM field on the trajectory and calculate the beam-induced EM field. This category of algorithms serves to simulate dissipative effects of beamline devices and the feedback action on subsequent particles.

- Particle-In-Cell algorithms: bi-directionally coupled problem, solves electrodynamics and particle dynamics problem alternately.
- Tracking algorithms: uni-directionally coupled problem, solves particle dynamics problem using precalculated EM field.
- Wakefield algorithms: uni-directionally coupled problem, solves electrodynamics problem for rigid beam source field.

The methods that have been employed in the context of this work belong to the category of wakefield algorithms which are based on TD formalisms. An alternate approach based on a FD formulation will be introduced below.

5.2 Finite Integration Technique

Numerical methods allow to find an approximative solution by replacing a continuous mathematical problem with a discrete formulation. For the case of electromagnetics the time- and space-continuous MAXWELL equations must be translated into a space- and time-discrete analogon which is accomplished by using a suitable discretization scheme. All numerical simulation work has been accomplished in the framework of the FIT which has been introduced and advanced by T. WEILAND [54]. FIT is a consistent computational method which preserves fundamental principles such as the conservation laws for charge and energy. FIT-based simulations have successfully been applied for electromagnetic problems in various fields of electrical engineering and particle accelerator related applications. In the following, the central conceptions of FIT will be summarized.

The Three dimensional (3D) computational domain consists of a bounded volume which must be discretized first. In general, volume discretization in FIT is not limited to structured orthogonal grids [14, 42]. However, cartesian grids are the prevailing type of volume discretization to be found in the context of FIT. Thereby the volume is subdivided into a finite number of cuboid-shaped subvolumes which are commonly named *mesh cells* or *volume elements*. A canonical indexing scheme assigns a unique index n to each grid point $P_n = P(n)$. The index n is determined by the grid coordinate triple $\{i, j, k\}$[1]:

$$n = (i-1)\,M_x + (j-1)\,M_y + (k-1)\,M_z \tag{5.1}$$

N_x, N_y and N_z denote the number of grid points in x-, y- and z-direction, such that $i \in \mathbb{N}^{\leq N_x}$, $j \in \mathbb{N}^{\leq N_y}$ and $k \in \mathbb{N}^{\leq N_z}$. The index increments for each direction M_x, M_y and M_z are defined as:

$$M_x = 1 \tag{5.2a}$$

$$M_y = N_x \tag{5.2b}$$

$$M_z = N_x N_y \tag{5.2c}$$

The total number of grid points N_P is directly related to the number of unknowns for the linear equation system and therefore presents an important measure for computational cost.

---

[1] The canonical indexing scheme is not mandatory. It originates from the need to use single-integer array indices to overcome limitations in early implementations. As a byproduct it allows for a more compact notation.

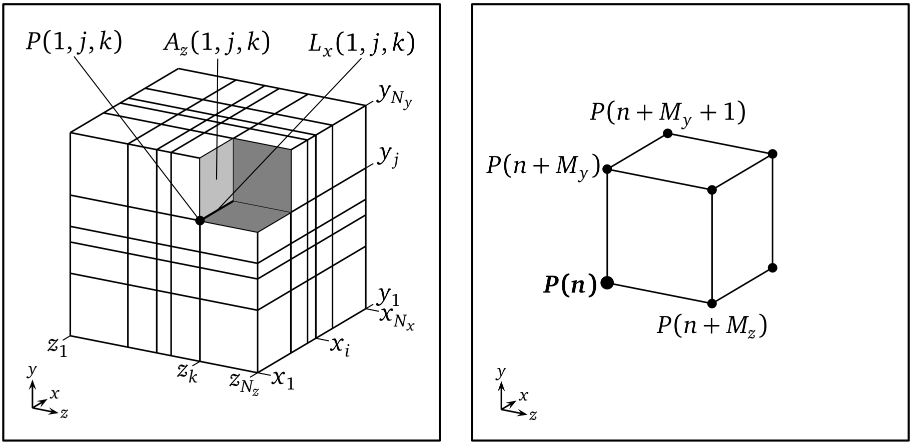

(a) **(b)**

Figure 5.2.: Figure (a) shows an exemplary problem volume which has been subdivided into a finite number of cuboid-shaped volume elements (mesh cells). Each volume element is assigned to a grid point $P(n)$ and can be addressed through its grid coordinates $\{i,j,k\}$. Figure (b) shows the volume element which is assigned to grid point $P(n)=P(1,j,k)$.

$$N_P = N_x N_y N_z \tag{5.3}$$

As an essential property of the FIT discretization scheme, integral quantities are introduced as discrete counterparts for the field intensities and flux densities. Consequently, the line integrals of the electric field intensity and the surface integrals of the magnetic flux density can be expressed as sums of grid voltages and grid fluxes which are allocated on the edges $L_{x,y,z}(n)$ and facets $A_{x,y,z}(n)$ of the grid.

$$\widehat{e}_{x,y,z}(n) = \int\limits_{L_{x,y,z}(n)} \vec{E}\cdot\mathrm{d}\vec{s} \tag{5.4a}$$

$$\widehat{\widehat{b}}_{x,y,z}(n) = \int\limits_{A_{x,y,z}(n)} \vec{B}\cdot\mathrm{d}\vec{A} \tag{5.4b}$$

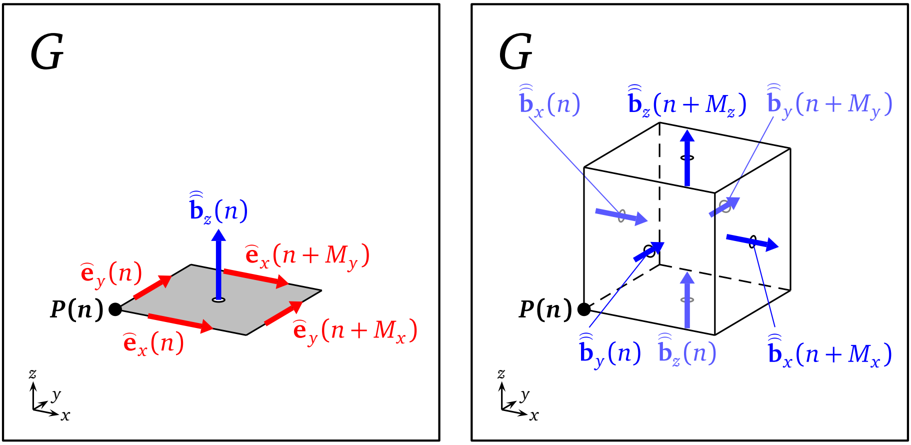

(a) **(b)**

Figure 5.3.: Figure (a) shows a single facet of the primary grid. The grid voltages are allocated on the bounding edges and contribute to the circulation of the electric field. Figure (b) shows a single volume element of the primary grid. The grid fluxes are allocated on the bounding facets and contribute to the surface integral of the magnetic flux density.

The circulation of the electric field for each facet is obtained by summing the grid voltages of the four adjacent edges. By this means Faraday's law can be formulated for a single facet (figure 5.3a):

$$\widehat{e}_x(n)+\widehat{e}_y(n+M_x)-\widehat{e}_x(n+M_y)-\widehat{e}_y(n)=-\frac{d}{dt}\widehat{\widehat{b}}_z(n) \tag{5.5}$$

The surface integral of the magnetic induction for each volume element is obtained by summing the grid fluxes of the adjacent facets. By this means Gauss' law can be formulated for a single volume element (figure 5.3b):

$$-\widehat{\widehat{b}}_x(n)-\widehat{\widehat{b}}_y(n)-\widehat{\widehat{b}}_z(n)+\widehat{\widehat{b}}_x(n+M_x)+\widehat{\widehat{b}}_y(n+M_y)+\widehat{\widehat{b}}_z(n+M_z)=0 \tag{5.6}$$

A second auxiliary grid is introduced, which has essentially the same structure as the *primary* grid but is shifted by one half of a grid step in each coordinate direction (staggered grid). The edges of this *dual* grid intersect orthogonally with the facets of the primary grid and vice versa resulting in a *dual-orthogonal* grid.

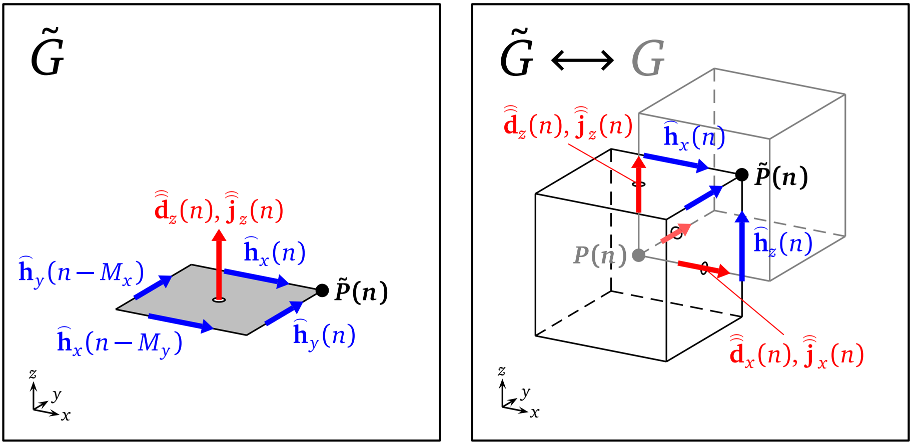

(a) **(b)**

Figure 5.4.: Figure (a) shows a single facet of the dual grid. The magnetic grid voltages are allocated on the bounding dual edges and contribute to the circulation of the magnetic field. Figure (b) shows the duality relations between the two staggered grids. The edges of the grid intersect orthogonally with the facets of the primary grid and vice versa.

The line integrals of the magnetic field intensity, the surface integrals of the electric displacement and the current density can be expressed as magnetic grid voltages, grid fluxes and grid currents which are allocated on the edges $\tilde{L}_{x,y,z}(n)$ and faces $\tilde{A}_{x,y,z}(n)$ of the dual grid:

$$\wideparen{h}_{x,y,z}(n) = \int\limits_{\tilde{L}_{x,y,z}(n)} \vec{H} \cdot \mathrm{d}\vec{s} \tag{5.7a}$$

$$\wideparen{\wideparen{d}}_{x,y,z}(n) = \int\limits_{\tilde{A}_{x,y,z}(n)} \vec{D} \cdot \mathrm{d}\vec{A} \tag{5.7b}$$

$$\wideparen{\wideparen{j}}_{x,y,z}(n) = \int\limits_{\tilde{A}_{x,y,z}(n)} \vec{J} \cdot \mathrm{d}\vec{A} \tag{5.7c}$$

The discretization procedure that has initially been applied to the quantities on the primary grid can be applied in an analogous manner to the quantities on the dual grid. The circulation of the magnetic field for each dual facet is obtained by summing the magnetic grid voltages of the four adjacent edges. By this means Ampere's law can be formulated for a single dual facet (figure 5.4a). The surface integral of the electric displacement is obtained by summing the electric grid fluxes of the adjacent facets. By this means Gauss' law can be formulated for a single dual volume element (figure 5.4b).

The discrete electromagnetic voltages, fluxes, currents and charges can be systematically assembled in vectors of length $3N_P$ allowing for a vector-matrix representation of Maxwell's equations. Through the use of an integral representation, the matrices $\mathbf{C}$, $\widetilde{\mathbf{C}}$ and $\mathbf{S}$, $\widetilde{\mathbf{S}}$ only contain information regarding the topological interconnectedness between voltages and fluxes. The matrix entries take either the value 0 or ±1 which is predetermined by the orientation of the edges and facets in the right-handed coordinate system. The matrices $\mathbf{C}$, $\widetilde{\mathbf{C}}$ and $\mathbf{S}$, $\widetilde{\mathbf{S}}$ can be interpreted as the discrete counterparts of the curl and div operators. Remarkably, the fundamental algebraic properties that are known for the curl and div operators persist for the set of discrete operators [13, 41].

$$\mathbf{C}\widehat{\mathbf{e}} = -\frac{\mathrm{d}}{\mathrm{d}t}\widehat{\widehat{\mathbf{b}}} \tag{5.8a}$$

$$\widetilde{\mathbf{C}}\widehat{\mathbf{h}} = \frac{\mathrm{d}}{\mathrm{d}t}\widehat{\widehat{\mathbf{b}}} + \widehat{\widehat{\mathbf{j}}} \tag{5.8b}$$

$$\widetilde{\mathbf{S}}\widehat{\widehat{\mathbf{d}}} = \mathbf{q} \tag{5.8c}$$

$$\mathbf{S}\widehat{\widehat{\mathbf{b}}} = 0 \tag{5.8d}$$

The connection between primary and dual grid is established through the discretized representation of the constitutional equations. The mutual position of primary and dual grid indicates that a suitable averaging procedure is required for the material parameters ε, μ and κ. A detailed explanation about the assembly of the material matrices $\mathbf{M}_\varepsilon$ and $\mathbf{M}_\mu$ and the implementation of boundary conditions can be found in [5, 27, 47, 54] and in the up-following publications by Weiland et al.

5.3 Time domain analysis

Until this point only the discretization of the problem volume has been adressed and discrete counterparts have been found for the 3D differential operators.

$$\frac{\mathrm{d}}{\mathrm{d}t}\widehat{\mathbf{h}}(t) = -\mathbf{M}_{\mu^{-1}}\mathbf{C}\widehat{\mathbf{e}}(t) \tag{5.9a}$$

$$\frac{\mathrm{d}}{\mathrm{d}t}\widehat{\mathbf{h}}(t) = \mathbf{M}_{\varepsilon}^{-1}\left(\widetilde{\mathbf{C}}\widehat{\mathbf{h}}(t) - \widehat{\widehat{\mathbf{j}}}(t)\right) \tag{5.9b}$$

For time-varying fields also a discretization of the time axis must take place. The desired time range is subdivided in equidistant intervals by defining sampling points $t_m := t_0 + m\Delta t,\ m \in \mathbb{N}^{\geq 0}$.

$$T := \left\{ t_m \in \mathbb{R}^{\geq 0} \,|\, t_0 \leq t_m \leq t_{max}, t_m := t_{m-1} + \Delta t \right\} \tag{5.10}$$

The semi-discrete formulations of Faraday's and Ampere's law (equations 5.9a and 5.9b) indicate, that only the time derivative of either $\widehat{\mathbf{e}}$ or $\widehat{\mathbf{h}}$ is required at the same time. The time derivatives are approximated by means of central differences, whereupon the derivative at $t_{m+1/2}$ is given by the neighbouring sampling points at t_m and t_{m+1}.

$$\frac{\mathrm{d}}{\mathrm{d}t}\widehat{\mathbf{h}}^{(m+1/2)} \approx \frac{\widehat{\mathbf{h}}^{(m+1)} - \widehat{\mathbf{h}}^{(m)}}{\Delta t} \tag{5.11a}$$

$$\frac{\mathrm{d}}{\mathrm{d}t}\widehat{\mathbf{e}}^{(m+1)} \approx \frac{\widehat{\mathbf{e}}^{(m+3/2)} - \widehat{\mathbf{e}}^{(m+1/2)}}{\Delta t} \tag{5.11b}$$

By introducing half steps the update equations for $\widehat{\mathbf{e}}$ and $\widehat{\mathbf{h}}$ can be written in explicit notation and the computationally efficient *leapfrog* time integration scheme is obtained [57]:

$$\widehat{\mathbf{h}}^{(m+1)} := \widehat{\mathbf{h}}^{(m)} - \Delta t\mathbf{M}_{\mu^{-1}}\mathbf{C}\widehat{\mathbf{e}}^{(m+1/2)} \tag{5.12a}$$

$$\widehat{\mathbf{e}}^{(m+3/2)} := \widehat{\mathbf{e}}^{(m+1/2)} + \Delta t\mathbf{M}_{\varepsilon}^{-1}\left(\widetilde{\mathbf{C}}\widehat{\mathbf{h}}^{(m+1)} - \widehat{\widehat{\mathbf{j}}}^{(m+1)}\right) \tag{5.12b}$$

Thus, this type of algorithm belongs to the supergroup of Finite Difference Time Domain (FDTD) algorithms.

A necessary condition for the stability of the algorithm is given through the generalized Courant-Friedrichs-Levy (CFL) condition [55]:

$$\Delta t \leq \min_i \left\{ \frac{\sqrt{\varepsilon_i \mu_i}}{\sqrt{\frac{1}{\Delta x_i^2} + \frac{1}{\Delta y_i^2} + \frac{1}{\Delta z_i^2}}} \right\} \tag{5.13}$$

This criterion empirically determines an upper bound for the time step length depending on the spatial discretization for a problem volume with inhomogenous material properties [55].

Single charged particles have dimensions in the range of 10^{-15}m which can not be resolved by any grid. Thus they are represented by *macro particles* which are a much like a rigid bunch of particles while its dimensions are in the range of the grid spacing. The bunch profile is characterized by the transverse and longitudinal charge densities $q_\perp$ and $q_{||}$ which must be carried over to the discretized problem. In the field of numerical simulation only signals which have a finite duration and finite slew rate can be realized. The more a signal approaches the Dirac delta function the more bandwidth is occupied by its spectrum. This, in turn, reduces the time step length and therefore requires a finer discretization of the problem volume. The use of Gaussian signals is founded both on its mathematical properties and the fact that a Gaussian profile is an adequate assumption for many practical applications. However, in the present case the Gaussian profile is not related to an actual beam profile. For reasons of simplicity a particle beam with point-like cross-section is assumed. The longitudinal profile is given as a single Gaussian bunch. Thus, the charge distribution is fully described by the total bunch charge Q_{bunch} and the standard deviation σ_z of the Gaussian distribution which is related to the Root Mean Square (RMS) bunch length ${L_{\text{bunch}}}^2$.

$$q_V(s) = Q_{\text{bunch}}\, q_{||}(s) = Q_{\text{bunch}} \frac{1}{\sqrt{2\pi\sigma_z^2}} e^{-\frac{s^2}{2\sigma_z^2}} \tag{5.14}$$

---

[2] Various application-dependent definitions can be found in literature for the term bunch length: The RMS bunch length is defined as the total length for a rectangular distribution having the same square measure as the actual bunch profile. Differing definitions of the term bunch length will be explained where necessary.

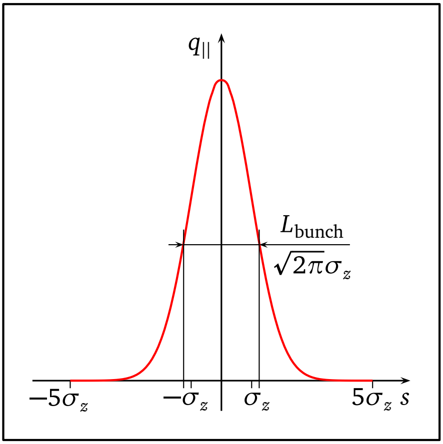

Figure 5.5.: Longitudinal charge distribution described by a Gaussian profile. The area bounded by the Gaussian curve and the abscissa equals the normalized bunch charge. For practical application the distribution is truncated where it falls below $1/1000$ of its peak value.

The RMS bunch length for a Gaussian bunch is defined as:

$$L_\text{bunch} = \sqrt{2\pi}\sigma_z \approx 2.5\sigma_z \quad \rightarrow \quad \int\limits_{-\infty}^{+\infty} q_{||}(s)\,\mathrm{d}s = 1 \tag{5.15}$$

Since the charge distribution must be of finite length, the longitudinal profile is truncated where the Gaussian function falls below $1/1000$ of its peak value. The bunch spectrum is obtained through Fourier transform. The standard deviation σ_z is chosen such that the frequency range of interest is contained in the spectrum of the truncated signal.

With each time step the charge distribution is passed through the grid following a uniform motion on a predefined path. The calculation of the EM field is followed by numerical integration to yield the wake potential $W_{||}$ which is recorded for the desired length L_wake. The wake potential accounts for the predefined bunch profile therefore the wake function must be calculated by means of deconvolution. Alternatively, the coupling impedance can be calculated by normalizing the Fourier transform of the wake potential with the bunch spectrum.

$$\left.\begin{array}{l} W_{||}(s) = G_{||}(s) * q_{||}(s) \\ \underline{Z}_{||}(\omega) = \mathfrak{F}\left\{G_{||}(s)\right\} \end{array}\right\} \Rightarrow \mathfrak{F}\left\{W_{||}(s)\right\} = \mathfrak{F}\left\{G_{||}(s) * q_{||}(s)\right\} = \mathfrak{F}\left\{G_{||}(s)\right\}\mathfrak{F}\left\{q_{||}(s)\right\} \tag{5.16}$$

The longitudinal coupling impedance is obtained as:

$$\underline{Z}_{||}(\omega) = \frac{\mathfrak{F}\left\{W_{||}(s)\right\}}{\mathfrak{F}\left\{q_{||}(s)\right\}} \tag{5.17}$$

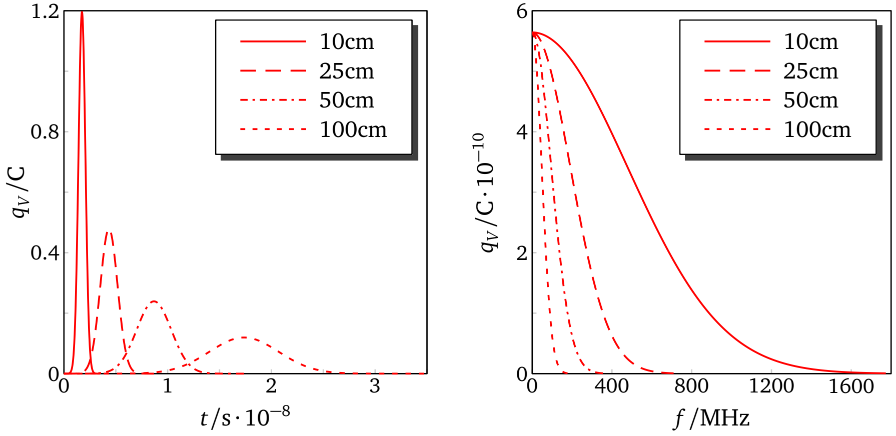

(a) **(b)**

Figure 5.6.: bunch profiles (a) and bunch spectra (b) for GAUSSIAN bunches with different values for the standard deviation σ_z. The position axis s is connected with the time axis t through the bunch velocity v as $s = vt$.
A shift of the bunch spectrum towards higher frequencies requires a finer discretization in order to resolve the shortest wavelength with at least several meshlines.

The wake potential is recorded for an interval of finite duration $T_\mathrm{w} = L_\mathrm{w}/v$. Consequently, the wake potential must be weigthed with a window function which for the coupling impedance results in an additional convolution with the FOURIER transform of the window function. The use of a rectangular window function Π leads to the cardinal sine function as counterpart for convolution in frequency domain:

$$\mathfrak{F}\left\{\Pi_{T_\mathrm{w}}(t)\right\} = \int\limits_{-\infty}^{+\infty} \Pi_{T_\mathrm{w}}(t)\,dt = \int\limits_{-T_\mathrm{w}/2}^{+T_\mathrm{w}/2} 1e^{j\omega t}\,\mathrm{d}t = T_\mathrm{w}\,\mathrm{sinc}\left(\omega\frac{T_\mathrm{w}}{2}\right) \tag{5.18}$$

The total area enclosed by the sinc-function is given by[3]:

---

[3] $\int\limits_{-\infty}^{+\infty} \mathrm{sinc}(\xi)\,\mathrm{d}\xi = \pi$, [AS72]

$$\int_{-\infty}^{+\infty} \mathfrak{F}\left\{\Pi_{T_\mathrm{w}(t)}\right\} \mathrm{d}\omega = T_\mathrm{w} \int_{-\infty}^{+\infty} \mathrm{sinc}\left(\omega \frac{T_\mathrm{w}}{2}\right) \mathrm{d}\omega = 2\pi \tag{5.19}$$

In the limit of $T_\mathrm{w} \rightarrow \infty$ the sinc-function approaches the δ-function. For sufficiently large T_w the following estimate may be used:

$$\lim_{T_\mathrm{w}\rightarrow\infty} \mathfrak{F}\left\{\Pi_{T_\mathrm{w}}(t)\right\} \rightarrow 2\pi\delta(\omega) \Rightarrow \mathfrak{F}\left\{\Pi_{T_\mathrm{w}}(t)\right\} \rightarrow 2\pi\delta(\omega) + \mathcal{O}\left(\frac{1}{T_\mathrm{w}}\right) \tag{5.20}$$

The Dirac delta function is followed by a remainder espression which indicates the error caused by truncation. The influence on the coupling impedance can be estimated according:

$$W_{||,\Pi}(s) = \left(G_{||}(s) q_{||}(s)\right) \Pi_{T_\mathrm{w}}(s) \tag{5.21a}$$

$$Z_{||,\Pi}(\omega) = \frac{\mathfrak{F}\left\{W_{||,\Pi}(s)\right\}}{\mathfrak{F}\left\{q_{||}(s)\right\}} = \frac{\left(\mathfrak{F}\left\{G_{||}(s)\right\}\mathfrak{F}\left\{q_{||}(s)\right\}\right) * \mathfrak{F}\left\{\Pi_{T_\mathrm{w}}(s)\right\}}{\mathfrak{F}\left\{q_{||}(s)\right\}} \tag{5.21b}$$

$$= \underbrace{\frac{\left(\mathfrak{F}\left\{G_{||}(s)\right\}\mathfrak{F}\left\{q_{||}(s)\right\}\right) * \delta(\omega)}{\mathfrak{F}\left\{q_{||}(s)\right\}}} + \frac{\mathcal{O}\left(\frac{1}{T_\mathrm{w}}\right)}{\mathfrak{F}\left\{q_{||}(s)\right\}} \tag{5.21c}$$

$$= \underline{Z}_{||}(\omega) + \mathcal{O}\left(\frac{1}{T_\mathrm{w}}\right) \tag{5.21d}$$

This effect is known as *spectral leakage* and alters the original spectrum. The spectral components of the original signal leak into neighbouring components causing a blurring of the original spectrum. This must be kept in mind during the interpretation of the results. If certain parts of the spectrum are more relevant than others, the effect may be influenced by choosing a different type of window function. For the case of lossy and/or open structures the stored EM energy will decay with time due to dissipation or propagation of the EM field. Thus the wake potentials must approach zero and the influence of the window function is reduced by choosing a sufficiently large time interval. The recorded temporal progression of the stored energy serves as an indicator whether the calculation has been truncated too early. The beam entry and exit planes must allow for either unimpeded propagation or natural attenuation of the wakefields. Simple boundary conditions such as a PEC ($\vec{E} \times \vec{n} = 0$) or a Perfect Magnetic Conductor (PMC) ($\vec{H} \times \vec{n} = 0$) can not be used here, therefore an open boundary condition based on a Perfectly Matched Layer

(PML) formulation is used.

Finally, the most important simulation parameters can be summarized as follows (preferred values are listed in brackets):

- Grid step widths Δx, Δy, Δz
- Number of volume elements N_V
- Bunch charge Q_{bunch} (10^{-9} C)
- Standard deviation σ_z of the GAUSSIAN profile (15 cm)
- Bunch displacements d_x and d_y from reference orbit
- Relative bunch velocity β (1.0)
- Wake length L_{wake} (100 m)
- Time step reduction factor α_t (0.85)[4]

All TD simulations have been carried out with CST PARTICLE STUDIO® [43] which follows the procedure above. The post-processing of the wakefield data is already included. In the scope of this work the influence of ferrite material on the wakefield is of special interest. Time domain modeling of non-linear hysteresis usually requires some type of memory function where the magnetization history is stored. These methods are still subject to research and more costly. By introducing a complex-valued permeability $\underline{\mu}_{\mathrm{r}} = \mu_{\mathrm{r}}' - j\mu_{\mathrm{r}}''$ it is possible to approximate the hysteretic behaviour by inscribing a sheared ellipse in the hysteresis loop. The TD module of CST PARTICLE STUDIO® allows to approximate this frequency-dependent behaviour with a second order dispersion model [22, 43]. The coefficients are determined in an automated fitting process which is based on the frequency characteristics of μ_{r}' and μ_{r}''. The raw data for different materials is pictured in appendix H.1 while raw data and fitted data are plotted for comparison in figure 5.7.

---

[4] A time step reduction factor less than 1.0 reduces the time step width below the upper bound provided through the CFL condition as a precautional measure against numerical instability.

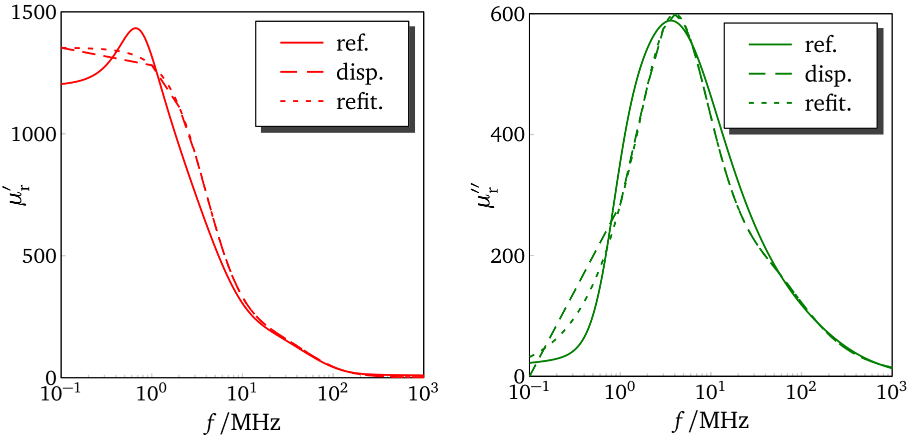

(a) **(b)**

Figure 5.7.: Comparison of the relative permeability for 8C11 ferrite obtained from the datasheet (reference) and the dispersion model (disp.). The third curves have been refitted to the dispersion model to compensate for the small number of data-points in the region 0.1 to 1 MHz and to obtain a more smooth characteristic.
There is an obvious difference compared to the reference data, which affects the results for the coupling impedance. For a coherent comparison of time domain simulation results and analytical results the permeability data obtained from the dispersion model must be used for the analytical calculation as well.

5.3.1 Rotational symmetry

The hollow cylinder characterized by the radii ϱ_1 and ϱ_2 has been treated analytically in the previous chapter. The previous results are now compared with the time domain simulation results obtained with CST Particle Studio® [43]. The rotational symmetry with respect to the z-axis allows to insert magnetic mirror planes ($H_\mathrm{tan} = 0$) at $y = 0$ and $x = 0$ which reduce the effective problem size to one quarter of the original problem size. The background material is chosen as PEC where all fields must vanish.
The numerical results show very good agreement with the analytical results (figure 5.9) and emphasize the suitability of the TD approach. The maximum deviation with respect to the analytical result occurs around 70 MHz and reads less than 6%.

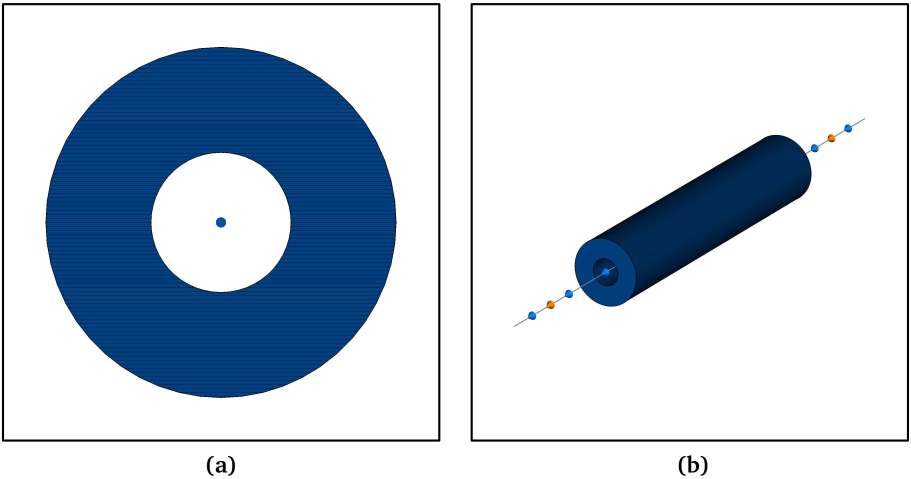
(a) (b)

Figure 5.8.: Computational model shown in 2D (a) and 3D (b). The ultra-relativistic particle beam is represented as central line with arrows pointing in the direction of the positive z-axis. The inner vacuum region and the perfectly-conducting background region are hidden.

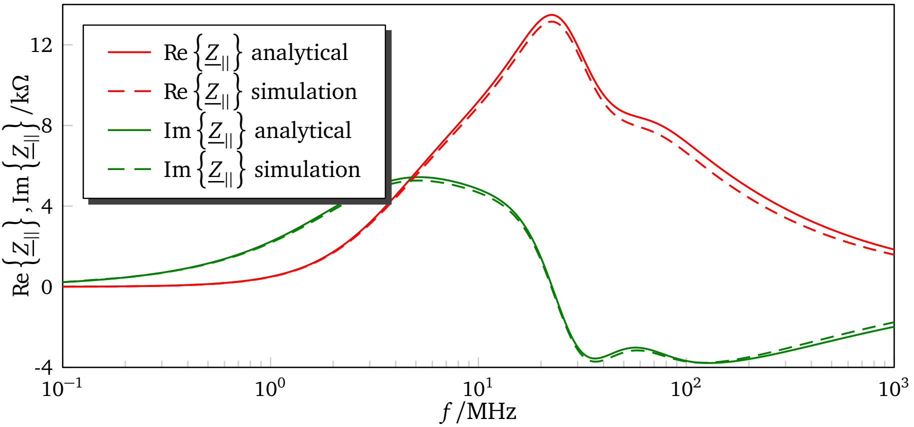

Figure 5.9.: Comparison of analytical and time domain simulation results for the rotationally symmetric problem of unit length. The dimensions are $\varrho_1 = 2$ cm and $\varrho_1 = 8$ cm which correspond to the minimum aperture of an actual beamline devices.

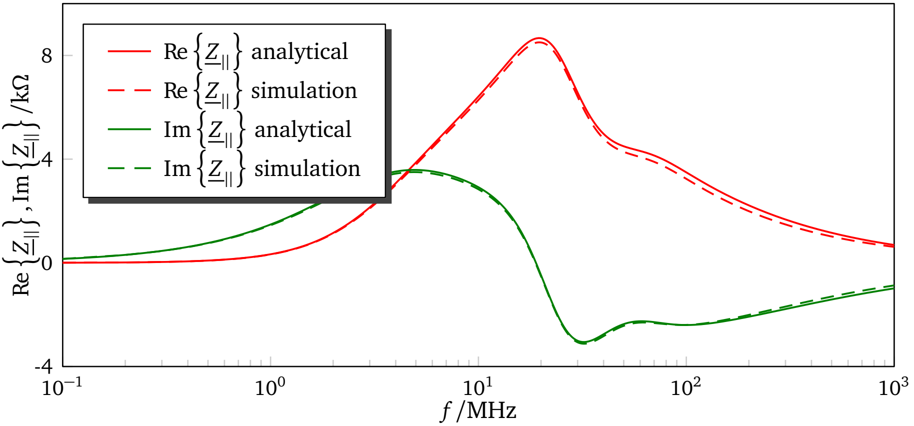

Figure 5.10.: Comparison of analytical and time domain simulation results for the rotationally symmetric problem. This time the dimensions are $\varrho_1 = 4$ cm and $\varrho_2 = 10$ cm.

5.3.2 Planar symmetry

The parallel plates characterized by the lengths x_1, y_1 and y_2 have been treated analytically in the previous chapter. By analogy with the rotational-symmetric problem the analytical results are now compared with the time domain simulation results obtained with CST Particle Studio®. The planar symmetry allows to insert magnetic mirror planes ($H_{\text{tan}} = 0$) at $y = 0$ and $x = 0$ which reduce the effective problem size to one quarter of the original problem size for the case of the centered particle beam. The background material is chosen as PEC where all fields must vanish.

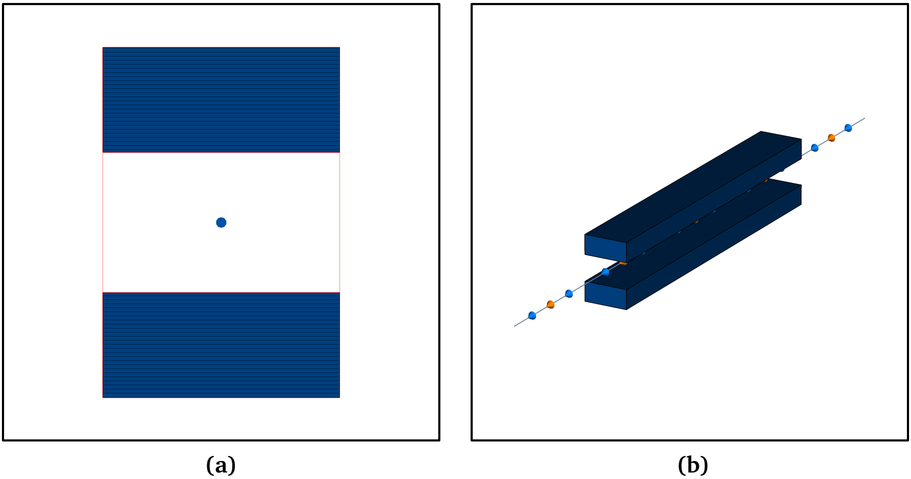
(a)

(b)

Figure 5.11.: Computational model for planar symmetry shown in 2D (a) and 3D (b). The ultra-relativistic particle beam is represented as central line with arrows pointing in the direction of the positive z-axis. The inner vacuum region and the perfectly-conducting background region are hidden.

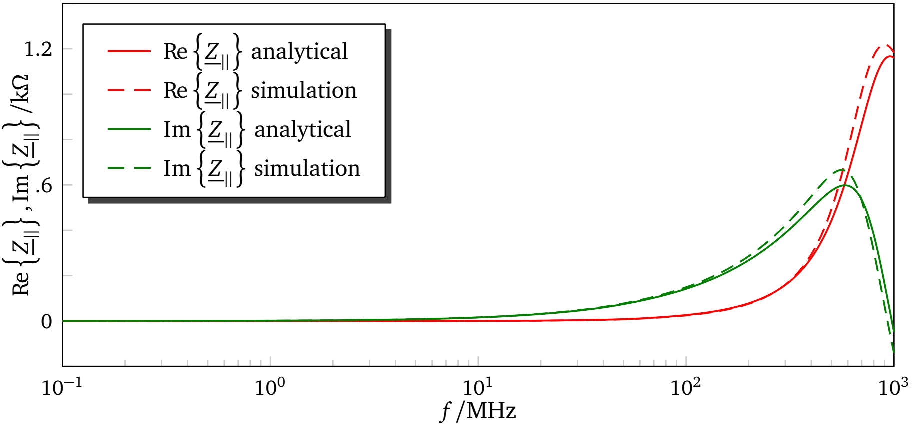

Figure 5.12.: Comparison of analytical and time domain simulation results for the planar symmetric problem of unit length. The dimensions are $x_1 = 6.75$ cm and $y_1 = 4$ cm which corresponds to the aperture of an actual beamline device.

5.4 Frequency domain analysis

Phasor notation has previously been introduced for the continuous space, more precisely the time-harmonic field intensities and flux densities. This concept can be expanded to quantities in discrete space. Hence, the vector entries in FIT notation represent complex voltage amplitudes and flux amplitudes while the material matrices may take complex-valued entries. The derivative with respect to time is replaced by the factor $j\omega$. Thus, the FD wave equation for non-vanishing source terms using FIT notation reads:

$$\underbrace{\left(\widetilde{\mathbf{C}}\mathbf{M}_{\mu}^{-1}\mathbf{C}-\omega^{2}\mathbf{M}_{\varepsilon}\right)}_{\mathfrak{L}}\widehat{\mathbf{e}} = -j\omega\widehat{\widehat{\mathbf{j}}}_{\beta} \tag{5.22}$$

At the same time discretization of the frequency axis is accomplished by solving the complex-valued linear system separately for selected frequencies. $\mathbf{C}$, $\widetilde{\mathbf{C}}$, $\mathbf{M}_{\varepsilon}$ and $\mathbf{M}_{\mu}^{-1}$ are $3N_P \times 3N_P$ square matrices while the material matrices $\mathbf{M}_{\varepsilon}$ and $\mathbf{M}_{\mu}^{-1}$ are diagonally symmetrical. Complex-valued material matrices result in a complex-valued linear equation system, where the number of the degrees of freedom can easily reach several hundreds of thousands for practical applications. The efforts of solving such kind of linear system ususally rely on iterative methods (KRYLOV subspace methods, [Saa03]). Alternative methods have been proposed to improve the convergence behaviour for ill-conditioned systems [16, 17].

Special attention is paid to the treatment of the domain boundaries that coincide with the particle entry and exit planes. All beamline devices are usually located in some kind of vacuum vessel. The transverse dimensions of the vessel reduce abruptly at the beam entry and exit ports to match the diameter of the beampipe which connects neighbouring sections (step transition). The EM field in the beampipe sections follows the known longitudinal dependency as long as the influence of the perturbing beamline device has vanished:

$$\left\{\begin{array}{c}\underline{\vec{E}}\\ \underline{\vec{H}}\end{array}\right\}_{beampipe} \propto e^{-j\frac{\omega}{v}z} \tag{5.23}$$

With this knowledge the EM problem inside the beampipe reduces to a transverse 2D problem. The 2D solution serves as boundary condition for the 3D problem inside the vessel [17].

The simulation parameters can be summarized as follows:

- Grid step widths Δx, Δy, Δz.
- Number of volume elements N_V
- Bunch displacements d_x and d_y.
- Relative bunch velocity β.
- Frequency f_0.

5.4.1 Rotational symmetry

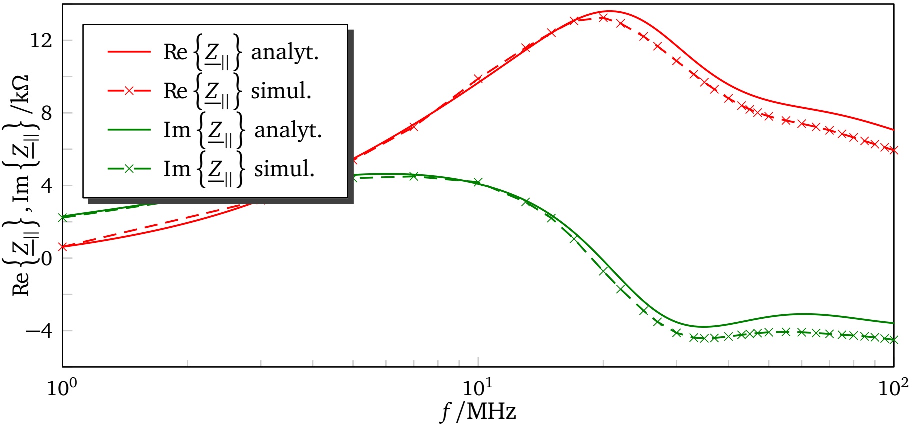

Figure 5.13.: Comparison of analytical and frequency domain simulation results for the rotationally symmetric problem of unit length. The dimensions are $\varrho_1 = 2$ cm and $\varrho_1 = 8$ cm which correspond to the minimum aperture of an actual beamline device.
Markers indicate frequencies for which the problem was solved. The increasing deviation at frequencies around 100 MHz is owed to both differences in extrapolation of material data and coarse meshing.

5.5 Conclusive remarks

Both simulation approaches are in good agreement with the analytically predicted results. The deviations that have been found originate mostly from the different realization of lossy materials. The TD approach requires long simulation intervals to reproduce the low frequency regime. For frequencies $f < f_{min}$ an integration interval $T > 1/f_{min}$ must be available. The simulation time is further increased due to the slow decay of EM energy. The spacing of the frequency points is a consequence from the number of sampling points used for the Discrete-Time FOURIER Transform (DTFT).

The frequency domain approach allows to explore arbitrarily low frequencies while requiring a single simulation for each point on the frequency axis.

6 Application: Coupling Impedance analysis for the SIS100 kicker system

Several applications require an abrupt change of the particle trajectory : After acceleration in a preceeding synchrotron (SIS18) or linear accelerator, the particle beam must be injected into the main synchrotron (SIS100). After completion of the final acceleration cycle the particle beam must be extracted and supplied for experimental use. To dispose the beam, an emergency extraction to a designated beam dump can be initiated.

Obviously, an immediate shut-down of the dipole magnets would cause a tangential ejection of all particles regardless of their current position causing unforeseeable damage and radioactivation. A suitable transverse force field must be applied at the right time and place to permit a controlled extraction into a designated transfer channel. In the case of a fast extraction procedure this transverse kick is typically accomplished through a magnetic field[1]*. The kick direction is given by the orientation of* $\vec{v} \times \vec{B}$*. Depending on their individual purpose, these devices are called injection kicker, extraction kicker, transfer kicker or emergency kicker (magnet).*

6.1 The SIS100 kicker system

To accomplish a certain amount of transverse deflection it may be necessary to arrange multiple modules in series such that they are subsequently passed by the particle beam. Each module consists of a specialized window frame dipole magnet which must have low rise time ($< 1\mu$s) in order to provide the desired deflection instantly. The coil current must remain constant during the extraction phase in order to provide the same deflection for all particles. In the following the SIS100 extraction / emergency kicker is studied representatively for all kicker magnets based on a similar design.

---

[1] Electrostatic septa which are used for slow extraction are not discussed here.

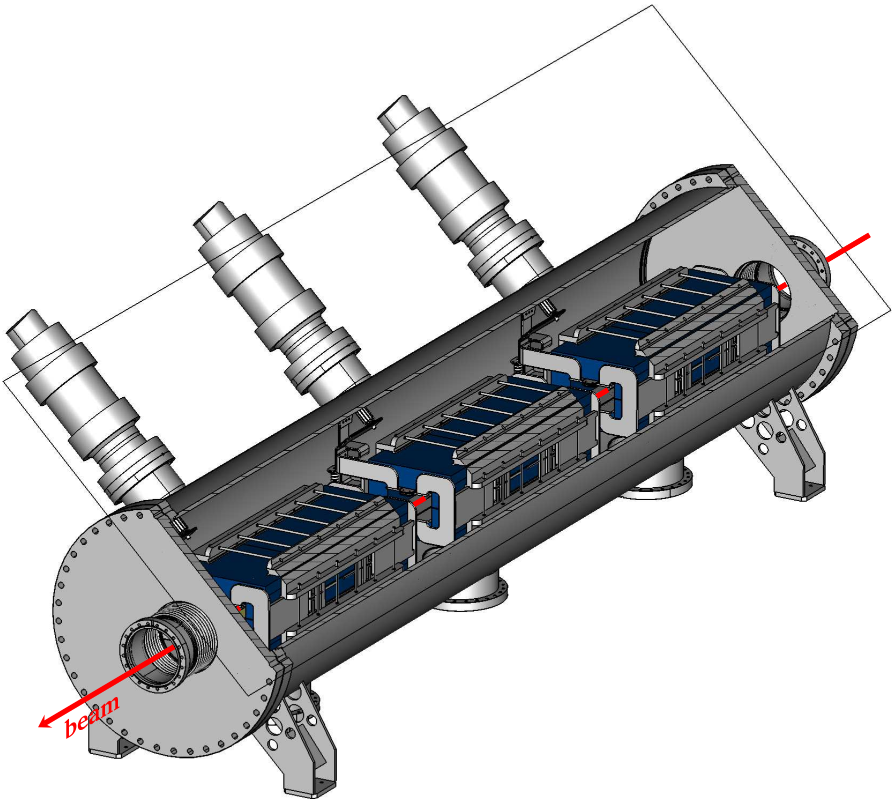

Figure 6.1.: The figure shows a perspective view of the SIS100 fast extraction kicker system. Three single units are stored in one vacuum vessel which has been opened for illustration. The particle beam enters through a beam port on the cover plate and exits on the opposite side. Mechanical support structures have been omitted partly for better visibility of the actual magnet devices. Each magnet coil is connected to a designated power supply through a coaxial high voltage feedthrough. The total dimensions are about 3m in length and 0.75m in diameter. Computer Aided Design (CAD) graphics by courtesy of: Ulrich Kopf, GSI GmbH.

6.1.1 Bipolar window frame kicker magnet

Each unit consists of a *coil* which is enclosed by a ferrite *yoke*. The yoke is made up of several blocks of high permeable ferrite which are secured by a cage construction to hold everything in place. The kicker magnet follows a *current-dominated* design thus the ferrite mainly serves to minimize stray flux and to flatten the magnetic field pattern. The force on each particle is proportional to the magnitude of the magnetic field which in turn is proportional to the Magnetomotive Force (MMF) given by $\Theta_{\mathrm{mag}} = N_{\mathrm{coil}} I_{\mathrm{coil}}$. The kick direction can be changed to the opposite direction by reversing the polarity of the current (capability for bipolar operation). The coil geometry can be best described as two opposite planar coils that are connected in series, each having a single turn[2]. Both coils are aligned in parallel with the y-z- plane, producing predominantly an x- component for the magnetic field. Consequently the particles are deflected in the y- direction.

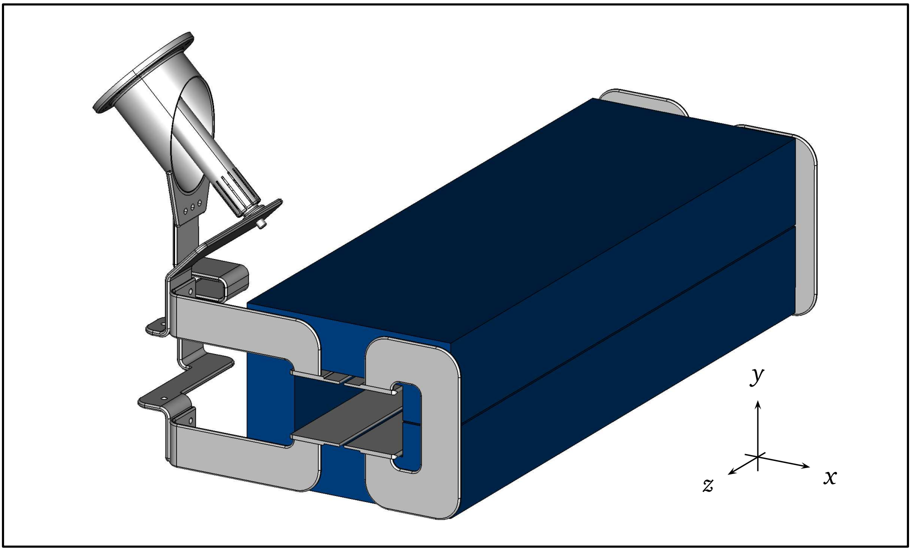

Figure 6.2.: Perspective view of a single magnet unit including the ferrite block, coil and the high-voltage coaxial feedthrough. The aperture measures 135mm by 80mm.

---

[2] This arrangement is not to be confused with the HELMHOLTZ coil pair, since the uniformity of the magnetic field is achieved through the boundary condition $H_{\mathrm{tan}} \approx 0$ on the surface of the ferrite while the term HELMHOLTZ coil pair exclusively refers to air coils.

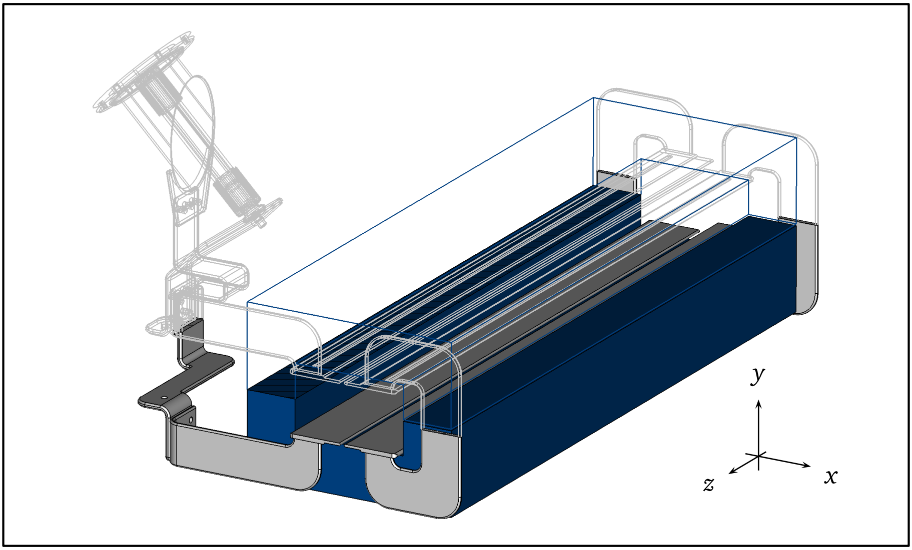

(a)

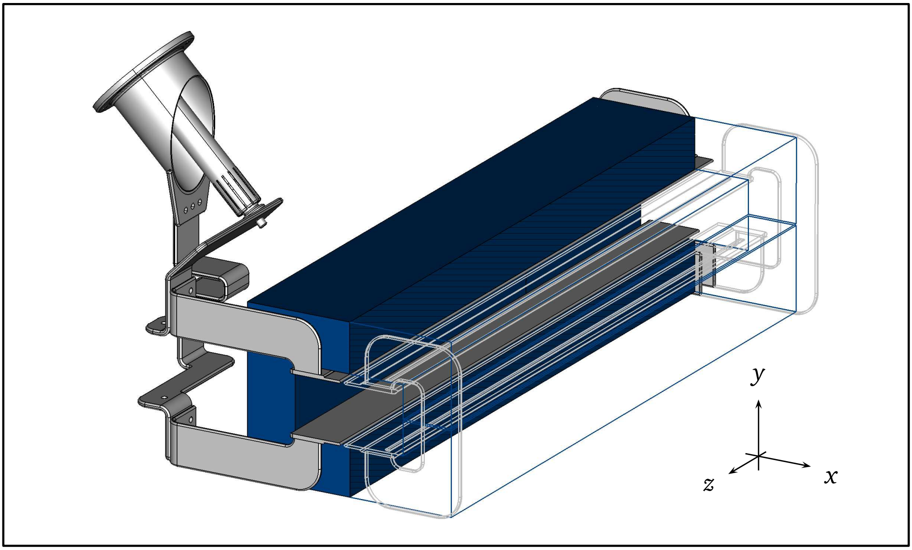

(b)

Figure 6.3.: Longitudinal sections visualizing the coil geometry in the x-z-plane (a) and the y-z-plane (b). The cut-away parts are drawn as wireframe.

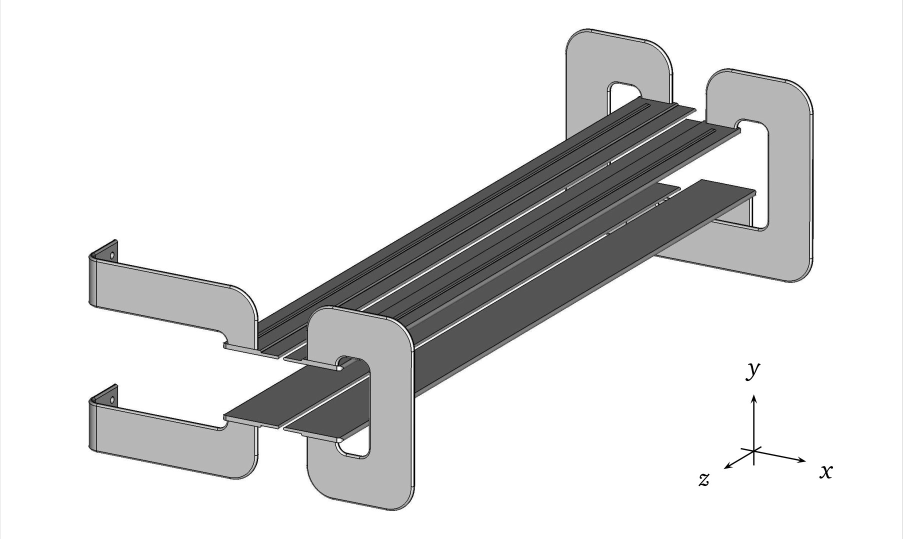

Figure 6.4.: Coil geometry of a single SIS100 kicker magnet.

Due to the orientation of the coil, predominantly the transverse x-component of the magnetic field will couple to the kicker circuit and induce a voltage in the coil. In turn, a transverse magnetic field is produced by the dipole moment of the beam current. A quantitative description of the coupling between particle beam and kicker circuit is given in the next sections.

6.1.2 Power supply

In order to keep the coil inductance in the range of a few mH, the coil of a fast kicker magnet has a few turns only. This results in increased demands for current to yield the required MMF (several kA-turns). For the extraction phase the current must remain constantly at maximum level. This requires a charge reservoir that discharges with constant current, which will be called Pulse Forming Network (PFN) in the following. This is either accomplished by a delay line that has a suitable capacitance and inductance per unit length or by cascading discrete circuits of capacitors and inductors [56]. The PFN is charged by an external high-voltage source and finally discharged through the primary winding of a pulse transformer which provides galvanic isolation. Bipolar operation is achieved by using a center-tapped primary winding for the pulse transformer. The discharge current is supplied to only one half at a time for each kick direction which is accomplished by thyratron switches. The secondary winding of the pulse transformer is connected to the kicker coil which forms the bridge element of a *bridged-T* impedance matching network [33]. The network is terminated with a load resistor in order to absorb the pulse power [6].

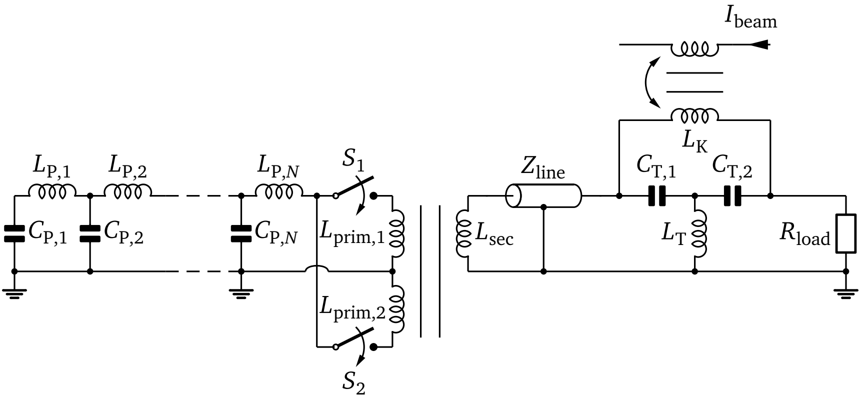

Figure 6.5.: The schematic shows the complete kicker circuit. From left to right: pulse forming network (C_{P} and L_{P}) thyratron switches (S_1 and S_2), isolation transformer (L_{prim} and L_{sec}) , cable (Z_{line}), bridged-T impedance matching network (C_{T}, L_{T} and L_{K}) , and the load resistor (R_{load}). Inductive coupling between particle beam and kicker magnet is illustrated by a second transformer.The cable is modeled as a lossy transmission line.

If the kicker magnet is not in operation, the PFN remains disconnected. The kicker acts as a passive component and only the secondary winding of the transformer remains part of the kicker circuit. Inductive coupling between the coil and the particle beam is assumed, which can be understood as a transformer circuit, where the primary flux is linked to the dipole moment of the beam current. Therefore the kicker circuit contributes to the transverse coupling impedance. The generator impedance Z_{G} must be obtained through circuit analysis or measurement [7, 38, 56]. All relevant circuit parameters are listed in table 6.1.

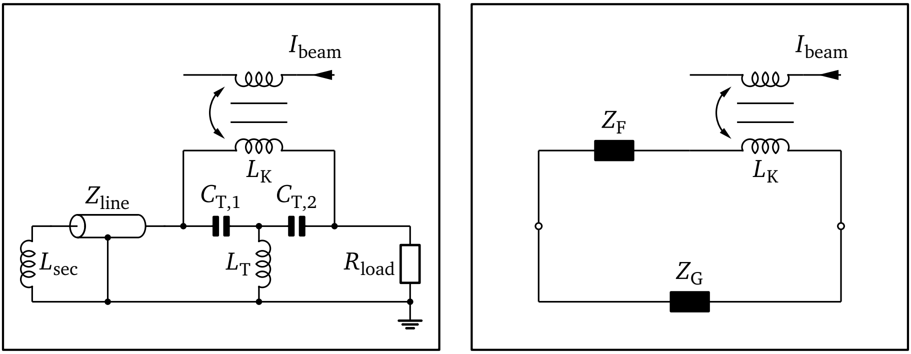

(a) **(b)**

Figure 6.6.: The schematics show the effective circuit, when the kicker magnet is not energized: (a) shows the relevant components, which can be merged into a combined lumped element Z_G according (b). The presence of the ferrite material has been taken into account through the addition of the serial circuit element Z_F.

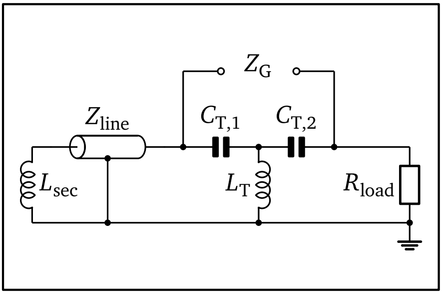

Figure 6.7.: The schematic shows the remaining components of the kicker circuit.

Parameter		Value	Unit
Sec. inductance	L_{sec}	4	μH
Capacitance	C_T	49.9	nF
Inductance	L_T	825	nH
Load resistance	R_{load}	5.7	Ω
Transmiss. line	R'_{line}	2.1	mΩ/m
	L'_{line}	35	nH/m
	C'_{line}	1.08	nF/m

Table 6.1.: The values for the relevant circuit parameters are listed. The transmission line has a length of 100m, furthermore the parasitic conductance is neglected ($G'_{\text{line}} = 0$).

The transmission line consists of three identical coaxial cables (CPP20, [44]) that are connected in parallel resulting in the line parameters R'_{line}, L'_{line} and C'_{line}. Strictly speaking these parameters themselves are frequency dependent due to the *skin effect*, *proximity effect* and *dielectric dispersion*. For reasons of simplicity an operating point of $f = 300\text{kHz}$ is assumed for the purpose of this application.

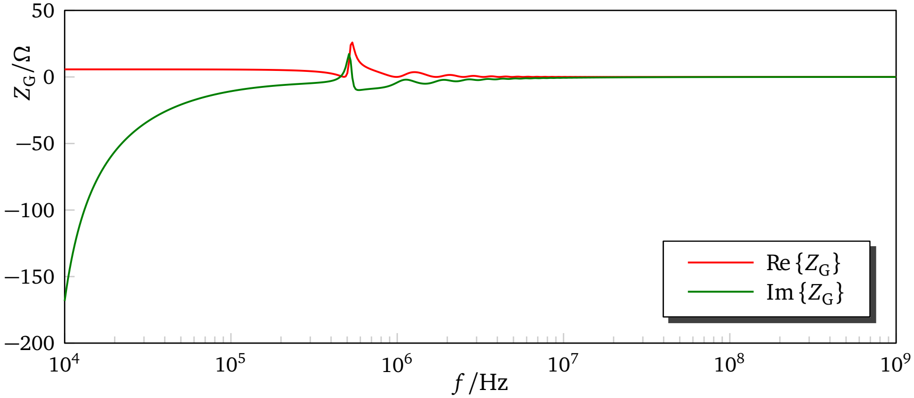

Figure 6.8.: Real and imaginary part of the generator impedance Z_G. The influence of the circuit is mostly present in the frequency range below 10MHz.

The total generator impedance as it is perceived at the terminal is shown in figure 6.8. The impedance has been determined using conventional circuit analysis and confirmed with Micro Cap, a Simulation Program with Integrated Circuit Emphasis (SPICE) [46]. A more detailed analysis of the circuit is presented in appendix F.

6.2 Mutual coupling

In the first instance, the current density of a displaced particle beam is given by the moments of first and second order, the monopolar and dipolar source field respectively, outlined in figure 6.9. The flux produced by the monopolar source field forms concentric loops inside the yoke which is the primary source of dissipative losses in the ferrite material. This flux does not couple to the coil winding. The differential flux produced by the dipolar source field also contributes to dissipative losses but most notably couples to the coil winding and therefore establishes a connection to the external *lumped element network*. The strength of the coupling depends on the relative orientation of the dipolar source field and the coil. Possible coil arrangements are shown in figure 6.10. According the coil orientation shown in figure 6.10c mutual coupling is maximized for the x- component of the magnetic source field. In the following an approximate relation for the quantitative description of mutual coupling between the coil and the particle beam is presented following the formalism described in [19, 32].

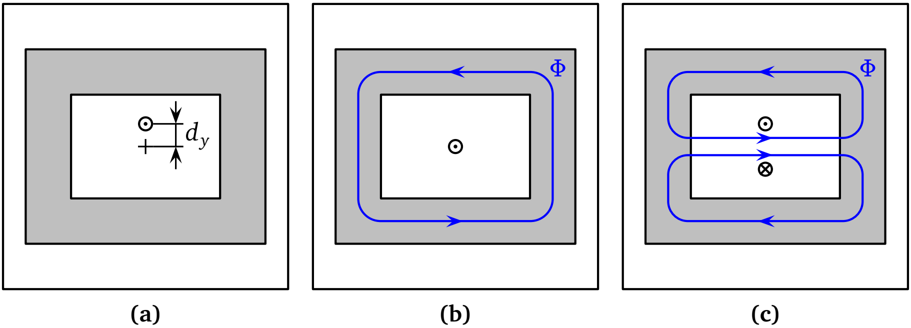

(a) (b) (c)

Figure 6.9.: Cross-sectional view on a window frame kicker magnet. The vertically displaced particle beam in figure (a) produces monopolar and dipolar source fields. The corresponding magnetic flux lines are illustrated in figure (b) and (c), respectively.

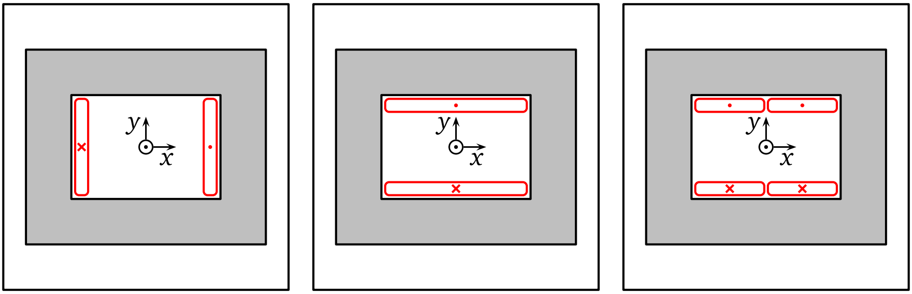

(a) (b) (c)

Figure 6.10.: Cross-sectional view on different coil arrangements for window frame kicker magnets. The coil in figure (a) is formed by two filaments of opposite orientation. The coil axis is collinear with the vertical axis of the coordinate system producing a kick force in the horizontal direction. This principle found its application for the SIS18 extraction kicker [7]. In turn, the coil axis in figure (b) is collinear with the horizontal axis of the coordinate system producing a kick force in the vertical direction. This principle has been extended by doubling the number of filaments for the SIS100 extraction kicker which is shown in figure (c).

A current I_K in the coil winding produces a magnetic field in the window region. With the exception of edge effects the average magnetic flux density can be calculated using AMPERE's law:

$$\int_{\partial A} \underline{\vec{H}} \cdot \mathrm{d}\vec{s} = \underline{\Theta}_\mathrm{mag} = n_\mathrm{K}\underline{I}_\mathrm{K} \rightarrow \underline{B}_x \approx \frac{\mu_0 n_\mathrm{K} \underline{I}_\mathrm{K}}{2y_1} \tag{6.1}$$

The vertical aperture measures $2y_1$ and n_K equals the number of turns (filament pairs) of the coil winding. The flux linkage between coil winding and a vertically displaced particle beam represented by a current loop of width d_y and length l can be written as:

$$\int_{A} \underline{\vec{B}} \cdot \mathrm{d}\vec{A} = \underline{\Phi}_\mathrm{B}(d_{y,1}) = \frac{\mu_0 n_\mathrm{K} \underline{I}_\mathrm{K} l}{2y_1} d_{y,1} \tag{6.2}$$

The *mutual inductance* is defined as the magnetic flux produced in a secondary coil divided by the current in an inductively-coupled primary coil. In this context, the mutual inductance is identified as:

$$M_{\mathrm{K}}(d_{y,1}) = \frac{\mu_0 n_{\mathrm{K}} l}{2y_1} d_{y,1} \tag{6.3}$$

The mutual inductance M_{K} provides a measure for the inductive coupling between particle beam and kicker coil and vice versa (reciprocity). Thus, a displaced beam induces the voltage U_{K} in the coil winding:

$$\underline{U}_{\mathrm{K}}(d_{y,1}) = M_{\mathrm{K}}(d_{y,1}) \frac{\mathrm{d}}{\mathrm{d}t} \underline{I}_{\mathrm{B}} = j\omega M_{\mathrm{K}}(d_{y,1}) \underline{I}_{\mathrm{B}} \tag{6.4}$$

This voltage drives a current I_{K} in the closed loop circuit consisting of the coil reactance $j\omega L_{\mathrm{K}}$ and the generator impedance Z_{G}:

$$\underline{I}_{\mathrm{K}}(d_{y,1}) = \frac{\underline{U}_{\mathrm{K}}(d_{y,1})}{\underline{Z}_{\mathrm{G}} + j\omega L_{\mathrm{K}}} \tag{6.5}$$

In turn, the current flow in the kicker circuit induces a voltage U_{B} in the beam region:

$$\underline{U}_{\mathrm{B}}(d_{y,1}, d_{y,2}) = -M_{\mathrm{K}}(d_{y,2}) \frac{\mathrm{d}}{\mathrm{d}t} \underline{I}_{\mathrm{K}}(d_{y,1}) \tag{6.6a}$$

$$= -j\omega M_{\mathrm{K}}(d_{y,2}) \frac{\underline{U}_{\mathrm{K}}(d_{y,1})}{\underline{Z}_{\mathrm{G}} + j\omega L_{\mathrm{K}}} \tag{6.6b}$$

$$= \frac{\omega^2 M_{\mathrm{K}}(d_{y,1}) M_{\mathrm{K}}(d_{y,2}) \underline{I}_{\mathrm{B}}}{\underline{Z}_{\mathrm{G}} + j\omega L_{\mathrm{K}}} \tag{6.6c}$$

The quotient $Z_{\mathrm{B}}(d_{y,1}, d_{y,2}) = U_{\mathrm{B}}/I_{\mathrm{B}}$ defines an impedance from which the following relations are obtained for the longitudinal and transverse coupling impedance [32]:

$$\underline{Z}_{||,\mathrm{G}}(\omega) = \underline{Z}_{\mathrm{B}}(d_{y,1}, d_{y,2})\Big|_{d_{y,1}=d_{y,2}=d_y} \tag{6.7a}$$

$$= \frac{\omega^2 M_{\mathrm{K}}^2(d_y)}{\underline{Z}_{\mathrm{G}} + j\omega L_{\mathrm{K}}} \tag{6.7b}$$

$$= \frac{\omega^2 n_{\mathrm{K}}^2 \mu_0^2 l^2 d_y^2}{4y_1^2 \left(\underline{Z}_{\mathrm{G}} + j\omega L_{\mathrm{K}}\right)} \tag{6.7c}$$

$$\underline{Z}_{y,\mathrm{G}}(\omega) = \frac{c_0}{\omega} \frac{\partial^2 \underline{Z}_\mathrm{B}(d_{y,1}, d_{y,2})}{\partial d_{y,1} \partial d_{y,2}} \bigg|_{d_{y,1}=d_{y,2}=d_y} \tag{6.8a}$$

$$= \frac{c_0 \omega n_\mathrm{K}^2 \mu_0^2 l^2}{4 y_1^2 \left(\underline{Z}_\mathrm{G} + j\omega L_\mathrm{K}\right)} \tag{6.8b}$$

The contribution of the circuit impedance to the longitudinal coupling impedance strongly depends on the transverse displacement of the particle beam. The contribution to the horizontal coupling impedance does not depend on the transverse position but the unit Ω/m indicates that this a normalized impedance with respect to the transverse displacement. Similar results have been published in [38].

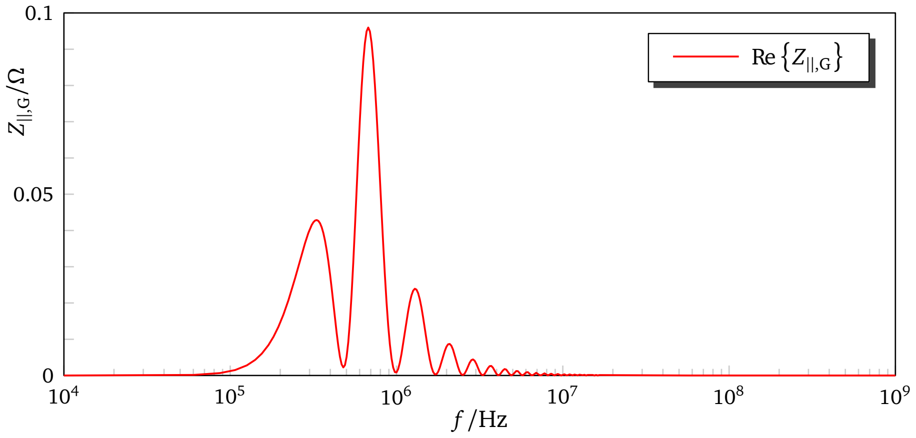

(a)

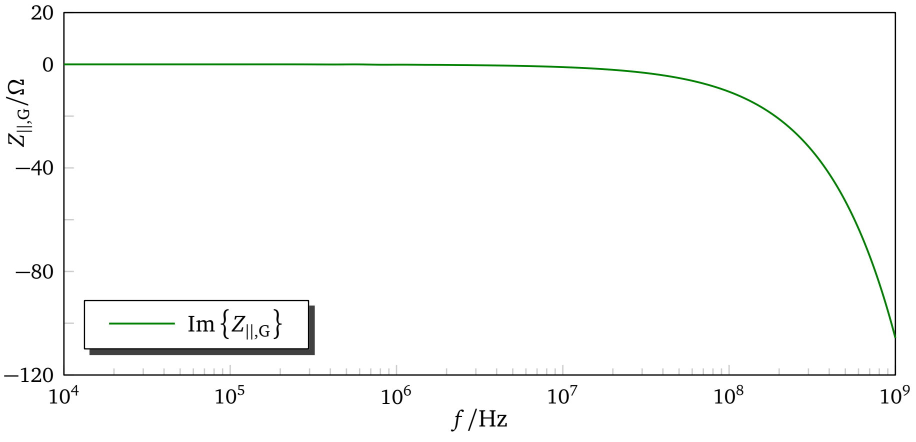

(b)

Figure 6.11.: Real and imaginary part of the longitudinal impedance contribution caused by the external kicker circuit. The parameter n_K takes the value 2 due to the double-turn coil geometry and y_1 has been set to 4cm to match the vertical dimension of the magnet aperture. The length l has been chosen as 75cm which equals the length of a single ferrite block.

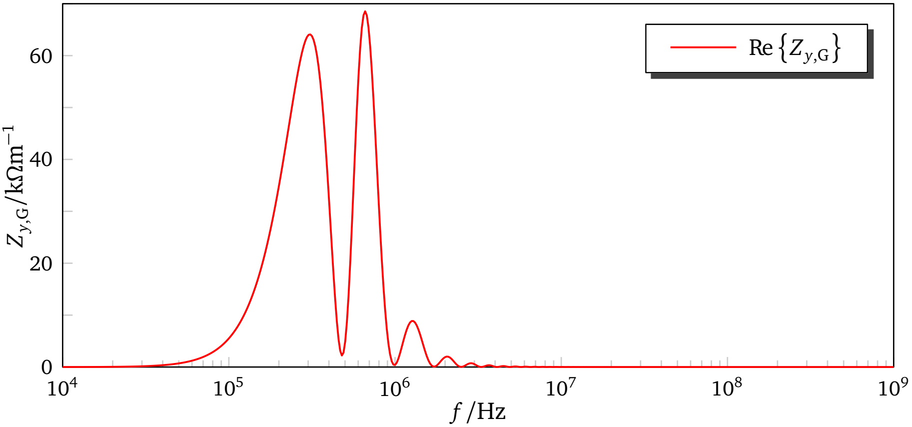

(a)

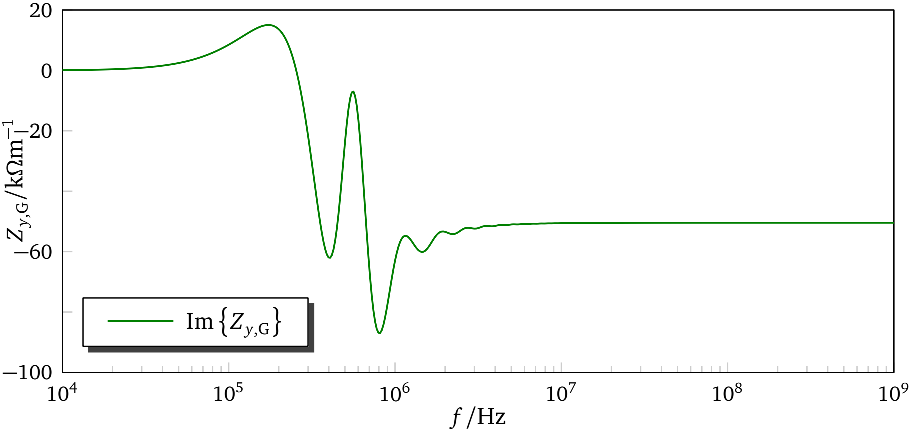

(b)

Figure 6.12.: Real and imaginary part of the vertical impedance contribution caused by the external kicker circuit. The parameter n_K takes the value 2 due to the double-turn coil geometry and y_1 has been set to 4cm to match the vertical dimension of the magnet aperture.

6.3 Coupling impedance contributions caused by the SIS100 kicker magnet

In this section the simulation results for the computational model of the SIS100 kicker magnet are presented. Different computational models have been investigated. In the first instance the case of ultra-relativistic beam ($\beta = 1.0$) is considered for a simplified kicker model consisting of a ferrite yoke having the actual dimensions. The yoke is located in a larger cuboid-shaped vacuum chamber with perfect-conducting walls.

A cylinder-shaped vaccum chamber has been used for the second model to have a more realistic representation of the actual vessel and check for the impact of curvature discretization by the mesh.

6.3.1 Coupling Impedance contribution of a single kicker module with cuboid chamber in the ultra-relativistic limit.

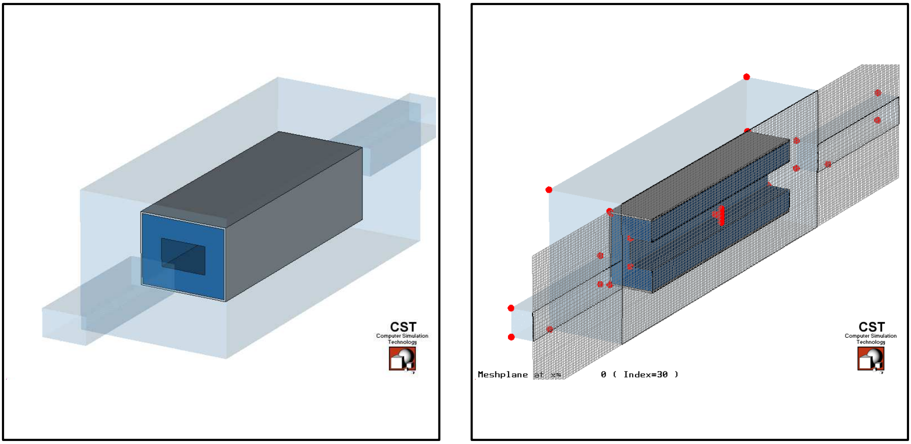

(a) (b)

Figure 6.13.: Computational model of a simplified magnet with cuboid vacuum chamber shown with and without hexahedral mesh.

The beam is represented by a current path at the center for a monopolar source field or by two symmetrically displaced current paths with opposite directions to produce a dipolar source field.

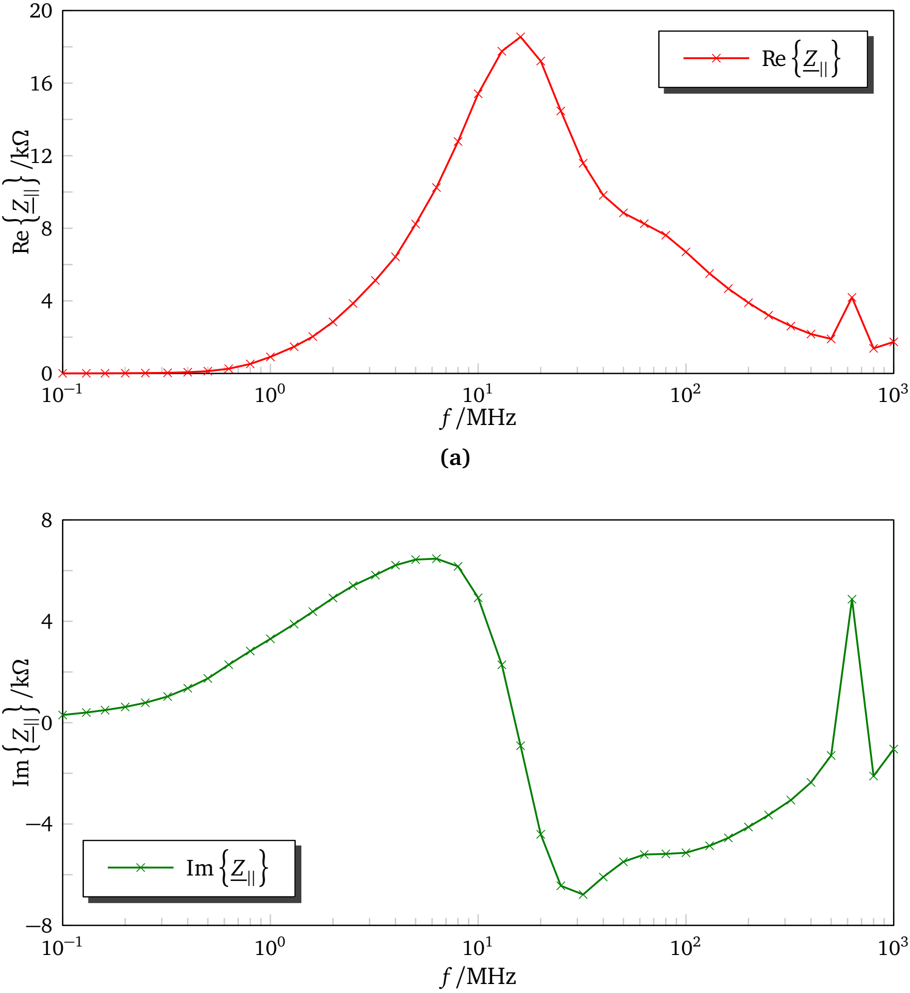

(a)

(b)

Figure 6.14.: Real and imaginary part of the longitudinal coupling impedance caused by the presence of the ferrite yoke in a cuboid-shaped vacuum chamber. The beam is represented by a point-shaped current filament at the center. The peaks around 600MHz indicate a TM_{11} type resonance, which is related to the dimensions chosen for the vacuum chamber. This has been verfied separately by increasing the number of frequency samples between 5×10^2 and 10^3 Megahertz.

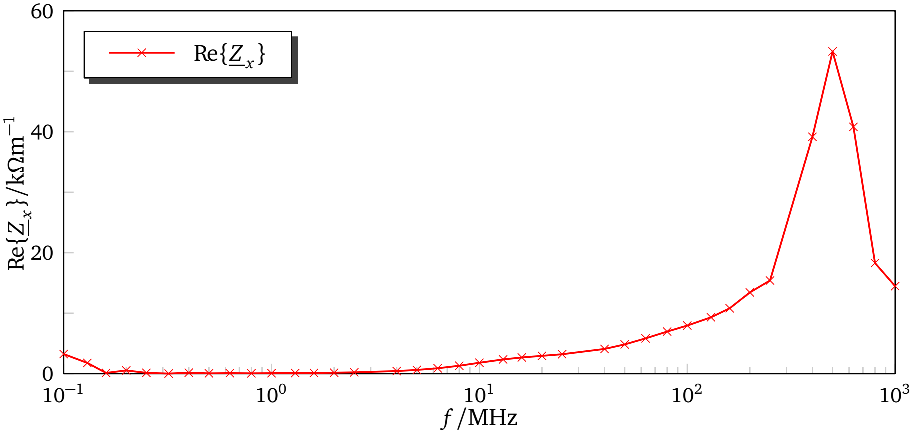

(a)

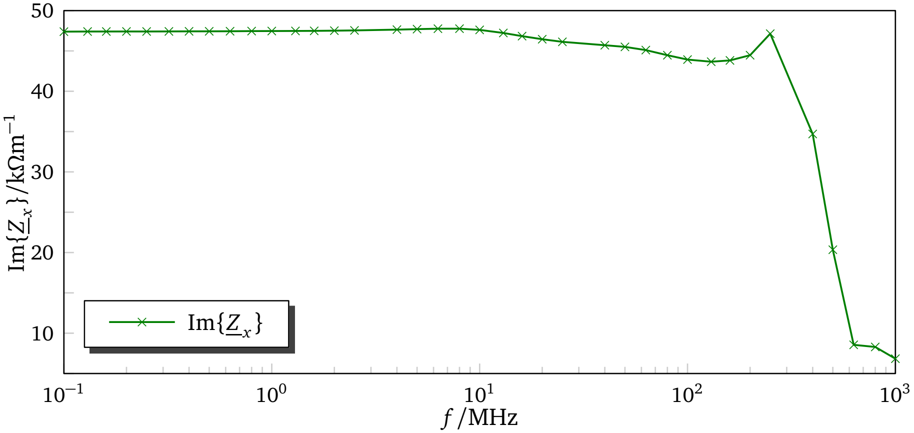

(b)

Figure 6.15.: Real and imaginary part of the horizontal coupling impedance caused by the presence of the ferrite yoke in a cuboid-shaped vacuum chamber.

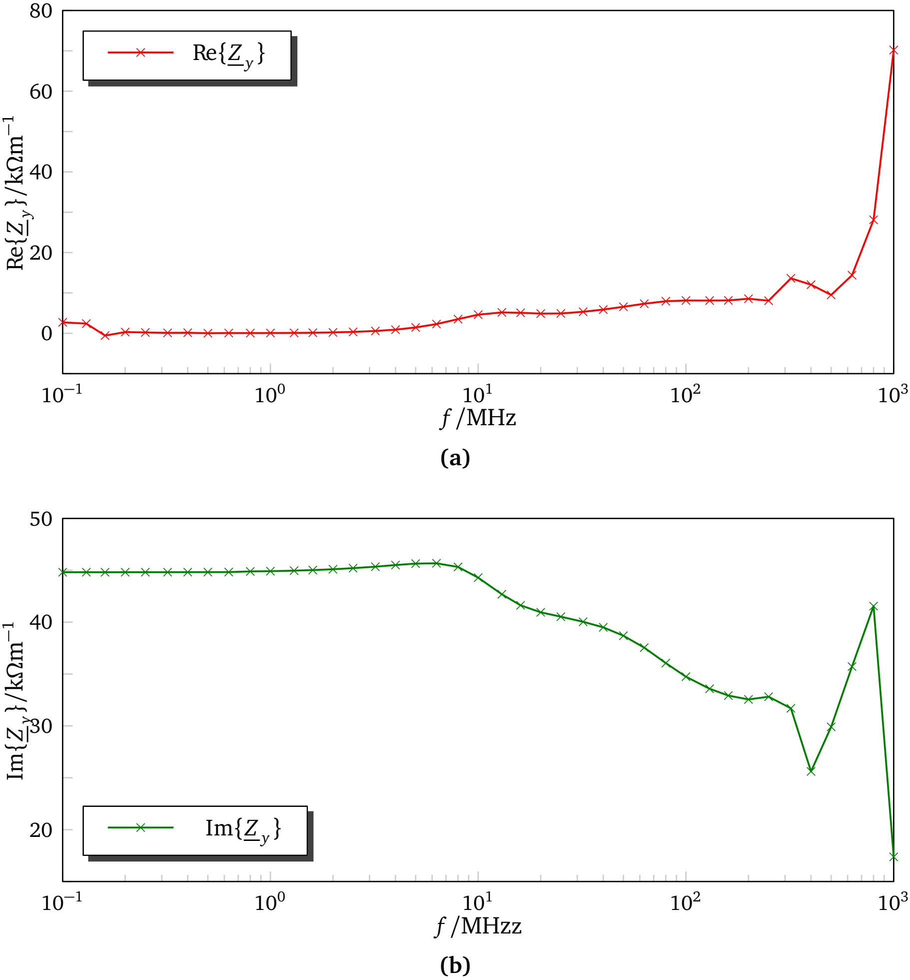

Figure 6.16.: Real and imaginary part of the vertical coupling impedance caused by the presence of the ferrite yoke in a cuboid-shaped vacuum chamber.

6.3.2 Coupling Impedance contribution of a single kicker module with cylindrical chamber in the ultra-relativistic limit.

The previous calculations have been repeated with altered geometry: the previously cuboid vacuum chamber and adjacent beam pipe stubs have been replaced with a cylindrical geometry which is more similar to the actual beamline situation. Approximation of curved geometry by staircase mesh can lead to inaccurate results, depending on how coarse the discretization has been chosen. In the present case there is practically no effect on the results for the coupling impedance, since geometrical effects are negligible compared with the influence of the ferrite parts.

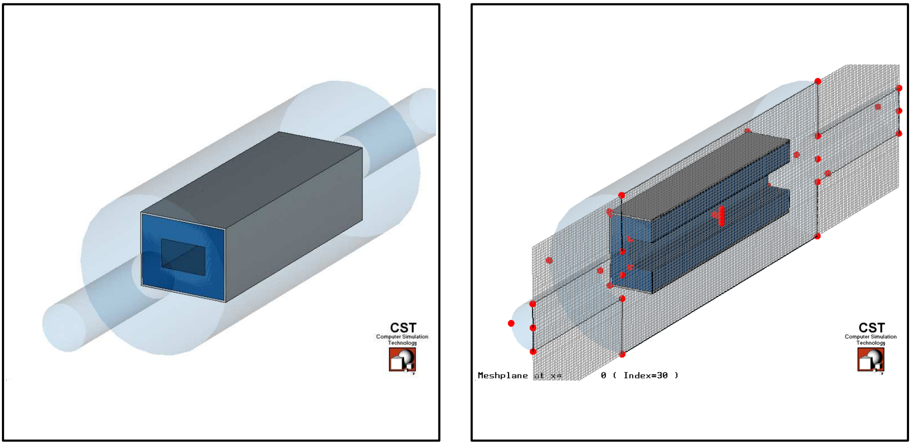

(a) **(b)**

Figure 6.17.: Computational model of a simplified magnet with cylindrical vacuum chamber shown with and without hexahedral mesh. The previously cuboid vacuum chamber and adjacent beam pipe stubs have been replaced with a cylindrical geometry.

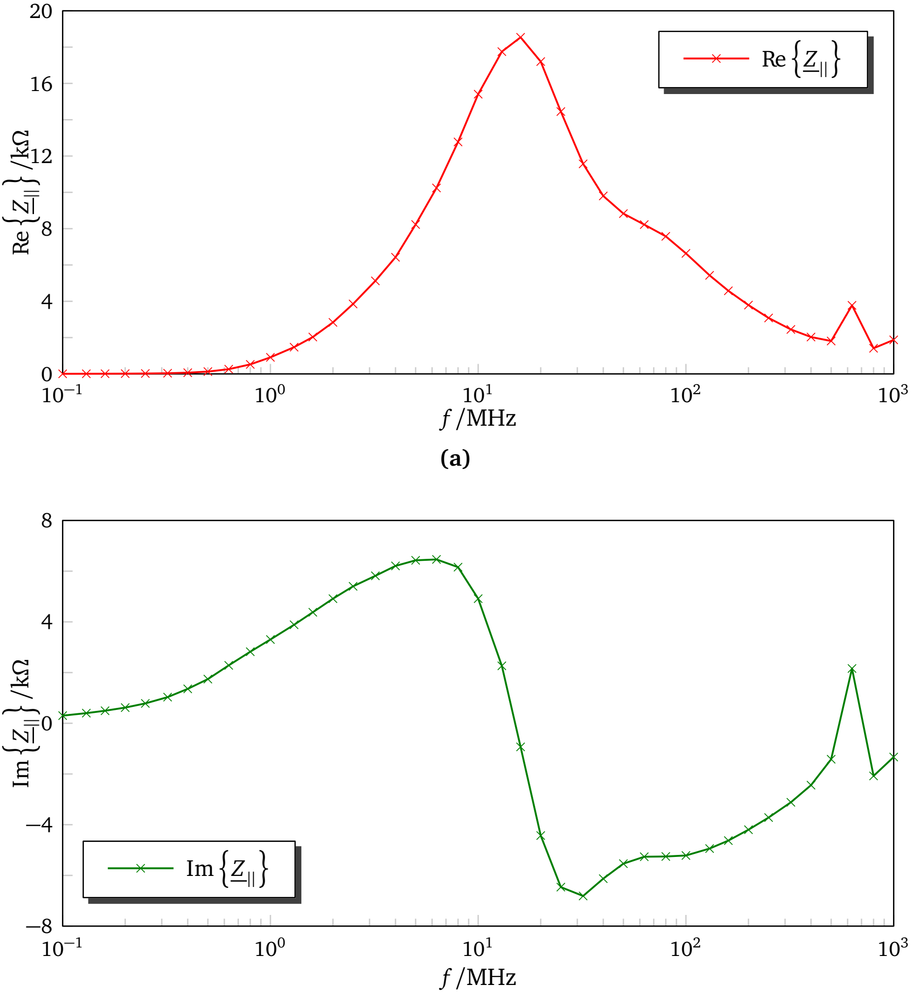

(a)

(b)

Figure 6.18.: Real and imaginary part of the longitudinal coupling impedance caused by the presence of the ferrite yoke in a cylinder-shaped vacuum chamber.

6.3.3 Coupling Impedance contribution of a single kicker module with cuboid chamber and moderate beam velocity.

The frequency domain formulation for the source field contains a frequency-dependent phase angle which describes the feedback action of preceeding wake fields on subsequent particles. In the previous sections ultra-relativistic conditions were assumed where the source field resembles a TEM wave and the phase angle vanishes. Consequently, there exists no feedback action through direct or indirect space charge on subsequent particles. Therefore the coupling impedance does not dependend on the transverse current distribution of the source field for ultra-relativistic conditions. In the general case for velocities lower than c_0 space charge will contribute to the coupling impedance depending on the transverse current distribution of the source field.

While the limit of a point source is practicable from the mathematical point of view, problems arise from the viewpoint of simulation codes. The reason lies in the fact that the computational domain including the sources is discretized by some means which implys finite dimensions for all geometry. In the present case of the Finite Integration Technique current densities are allocated on the facets of the dual grid. The current density is given by the total current and the surface area of the corresponding facet which is perforated by the current path. Thus, the mesh density of the discretization may strongly influence the representation of the source field.

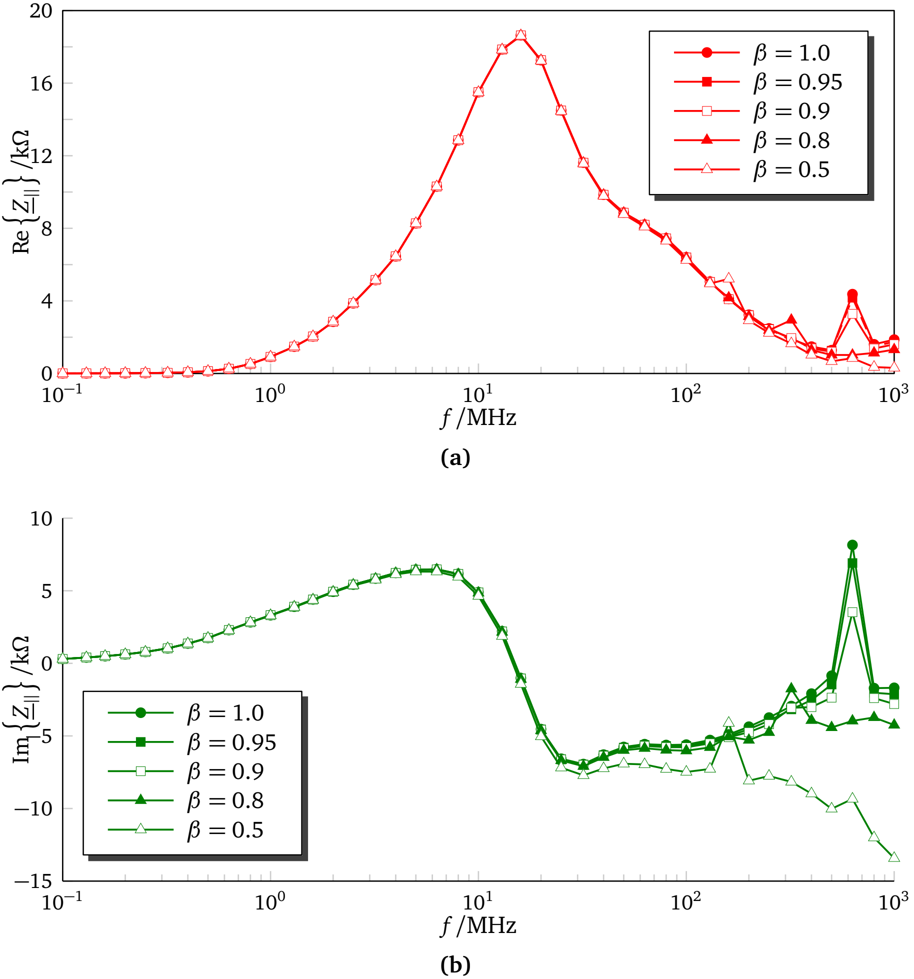

Figure 6.19.: Real and imaginary part of the longitudinal coupling impedance for different beam velocities. The previous model with a cuboid vacuum chamber was used. Mesh settings have been retained throughout all velocities.

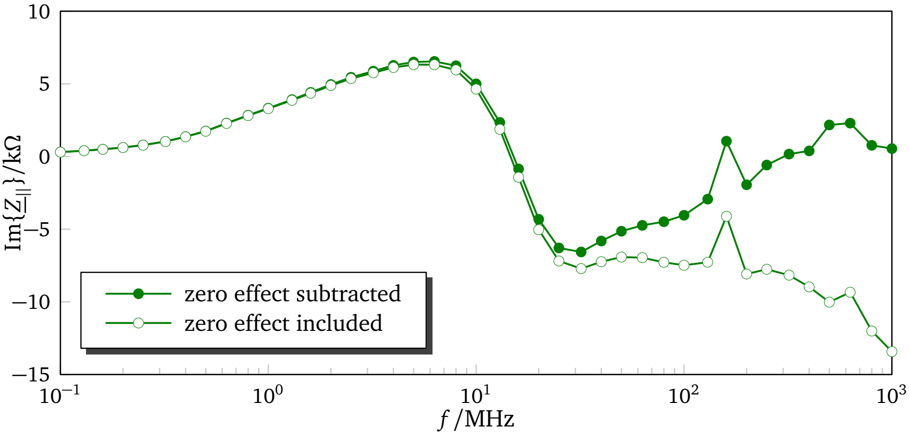

(a)

Figure 6.20.: Imaginary part of the longitudinal coupling impedance for different beam velocities of vacuum chamber without the ferrite block. As there is no loss of beam energy without the presence of lossy media, the real part is zero.

6.4 Beam induced heating

The real part of the coupling impedance is directly related to energy loss or gain of the particle beam. Electromagnetic energy which is lost by the beam is absorbed by lossy media of the beamline components and turned into heat. The average absorbed power can be calculated from the bunch spectrum. The results indicate a power deposit of 0.55kW per module for the proton beam.

Particle	No. of bunches	No. of ions per bunch	T_b/ns	E_{kin}/GeV
proton H^+	1	2×10^{13}	50	29
uranium ion U^{28+}	1	4×10^{11}	70	1.5

Table 6.2.: Exemplary bunch parameters for the operation of the SIS100 accelerator [8]. A parabolic pulse shape is assumed for the longitudinal charge distribution with a total pulse length of T_b.

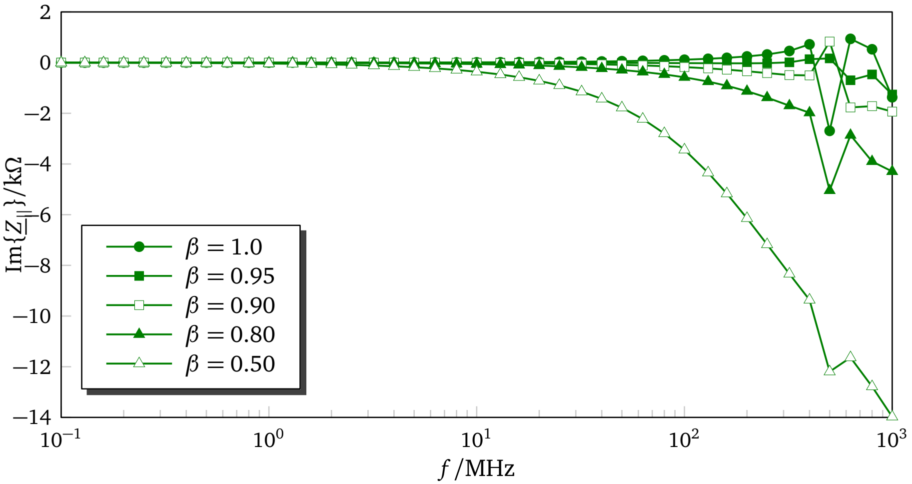

(a)

Figure 6.21.: It is often convenient to subtract the zero effect i.e. without lossy media from the previous result. The figure shows a comparison between the original result with and without subtracting the zero effect for $\beta = 0.5$.

6.5 Further applications

In the previous sections simulation models of a single kicker module has been used which is sufficiently resolved with less than 100000 mesh cells. Tests have shown that problem sizes of at least a few million mesh cells can be implemented at the cost of increased computation time. This allows for parameter studies of geometrical variations, resolving fine details or simulation of larger building blocks.

7 Conclusion

One of the primary objectives was to get a better understanding of charged particle beam electrodynamics, the mathematical description in both time and frequency domain and establish the links to actual physics and numerical modeling. Beam coupling impedances are the measure of choice to evaluate beam-induced electromagnetic fields and their feedback action on the particle beam itself.

Many publications exist focusing on the coupling impedance contributions of lossy media. The various analytical, numerical or experimental approaches often differ with respect to the assumptions being made, prerequisites and applicability. Much less contributions can be found where different methods are compared with each other, thus, another objective was to bring them in line and proove agreement.

Since the author's background lies in the field of electromagnetic field simulation, this thesis focuses on analytical methods and simulation techniques. Analytical methods are usually restricted to symmetrical geometry and may solely serve as approximation of real geometries or to proove the applicability of numerical methods. Finally, more accurate prognosis is only possible with 3D numerical simulation models. Numerical simulation techniques have been established in the second half of the last century and have a accompanied the construction of large particle accelerators. Classical time domain codes were the prevailing simulation tools where the actual process of the particle motion sequence is reproduced. Thereby, mainly coupling impedance contributions above cut-off were of interest and the ultra-relativistic approximation was suitable for many applications. For the present case of a heavy ion synchrotron accelerator, particle velocities significantly lower than speed of light occur and coupling impedances in the frequency regime below cut-off are subject to investigation. With the occurence of moderate beam velocities space charge effects must be considered as well.

Ferrite-loaded beamline devices occur for instance as kicker magnets which allow for an abrupt change of the beam direction of motion when activated. Ferrites show frequency-dependent hysteresis with respect to magnetization and therefore contribute to both real and imaginary parts of the coupling impedance.

After a recapitulation of the most important mathematical relations and definitions, a few reference examples are discussed, which can be treated by means of the classical electromagnetic field theory. After cross-checking simulation results with these analytical results, the focus is put on simulation models that are geared towards actual accelerator components.

Both the classical time domain approach and a specialized frequency domain approach produce reasonable results for reference geometry. The frequency domain approach is used for the practically relevant models. These usually consist of a contigous region of high-permeable media embedded in a larger vacuum region with electrically conductive walls. This material distribution inevitably leads to an ill-conditioned system matrix which in turn leads to bad convergence properties. With increased problem size, the number of iterations increases up to several thousands. For problem sizes consisting of several millions of meshcells, single computations at single frequency points do no longer converge within the given targets. Possible improvement may be achieved with the help of suitable preconditioners or specialized solvers.

However, coupling impedances can be reliably calculated with within this simulation framework, especially for the frequency regime below cut-off and corresponding bunch lengths that are much longer than the simulated device. Thus, not only coupling impedance contributions of kicker magnets can be investigated, but also other problems can be adressed such as beampipes with step transitions, corrugated sections, electrodes of monitoring devices or components with other types of lossy media.

A Deduction of source terms

The expressions for the source terms are based on the following fundamental expressions found in [2]. Let $F \subseteq \mathbb{R}^3$ be a surface of arbitrary shape in 3D position space:

$$F(\vec{r}, t) = 0 \tag{A.1}$$

The charge shall be located on the surface such that the charge density q_V can be expressed by the gradient of a surface charge density q_A and the surface unit vector $\vec{n}$:

$$q_V(\vec{r}, t) = -\vec{n} \cdot \nabla F \tag{A.2}$$

The surface charge density can be expressed with the HEAVISIDE step function :

$$\Theta(F) = \begin{cases} 1 & \text{, for } F = 0 \\ 0 & \text{, for } F \neq 0 \end{cases} \tag{A.3}$$

Consequently, the charge density reads:

$$\begin{align} q_V(\vec{r}, t) &= q_A(\vec{r}, t)\, |\nabla \Theta| \tag{A.4} \\ &= q_A(\vec{r}, t)\, |\nabla F|\, \delta(F) \tag{A.5} \end{align}$$

With the DIRAC delta distribution δ:

$$\delta(F) = \begin{cases} 1 & \text{, for } F = 0 \\ 0 & \text{, for } F \neq 0 \end{cases} \tag{A.6}$$

This surface performs a uniform motion with the velocity v and can be expressed as:

$$F(\vec{r}, t) = f(\vec{r}) - v t \tag{A.7}$$

The function f contains the shape information of the surface and can be TAYLOR expanded about $\vec{r}$ [AS72] :

$$f(\vec{r}-\vec{r}_q)=\sum_{\alpha=0}^{\infty}\frac{(-1)^{\alpha}}{\alpha!}\left(\vec{r}_q\cdot\nabla_{\vec{r}'}\right)^{\alpha}f(\vec{r}')\Big|_{\vec{r}'=\vec{r}} \tag{A.8a}$$

$$=f(\vec{r})-\left(\vec{r}_q\cdot\nabla_{\vec{r}'}\right)f(\vec{r}')\Big|_{\vec{r}'=\vec{r}}+\frac{1}{2}\left(\vec{r}_q\cdot\nabla_{\vec{r}'}\right)^{2}f(\vec{r}')\Big|_{\vec{r}'=\vec{r}}-\cdots \tag{A.8b}$$

The spatial charge distribution will now be limited to the transverse plane such that the surface can be expressed as:

$$F(z,t)=z-vt\Rightarrow|\nabla F|=1 \tag{A.9}$$

Consequently, the charge density now reads:

$$q_V(\vec{r}_\perp,z,t)=q_A(\vec{r}_\perp)\delta(z-vt) \tag{A.10}$$

If charge is equally distributed on a circular disc of radius a, then the surface charge density can be expressed by means of the HEAVISIDE step function Θ:

$$q_A(\vec{r}_\perp)=\frac{Q}{\pi a^2}\Theta(a-|\vec{d}-\vec{r}_\perp|) \tag{A.11}$$

By introducing $u=|\vec{d}-\vec{r}_\perp|$, the following expansion is obtained:

$$\begin{aligned}\Theta(a-u)=&\,\Theta(a-r_\perp)+((a-u)-(a-r_\perp))\left.\frac{d\Theta(a-u)}{d(a-u)}\right|_{a-u=a-r_\perp}\\&+\frac{1}{2}((a-u)-(a-r_\perp))^2\left.\frac{d^2\Theta(a-u)}{d(a-u)^2}\right|_{a-u=a-r_\perp}+\cdots\end{aligned} \tag{A.12a}$$

$$\begin{aligned}=&\,\Theta(a-r_\perp)+(r_\perp-u)\,\delta(a-r_\perp)\\&+\frac{1}{2}(r_\perp-u)^2\left.\frac{d\delta(a-u)}{d(a-u)}\right|_{a-u=a-r_\perp}+\cdots\end{aligned} \tag{A.12b}$$

The argument $r_\perp-u$ is expanded in order to obtain a more compact formulation:

$$
\begin{aligned}
r_\perp - u &= r_\perp - \sqrt{d^2 + r_\perp^2 - 2r_\perp d\cos(\varphi-\varphi_0)} && \text{(A.13a)}\\
&= r_\perp - r_\perp\left[1 + \frac{1}{2}\left(\frac{d^2 - 2r_\perp d\cos(\varphi-\varphi_0)}{r_\perp^2}\right)\right.\\
&\left.-\frac{1}{8}\left(\frac{d^2 - 2r_\perp d\cos(\varphi-\varphi_0)}{r_\perp^2}\right)^2 + \cdots\right] && \text{(A.13b)}\\
&= d\cos(\varphi-\varphi_0) - \frac{d^2}{2r_\perp}(1-\cos(\varphi-\varphi_0)) - \frac{d^3}{2r_\perp^2}\cos(\varphi-\varphi_0) + \frac{d^4}{8r_\perp^3}\\
&= d\cos(\varphi-\varphi_0) - \frac{d^2}{r_\perp}\sin^2(\varphi-\varphi_0) - \frac{d^3}{2r_\perp^2}\cos(\varphi-\varphi_0) + \frac{d^4}{8r_\perp^3}\\
&= d\cos(\varphi-\varphi_0) - \frac{d^2}{2r_\perp}(1-\cos(2(\varphi-\varphi_0))) - \frac{d^3}{2r_\perp^2}\cos(\varphi-\varphi_0) + \frac{d^4}{8r_\perp^3}\\
&= \left(d - \frac{d^3}{2r_\perp^2}\right)\cos(\varphi-\varphi_0) + \frac{d^2}{2r_\perp^2}\cos(2(\varphi-\varphi_0)) - \frac{d^2}{2r_\perp^2} + \frac{d^4}{8r_\perp^3} && \text{(A.13c)}
\end{aligned}
$$

To first order $\frac{d^2}{2r_\perp^2}, \frac{d^3}{2r_\perp^2}, \frac{d^4}{8r_\perp^3} << d$ is assumed, which leads to:

$$
r_\perp - u \approx d\cos(\varphi-\varphi_0) \qquad \text{(A.14)}
$$

The charge density has been decomposed into a surface charge density that is assigned to the transverse plane and a line density that is assigned to the longitudinal axis. The line density is expressed by means of the Dirac delta function, while the surface density is expressed by means of the Heaviside function. The charge density and the current density read:

$$
\begin{aligned}
q_V(\vec{r}_\perp, z, t) &\approx \frac{Q}{\pi a^2}\left(\Theta(a-r_\perp) + d\cos(\varphi-\varphi_0)\delta(a-r_\perp)\right)\delta(z-vt) && \text{(A.15a)}\\
\vec{J}_\beta(\vec{r}_\perp, z, t) &\approx v\frac{Q}{\pi a^2}\left(\Theta(a-r_\perp) + d\cos(\varphi-\varphi_0)\delta(a-r_\perp)\right)\delta(z-vt)\vec{e}_z && \text{(A.15b)}
\end{aligned}
$$

For a separate treatment of the horizontal and vertical displacement:

$$
\begin{aligned}
\vec{d} &= d_x\vec{e}_x \quad (\varphi_0 = 0, d_y = 0) && \text{(A.16a)}\\
\vec{d} &= d_y\vec{e}_y \quad (\varphi_0 = \pi/2, d_x = 0) && \text{(A.16b)}
\end{aligned}
$$

By truncating the TAYLOR expansion after the second term, an approximation is obtained which characterizes the charge and the current density by a monopolar term and a dipolar term. It is possible to produce either the monopolar term or the dipolar term through superposition of two source fields with opposite displacements $\vec{d}$ and $-\vec{d}$, respectively. This representation originates from experimental setups where the source field is produced with a twin wire arrangement.

$$\vec{J}_{\beta,\uparrow\uparrow}(\vec{r}_\perp, z, t) = v\frac{Q}{\pi a^2}\left[\frac{1}{2}\Theta(a - |\vec{d} - \vec{r}_\perp|) + \frac{1}{2}\Theta(a - |\vec{d} + \vec{r}_\perp|)\right]\delta(z - vt)\vec{e}_z \quad \text{(A.17a)}$$

$$\vec{J}_{\beta,\uparrow\downarrow}(\vec{r}_\perp, z, t) = v\frac{Q}{\pi a^2}\left[\frac{1}{2}\Theta(a - |\vec{d} - \vec{r}_\perp|) - \frac{1}{2}\Theta(a - |\vec{d} + \vec{r}_\perp|)\right]\delta(z - vt)\vec{e}_z \quad \text{(A.17b)}$$

Equation A.17a describes the current distribution for two circular current profiles with opposite displacement and parallel orientation. Equation A.17b describes the current distribution for two circular current profiles with opposite displacement and antiparallel orientation. By truncating the corresponding TAYLOR expansions, two approximations are obtained. The charge and current density for parallel orientation reads:

$$q_{V\uparrow\uparrow}(\vec{r}_\perp, z, t) \approx \frac{Q}{\pi a^2}\Theta(a - r_\perp)\delta(z - vt) \quad \text{(A.18a)}$$

$$\vec{J}_{\beta\uparrow\uparrow}(\vec{r}_\perp, z, t) \approx v\frac{Q}{\pi a^2}\Theta(a - r_\perp)\delta(z - vt)\vec{e}_z \quad \text{(A.18b)}$$

The charge and current density for antiparallel orientation reads:

$$q_{V\uparrow\downarrow}(\vec{r}_\perp, z, t) \approx \frac{Qd}{\pi a^2}\cos(\varphi - \varphi_0)\delta(a - r_\perp)\delta(z - vt) \quad \text{(A.19a)}$$

$$\vec{J}_{\beta\uparrow\downarrow}(\vec{r}_\perp, z, t) \approx v\frac{Qd}{\pi a^2}\cos(\varphi - \varphi_0)\delta(a - r_\perp)\delta(z - vt)\vec{e}_z \quad \text{(A.19b)}$$

Conclusively, this arrangement can be used to restrict the source field either to the zeroth or first order momentum, which is of practical relevance in bench measurement setups or implementation of simulation tools.

B Deduction of the inhomogenous wave equation

Applying the curl operator to 2.1a and 2.1a yields:

$$\operatorname{curl}\left(\operatorname{curl}\vec{E}\right) = -\frac{\partial}{\partial t}\operatorname{curl}\vec{B} \tag{B.1a}$$

$$\operatorname{curl}\left(\operatorname{curl}\mu\vec{H}\right) = \mu\operatorname{curl}\vec{J} + \varepsilon\mu\frac{\partial}{\partial t}\operatorname{curl}\vec{E} \tag{B.1b}$$

Resolving the curl-curl operator yields:

$$\operatorname{grad}\left(\operatorname{div}\vec{E}\right) - \nabla^2\vec{E} = -\frac{\partial}{\partial t}\left(\mu\vec{J} + \varepsilon\mu\frac{\partial}{\partial t}\vec{E}\right) \tag{B.2a}$$

$$\operatorname{grad}\left(\operatorname{div}\left(\mu\vec{H}\right)\right) - \nabla^2\left(\mu\vec{H}\right) = -\mu\operatorname{curl}\vec{J} + \varepsilon\mu\frac{\partial}{\partial t}\left(-\frac{\partial}{\partial t}\left(\mu\vec{H}\right)\right) \tag{B.2b}$$

Substituting with the adequate expressions from 2.1c and 2.1d yields:

$$\nabla^2\vec{E} - \varepsilon\mu\frac{\partial^2}{\partial t^2}\vec{E} = \frac{\partial}{\partial t}\mu\vec{J} + \operatorname{grad}\left(\frac{q_V}{\varepsilon}\right) \tag{B.3a}$$

$$\nabla^2\left(\mu\vec{H}\right) - \varepsilon\mu\frac{\partial^2}{\partial t^2}\left(\mu\vec{H}\right) = -\mu\operatorname{curl}\vec{J} \tag{B.3b}$$

Equations B.3a and B.3b are the vector wave equations for non-vanishing source terms. The corresponding formulations in frequency domain read:

$$\nabla^2\underline{\vec{E}} + \underline{\varepsilon}\underline{\mu}\omega^2\underline{\vec{E}} = j\omega\underline{\mu}\underline{\vec{J}} + \operatorname{grad}\left(\frac{\underline{q}_V}{\varepsilon_0\underline{\varepsilon}_{\mathrm{r}}}\right) \tag{B.4a}$$

$$\nabla^2\left(\underline{\mu}\underline{\vec{H}}\right) + \underline{\varepsilon}\underline{\mu}\omega^2\left(\underline{\mu}\underline{\vec{H}}\right) = -\underline{\mu}\operatorname{curl}\underline{\vec{J}} \tag{B.4b}$$

C Solutions for cylindrical geometry

Matching conditions for $\underline{E}_z$ and $\underline{H}_z$ according 4.16:

$$\begin{aligned}
\cos(m_{E,i}\varphi)\left(\underline{C}_{I,E,i}\underline{I}_{m_{E,i}}(k_{\varrho,i}\varrho_i)+\underline{C}_{K,E,i}\underline{K}_{m_{E,i}}(k_{\varrho,i}\varrho_i)\right) &= \\
\cos(m_{E,i+1}\varphi)\left(\underline{C}_{I,E,i+1}\underline{I}_{m_{E,i+1}}(k_{\varrho,i+1}\varrho_{i+1})+\underline{C}_{K,E,i+1}\underline{K}_{m_{E,i+1}}(k_{\varrho,i+1}\varrho_{i+1})\right) & \qquad \text{(C.1a)} \\
\sin(m_{H,i}\varphi)\left(\underline{C}_{I,H,i}\underline{I}_{m_{H,i}}(k_{\varrho,i}\varrho_i)+\underline{C}_{K,H,i}\underline{K}_{m_{H,i}}(k_{\varrho,i}\varrho_i)\right) &= \\
\sin(m_{H,i+1}\varphi)\left(\underline{C}_{I,H,i+1}\underline{I}_{m_{H,i+1}}(k_{\varrho,i+1}\varrho_{i+1})+\underline{C}_{K,H,i+1}\underline{K}_{m_{H,i+1}}(k_{\varrho,i+1}\varrho_{i+1})\right) & \qquad \text{(C.1b)}
\end{aligned}$$

Matching conditions for $\underline{E}_\varphi$ and $\underline{H}_\varphi$:

$$\begin{aligned}
\frac{1}{k^2_{\varrho,i}}\left(\frac{1}{\varrho_i}\frac{\partial}{\partial\varphi}\underline{E}_{z,i}(\varrho_i)-v\underline{\mu}_i\frac{\partial}{\partial\varrho}\underline{H}_{z,i}\bigg|_{\varrho=\varrho_i}\right) &= \\
\frac{1}{k^2_{\varrho,i+1}}\left(\frac{1}{\varrho_i}\frac{\partial}{\partial\varphi}\underline{E}_{z,i+1}(\varrho_i)-v\underline{\mu}_{i+1}\frac{\partial}{\partial\varrho}\underline{H}_{z,i+1}\bigg|_{\varrho=\varrho_i}\right) & \qquad \text{(C.2a)} \\
\frac{1}{k^2_{\varrho,i}}\left(v\underline{\varepsilon}_i\frac{\partial}{\partial\varrho}\underline{E}_{z,i}\bigg|_{\varrho=\varrho_i}+\frac{1}{\varrho_i}\frac{\partial}{\partial\varphi}\underline{H}_{z,i}(\varrho_i)\right) &= \\
\frac{1}{k^2_{\varrho,i+1}}\left(v\underline{\varepsilon}_{i+1}\frac{\partial}{\partial\varrho}\underline{E}_{z,i+1}\bigg|_{\varrho=\varrho_i}+\frac{1}{\varrho_i}\frac{\partial}{\partial\varphi}\underline{H}_{z,i+1}(\varrho_i)\right) & \qquad \text{(C.2b)}
\end{aligned}$$

The solutions for $\underline{E}_z$ and $\underline{H}_z$ are substituted according equations 4.9a and 4.9b, respectively:

$$\begin{aligned}
&\frac{m_{E,i}}{\varrho_i k_{\varrho,i}^2}\sin(m_{E,i}\varphi)\Big(\underline{C}_{E,I,i}\underline{I}_{m_E,i}(k_{\varrho,i}\varrho_i)+\underline{C}_{E,K,i}\underline{K}_{m_E,i}(k_{\varrho,i}\varrho_i)\Big)\\
+&\frac{\nu\underline{\mu}_i k_{\varrho,i}}{k_{\varrho,i}^2}\sin(m_{H,i}\varphi)\Big(\underline{C}_{H,I,i}\underline{I}'_{m_H,i}(k_{\varrho,i}\varrho_i)+\underline{C}_{H,K,i}\underline{K}'_{m_H,i}(k_{\varrho,i}\varrho_i)\Big)=\\
&\frac{m_{E,i+1}}{\varrho_i k_{\varrho,i+1}^2}\sin(m_{E,i+1}\varphi)\Big(\underline{C}_{E,I,i+1}\underline{I}_{m_E,i+1}(k_{\varrho,i+1}\varrho_i)+\underline{C}_{E,K,i+1}\underline{K}_{m_E,i+1}(k_{\varrho,i+1}\varrho_i)\Big)\\
+&\frac{\nu\underline{\mu}_{i+1} k_{\varrho,i+1}}{k_{\varrho,i+1}^2}\sin(m_{H,i+1}\varphi)\Big(\underline{C}_{H,I,i+1}\underline{I}'_{m_H,i+1}(k_{\varrho,i+1}\varrho_i)+\underline{C}_{H,K,i+1}\underline{K}'_{m_H,i+1}(k_{\varrho,i+1}\varrho_i)\Big)
\end{aligned}\tag{C.3a}$$

$$\begin{aligned}
&\frac{\nu\underline{\varepsilon}_i k_{\varrho,i}}{k_{\varrho,i}^2}\cos(m_{E,i}\varphi)\Big(\underline{C}_{E,I,i}\underline{I}'_{m_E,i}(k_{\varrho,i}\varrho_i)+\underline{C}_{E,K,i}\underline{K}'_{m_E,i}(k_{\varrho,i}\varrho_i)\Big)\\
+&\frac{m_{H,i}}{\varrho_i k_{\varrho,i}^2}\cos(m_{H,i}\varphi)\Big(\underline{C}_{H,I,i}\underline{I}_{m_H,i}(k_{\varrho,i}\varrho_i)+\underline{C}_{H,K,i}\underline{K}_{m_H,i}(k_{\varrho,i}\varrho_i)\Big)=\\
&\frac{\nu\underline{\varepsilon}_{i+1} k_{\varrho,i+1}}{k_{\varrho,i}^2}\cos(m_{E,i+1}\varphi)\Big(\underline{C}_{E,I,i+1}\underline{I}'_{m_E,i+1}(k_{\varrho,i+1}\varrho_i)+\underline{C}_{E,K,i+1}\underline{K}'_{m_E,i+1}(k_{\varrho,i+1}\varrho_i)\Big)\\
+&\frac{m_{H,i}}{\varrho_i k_{\varrho,i+1}^2}\cos(m_{H,i+1}\varphi)\Big(\underline{C}_{H,I,i+1}\underline{I}_{m_H,i+1}(k_{\varrho,i+1}\varrho_i)+\underline{C}_{H,K,i+1}\underline{K}_{m_H,i+1}(k_{\varrho,i+1}\varrho_i)\Big)
\end{aligned}\tag{C.3b}$$

D Transforms and identities

D.1 Fourier transform

The transform into frequency domain is given by:

$$\underline{F}(\omega) = \mathfrak{F}\{f(t)\} = \int_{-\infty}^{\infty} f(t)e^{-j\omega t}\,\mathrm{d}t \tag{D.1a}$$

The inverse transform back into the time domain is given by:

$$f(t) = \mathfrak{F}^{-1}\left\{\underline{F}(\omega)\right\} = \frac{1}{2\pi}\int_{-\infty}^{\infty} \underline{F}(\omega)e^{j\omega t}\,\mathrm{d}\omega \tag{D.1b}$$

Consequently, physical quantities in the frequency domain are perceived as spectral densities. Contrary to their time domain counterparts the actual unit is divided by the unit of frequency. The physically correct unit is obtained by using the sifting property of the delta distribution:

$$\underline{F}(\omega_1) = \int_{-\infty}^{\infty} \underline{F}(\omega)\delta(\omega-\omega_1)\,\mathrm{d}\omega \tag{D.1c}$$

If the (longitudinal) coupling impedance and the (longitudinal) wake function are connected through Fourier transform the following equations must be satisfied ($\vec{r}_{\perp 1} = \vec{r}_{\perp 2}, s = vt$):

$$\underline{Z}_{||}(\vec{r}_\perp,\omega) = \frac{1}{v}\int_{-\infty}^{\infty} G_{||}(\vec{r}_\perp,s)e^{-j\frac{\omega}{v}s}\,\mathrm{d}s \tag{D.2a}$$

$$= \frac{1}{v}\int_{-\infty}^{\infty} G_{||}(\vec{r}_\perp,vt)e^{-j\omega t}\,\mathrm{d}t = \mathfrak{F}\left\{G_{||}(\vec{r}_\perp,vt)\right\} \tag{D.2b}$$

and the inverse:

$$G_{||}(\vec{r}_\perp, s) = \frac{1}{2\pi} \int\limits_{-\infty}^{\infty} \underline{Z}_{||}(\vec{r}_\perp, \omega) e^{j\frac{\omega}{v}s}\,\mathrm{d}\omega \tag{D.2c}$$

$$= \frac{1}{2\pi} \int\limits_{-\infty}^{\infty} \underline{Z}_{||}(\vec{r}_\perp, \omega) e^{j\omega t}\,\mathrm{d}\omega = \mathfrak{F}^{-1}\left\{\underline{Z}_{||}(\vec{r}_\perp, \omega)\right\} \tag{D.2d}$$

This proof is demonstrated for the longitudinal component of the wake function but can be provided in analogous manner for other components as well.

$$G_{||}(\vec{r}_\perp, s) = \frac{1}{q} \int\limits_{-\infty}^{\infty} E_z(\vec{r}_\perp, z, t = \tfrac{z+s}{v})\,\mathrm{d}z \tag{D.3a}$$

$$= \frac{1}{q} \int\limits_{-\infty}^{\infty} \underbrace{\frac{1}{2\pi} \int\limits_{-\infty}^{\infty} \underline{E}_z(\vec{r}_\perp, z, \omega) e^{j\omega t}\,\mathrm{d}\omega}_{\mathfrak{F}^{-1}\{\underline{E}_z(\vec{r}_\perp, z, \omega)\}}\,\mathrm{d}z \tag{D.3b}$$

The order of integration is interchanged:

$$= \frac{1}{2\pi} \int\limits_{-\infty}^{\infty} \underbrace{\frac{1}{q} \int\limits_{-\infty}^{\infty} \underline{E}_z(\vec{r}_\perp, z, \omega) e^{j\frac{\omega}{v}s}\,\mathrm{d}z}_{\underline{Z}_{||}(\vec{r}_\perp, \omega)}\,\mathrm{d}\omega \tag{D.3c}$$

$$= \mathfrak{F}\left\{\underline{Z}_{||}(\vec{r}_\perp, \omega)\right\} \tag{D.3d}$$

D.2 LORENTZ transform

In the context of this work both inertial systems K and K' have the same orientation, such that all axes of K are aligned in parallel with the corresponding axes of K'. If frame K is regarded as being at rest, then the relative motion of frame K' can be described as a translational motion in the direction of the positive z-axis of constant velocity v. Consequently the following relations are used to switch between the two systems of reference [Hin08, Jac99, Wil96].

The time-space coordinates transform according:

$$x' = x \tag{D.4a}$$

$$y' = y \tag{D.4b}$$

$$z' = \gamma (z - v t) \tag{D.4c}$$

$$t' = \gamma \left(t - \frac{v}{c_0^2} z \right) \tag{D.4d}$$

The components of the electromagnetic field transform according:

$$E_x = \gamma \left(E'_x + v B'_y \right) \tag{D.4e}$$

$$E_y = \gamma \left(E'_y - v B'_x \right) \tag{D.4f}$$

$$E_z = E'_z \tag{D.4g}$$

$$B_x = \gamma \left(B'_x - \frac{v}{c_0^2} E'_y \right) \tag{D.4h}$$

$$B_y = \gamma \left(B'_y + \frac{v}{c_0^2} E'_x \right) \tag{D.4i}$$

$$E_z = E'_z \tag{D.4j}$$

D.3 Selected properties of the (modified) BESSEL functions

Higher derivatives [AS72]:

$$\underline{I}'_m(\underline{\xi}) = \frac{\partial}{\partial \varrho} \underline{I}_m = \underline{I}_{m-1}(\underline{\xi}) - \frac{m}{\underline{\xi}} \underline{I}_m \tag{D.5a}$$

$$\underline{K}'_m(\underline{\xi}) = \frac{\partial}{\partial \varrho} \underline{I}_m = -\underline{K}_{m-1}(\underline{\xi}) - \frac{m}{\underline{\xi}} \underline{K}_m \tag{D.5b}$$

$$\underline{I}'_0(\underline{\xi}) = \underline{I}_1(\underline{\xi}) \tag{D.5c}$$

$$\underline{K}'_0(\underline{\xi}) = -\underline{K}_1(\underline{\xi}) \tag{D.5d}$$

Higher order recurrence:

$$\underline{I}_{m+1}(\underline{\xi}) = \underline{I}_{m-1}(\underline{\xi}) - \frac{2}{\underline{\xi}}\underline{I}_m(\underline{\xi}) \tag{D.6a}$$

$$\underline{K}_{m+1}(\underline{\xi}) = \underline{K}_{m-1}(\underline{\xi}) + \frac{2}{\underline{\xi}}\underline{K}_m(\underline{\xi}) \tag{D.6b}$$

Symmetry with respect to order:

$$\underline{I}_{-m}(\underline{\xi}) = \underline{I}_m(\underline{\xi}) \tag{D.7a}$$

$$\underline{K}_{-m}(\underline{\xi}) = \underline{K}_m(\underline{\xi}) \tag{D.7b}$$

Conjugate-complex argument:

$$\underline{I}_m(\underline{\xi}^*) = \underline{I}_m(\underline{\xi})^* \tag{D.8a}$$

$$\underline{K}_m(\underline{\xi}^*) = \underline{K}_m(\underline{\xi})^* \tag{D.8b}$$

Mixed products:

$$\underline{I}'_m(\underline{\xi})\underline{K}_m(\underline{\xi}) - \underline{I}_m\underline{K}'_m = \frac{1}{\underline{\xi}} \tag{D.9a}$$

(D.9b)

Asymptotic forms:

$$\lim_{\underline{\xi}\to 0} \underline{I}_0(\underline{\xi}) = 1 \tag{D.10a}$$

$$\lim_{\underline{\xi}\to 0} \underline{I}_1(\underline{\xi}) = \frac{\underline{\xi}}{2} \tag{D.10b}$$

$$\lim_{\underline{\xi}\to 0} \underline{K}_0(\underline{\xi}) = -\ln \underline{\xi} \tag{D.10c}$$

$$\lim_{\underline{\xi}\to 0} \underline{K}_1(\underline{\xi}) = \frac{1}{\underline{\xi}} \tag{D.10d}$$

E Green function property of coupling impedances

Obtaining a solution for MAXWELLS equations in a particular regime (Statics, Quasistatics, Dynamics) often leads to solving a inhomogenous linear differential equation:

$$\mathfrak{L}_{\vec{r}}\, u(\vec{r}) = f(\vec{r}) \tag{E.1a}$$

with the solution:

$$u(\vec{r}) = \mathfrak{L}_{\vec{r}}^{-1}\, f(\vec{r}) \tag{E.1b}$$

If the occurence of δ distributions for the source terms on the right hand side is given, certain modifications are required. The GREEN function $\mathfrak{G}$ is an integral kernel representing the inverse operator $\mathfrak{L}_{\vec{r}}^{-1}$ of the linear equation [SG09]:

$$\mathfrak{L}_{\vec{r}}\, \mathfrak{G}(\vec{r},\vec{r}\,') = \delta(\vec{r}-\vec{r}\,') \tag{E.2a}$$

with the solution expressed through an integral ($\vec{r},\ \vec{r}\,' \in V \subseteq \mathbb{R}^3$) :

$$u(\vec{r}) = \int\limits_V \mathfrak{G}(\vec{r},\vec{r}\,') f(\vec{r}\,') d\vec{r}\,' \tag{E.2b}$$

F Circuit analysis

When the kicker is inoperative, the lumped element network simplifies. The effective circuit consists of the transformer secondary inductance, the transmission line, the bridged-T network and the load resistance. In order to obtain Z_G, the circuit must be transformed into a single circuit element.

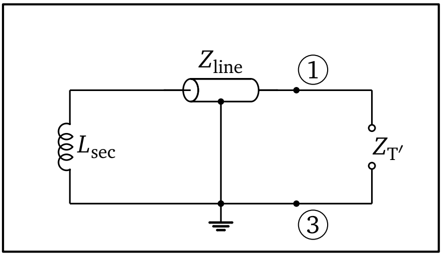

Figure F.1.: The schematic illustrates the impedance transformation of the secondary inductance through the transmission line.

The transmission line results in input-to-output impedance transformation:

$$\underline{Z}'_\mathrm{T} = \underline{Z}_\mathrm{line} \left(\frac{\underline{Z}_\mathrm{T} + \underline{Z}_\mathrm{line} \tanh(\underline{\gamma}_\mathrm{line} L_\mathrm{line})}{\underline{Z}_\mathrm{line} + \underline{Z}_\mathrm{T} \tanh(\underline{\gamma}_\mathrm{line} L_\mathrm{line})} \right) \tag{F.1}$$

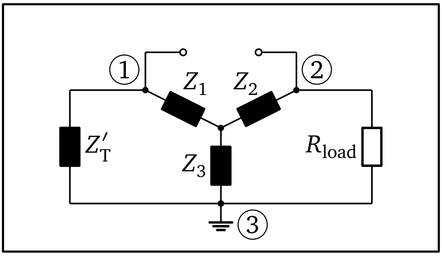

Figure F.2.: The schematic shows the remaining components.

The following circuit elements are defined:

$$\underline{Z}_1 = -\frac{j}{\omega C_\mathrm{T}} \tag{F.2a}$$

$$\underline{Z}_2 = -\frac{j}{\omega C_\mathrm{T}} = \underline{Z}_1 \tag{F.2b}$$

$$\underline{Z}_3 = j\omega L_\mathrm{T} \tag{F.2c}$$

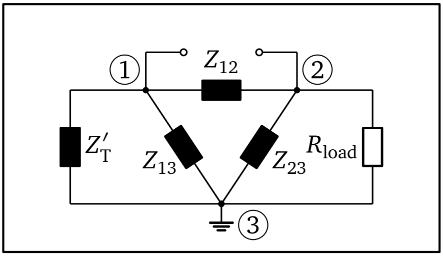

Figure F.3.: The schematic shows the circuit after applying a star-delta transformation.

The star circuit can be transformed into an equivalent delta circuit by application of KENNELLY's theoreme:

$$\underline{Z}_{12} = \frac{\underline{Z}_1\underline{Z}_2 + \underline{Z}_2\underline{Z}_3 + \underline{Z}_1\underline{Z}_3}{\underline{Z}_3} \tag{F.3a}$$

$$\underline{Z}_{13} = \frac{\underline{Z}_1\underline{Z}_2 + \underline{Z}_2\underline{Z}_3 + \underline{Z}_1\underline{Z}_3}{\underline{Z}_2} \tag{F.3b}$$

$$\underline{Z}_{23} = \frac{\underline{Z}_1\underline{Z}_2 + \underline{Z}_2\underline{Z}_3 + \underline{Z}_1\underline{Z}_3}{\underline{Z}_1} \tag{F.3c}$$

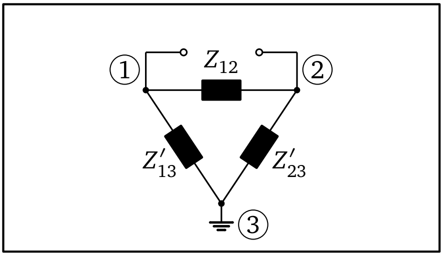

Figure F.4.: The schematic shows the modified components.

The parallel sub-circuits can be combined and yield the new circuit elements:

$$\underline{Z}'_{13} = \frac{\underline{Z}_{13}\underline{Z}'_{\mathrm{T}}}{\underline{Z}_{13} + \underline{Z}'_{\mathrm{T}}} \tag{F.4a}$$

$$\underline{Z}'_{23} = \frac{\underline{Z}_{23}R_{\mathrm{load}}}{\underline{Z}_{23} + R_{\mathrm{load}}} \tag{F.4b}$$

The remaining circuit elements can be combined to yield the total generator impedance as it is perceived at the terminal and includes all relevant components of the kicker circuit in idle state.

This circuit model can be easily extended to include parasitic elements that occur from the kicker bus bar or the coaxial feedthrough. The most simple approach to model the kicker employs a single inductor representing the coil. More sophisticated approaches include losses by addition of resistive elements.

$$\underline{Z}_{\mathrm{G}} = \frac{\underline{Z}_{12}\left(\underline{Z}'_{13} + \underline{Z}'_{23}\right)}{\underline{Z}_{12} + \underline{Z}'_{13} + \underline{Z}'_{23}} \tag{F.5}$$

The following expressions must be substituted:

$$\underline{Z}'_{13} = \frac{\left(\underline{Z}_1^2 + 2\underline{Z}_1\underline{Z}_3\right)\underline{Z}'_\mathrm{T}}{\underline{Z}_1^2 + 2\underline{Z}_1\underline{Z}_3 + \underline{Z}_1\underline{Z}'_\mathrm{T}} \tag{F.6a}$$

$$\underline{Z}'_{23} = \frac{\left(\underline{Z}_1^2 + 2\underline{Z}_1\underline{Z}_3\right)R_\mathrm{load}}{\underline{Z}_1^2 + 2\underline{Z}_1\underline{Z}_3 + \underline{Z}_1 R_\mathrm{load}} \tag{F.6b}$$

$$\underline{Z}'_{13} + \underline{Z}'_{23} = \frac{\left(\underline{Z}_1^2 + 2\underline{Z}_1\underline{Z}_3\right)^2\left(\underline{Z}'_\mathrm{T} + R_\mathrm{load}\right) + 2\left(\underline{Z}_1^2 + 2\underline{Z}_1\underline{Z}_3\right)\underline{Z}_1\underline{Z}'_\mathrm{T}R_\mathrm{load}}{\left(\underline{Z}_1^2 + 2\underline{Z}_1\underline{Z}_3 + \underline{Z}_1\underline{Z}'_\mathrm{T}\right)\left(\underline{Z}_1^2 + 2\underline{Z}_1\underline{Z}_3 + \underline{Z}_1 R_\mathrm{load}\right)}$$

The total generator impedance yields:

$$\underline{Z}_\mathrm{G} = \frac{\left(\underline{Z}_1^2 + 2\underline{Z}_1\underline{Z}_3\right)\left(\underline{Z}'_\mathrm{T} + R_\mathrm{load}\right) + 2\underline{Z}_1\underline{Z}'_\mathrm{T}R_\mathrm{load}}{\underline{Z}_1^2 + 2\underline{Z}_1\underline{Z}_3 + \left(\underline{Z}_1 + \underline{Z}_3\right)\left(\underline{Z}'_\mathrm{T} + R_\mathrm{load}\right) + \underline{Z}'_\mathrm{T}R_\mathrm{load}} \tag{F.7}$$

G Bunch profile and bunch spectrum

The beam current, as it is observed at a fixed location $z = 0$ along the circumference, is described by a FOURIER series expansion with the spectral components $\underline{I}_n$. T_0 corresponds to the revolution period according $T_0 = 2\,R_{\text{syn}}/v$:

$$I(t) = \sum_{n=-\infty}^{\infty} \underline{I}_n e^{jn\frac{2\pi}{T_0}t} \tag{G.1a}$$

$$= \sum_{n=-\infty}^{\infty} \underline{I}_n e^{jn\omega_0 t} \tag{G.1b}$$

For an arbitrary location $z \in \left[0, L_{\text{syn}}\right]$, the previous expression changes into:

$$I(z,t) = I(t - \tfrac{z}{v}) \tag{G.1c}$$

$$= \sum_{n=-\infty}^{\infty} \underline{I}_n e^{jn\omega_0\left(t-\frac{z}{v}\right)} \tag{G.1d}$$

The coefficients $\underline{I}_n$ are calculated as:

$$\underline{I}_n = \frac{1}{T_0} \int_{-T_0/2}^{T_0/2} I(t) e^{-jn\omega_0 t}\,\mathrm{d}t \tag{G.1e}$$

Consequently, the frequency domain representation of equation G.1c reads:

$$
\begin{aligned}
\underline{I}(z,\omega) &= \int_{-\infty}^{\infty} I(z,t)e^{-j\omega t}\,\mathrm{d}t && \text{(G.2a)}\\
&= \int_{-\infty}^{\infty} I(t-\tfrac{z}{v})e^{-j\omega t}\,\mathrm{d}t \\
&= \int_{-\infty}^{\infty} \sum_{n=-\infty}^{\infty} \underline{I}_n e^{jn\omega_0\left(t-\frac{z}{v}\right)}e^{-j\omega t}\,\mathrm{d}t \\
&= \sum_{n=-\infty}^{\infty} \underline{I}_n e^{-j\omega_n\frac{z}{v}} \underbrace{\int_{-\infty}^{\infty} e^{-j(\omega-\omega_n)t}\,\mathrm{d}t}_{} \\
&= \sum_{n=-\infty}^{\infty} \underline{I}_n e^{-j\omega_n\frac{z}{v}} \quad \delta(\omega-\omega_n) && \text{(G.2b)}
\end{aligned}
$$

Equations G.1c and G.1c are of general nature and valid for arbitrary signals $I(t)$. For the operation of the SIS100 *parabolic* bunch profiles represent a convenient approximation and are therefore of special interest. A single bunch with parabolic profile is given as:

$$
I_{\mathrm{b}}(t) = \begin{cases} I_0 - I_2^2 t^2 & \text{, for } |t| \leq \sqrt{I_0/I_2} \\ 0 & \text{, for } |t| > \sqrt{I_0/I_2} \end{cases} \tag{G.3}
$$

$T_{\mathrm{b}} = 2\sqrt{I_0/I_2}$ equals the bunch length that is duration. A train of N_{b} equidistantly spaced bunches is obtained by periodic continuation. The bunches are located at $t - mT_{\mathrm{i}}$ with $m \in \mathbb{N}_0^{\leq N_{\mathrm{b}}-1}$ and the inter-bunch distance $T_{\mathrm{i}} = T_0/N_{\mathrm{b}}$:

$$
I(t) = \sum_{m=0}^{N_{\mathrm{b}}-1} I_{\mathrm{b}}(t - m \underbrace{\tfrac{T_0}{N_{\mathrm{b}}}}_{T_{\mathrm{i}}}) \tag{G.4}
$$

The Fourier coefficients for the bunch train are calculated as:

$$\underline{I}_n = \frac{1}{T_0} \int\limits_{-T_0/2}^{T_0/2} I(t) e^{-j\omega_n t}\, \mathrm{d}t = \frac{1}{T_0} \int\limits_{-T_0/2}^{T_0/2} \sum_{m=0}^{N_\mathrm{b}-1} I_\mathrm{b}(t - mT_\mathrm{i}) e^{-j\omega_n t}\, \mathrm{d}t \tag{G.5a}$$

$$= \frac{1}{T_0} \sum_{m=0}^{N_\mathrm{b-1}} e^{-j\omega_n m T_\mathrm{i}} \int\limits_{-T_0/2N_\mathrm{b}}^{T_0/2N_\mathrm{b}} I_\mathrm{b}(t) e^{-j\omega_n t}\, \mathrm{d}t \tag{G.5b}$$

$$= \frac{1}{T_0} \sum_{m=0}^{N_\mathrm{b-1}} \sum_k e^{-j\omega_n m T_\mathrm{i}} \frac{T_0}{N_\mathrm{b}} \delta_{n,kN_\mathrm{b}} \underline{I}_{\mathrm{b},k} = \sum_k \delta_{n,kN_\mathrm{b}} \underline{I}_{\mathrm{b},k} \text{ , and } k \in \mathbb{Z} \tag{G.5c}$$

Thus, the FOURIER coefficients are calculated with the help of $I_\mathrm{b}(t)$. For the parabolic bunch according equation G.3 this reads:

$$\underline{I}_{\mathrm{b},k} = \frac{1}{\Omega_k^3} \left(-4 I_2 T_\mathrm{b} \Omega_k \cos(T_\mathrm{b}\Omega_k) + 2\left(I_0 \Omega_k^2 + I_2\left(2 - T_\mathrm{b}^2 \Omega_k^2\right)\right) \sin(T_\mathrm{b}\Omega_k)\right) \tag{G.6}$$

The abbreviation $\Omega_k = k N_\mathrm{b} \omega_0$ has been used.

H Datasheets

H.1 Material specifications

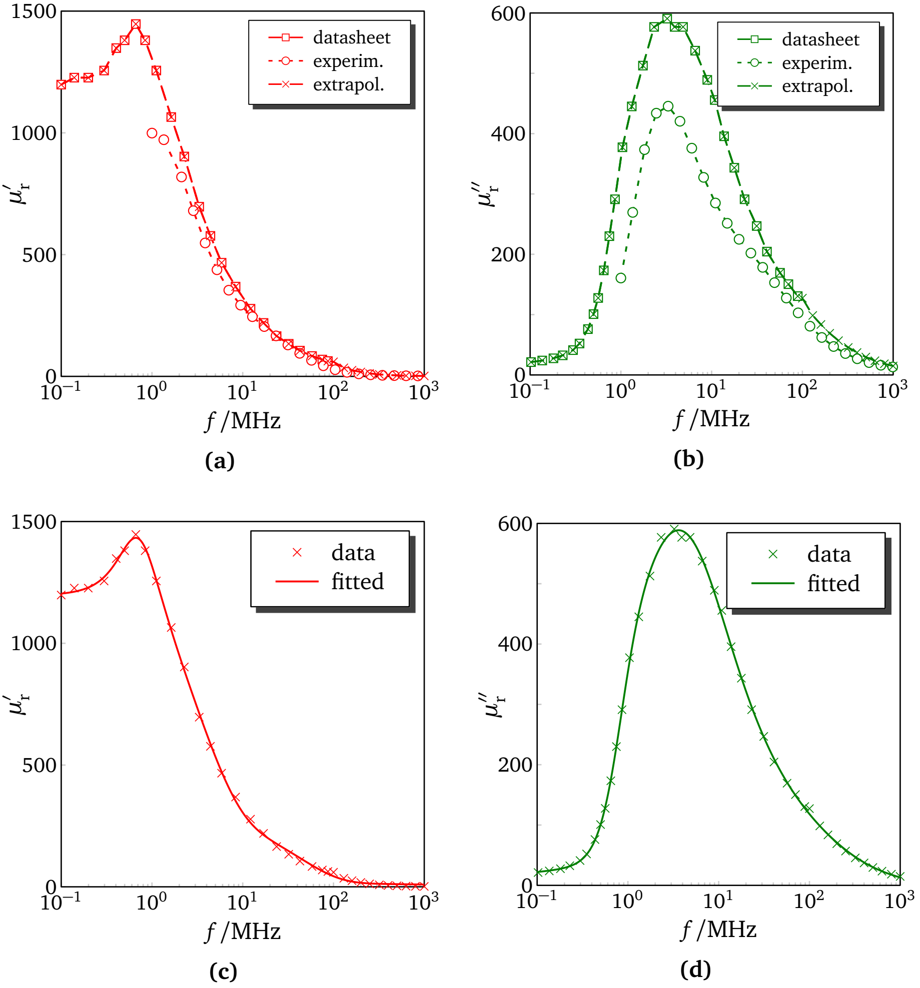

(a) (b) (c) (d)

Figure H.1.: The values plotted in figures (a) and (b) originate from manufacturer datasheets [45]. Values above 100MHz have been extrapolated. The experimental data is listed for comparison and originates from measurements that have been performed at European Organization for Nuclear Research (CERN) using a ferrite loaded waveguide [11]. The curves plotted in figures (c) and (d) present a least squares fit for the extrapolated data and serve as reference for all purposes of this work.

I Register

Acronyms

2D	Two dimensional
3D	Three dimensional
CAD	Computer Aided Design
CERN	European Organization for Nuclear Research
CFL	COURANT-FRIEDRICHS-LEVY
DTFT	Discrete-Time FOURIER Transform
DUT	Device Under Test
EM	Electromagnetic
FAIR	Facility for Antiproton and Ion Research GmbH
FD	Frequency Domain
FDTD	Finite Difference Time Domain
FIT	Finite Integration Technique
GSI	Helmholtz Center for Heavy Ion Research GmbH
LHS	Left Hand Side
MMF	Magnetomotive Force
ODE	Ordinary Differential Equation
PDE	Partial Differential Equation
PEC	Perfect Electric Conductor
PFN	Pulse Forming Network
PIC	Particle-In-Cell
PMC	Perfect Magnetic Conductor

PML	Perfectly Matched Layer
RF	Radio Frequency
RHS	Right Hand Side
RMS	Root Mean Square
SIS	Heavy Ion Synchrotron
SPICE	Simulation Program with Integrated Circuit Emphasis
TD	Time Domain
TEM	Transverse Electromagnetic
TM	Transverse Magnetic
UNILAC	UNIversal Linear ACcelerator

Coordinate systems

x	m	x- coordinate
y	m	x- coordinate
z	m	z- coordinate
$\vec{e}_x$		horizontal unit vector
$\vec{e}_y$		vertical unit vector
$\vec{e}_z$		longitudinal unit vector
ϱ	m	ϱ- coordinate
φ	rad	φ- coordinate
$\vec{e}_\varrho$		radial unit vector
$\vec{e}_\varphi$		azimuthal unit vector
$\vec{e}_{\vert\vert}$		longitudinal unit vector
$\vec{e}_\perp$		transverse unit vector
$\vec{n}$		normal unit vector
$\vec{r}$	m	position vector
$\vec{r}_{\vert\vert}$	m	longitudinal position vector, $\vec{r}_{\vert\vert} = z\vec{e}_z$
$\vec{r}_\perp$	m	transverse position vector, $\vec{r}_\perp = x\vec{e}_x + y\vec{e}_y = \varrho\vec{e}_\varrho$

Electrodynamics

$\vec{E}, \underline{\vec{E}}$	V/m	electric field intensity and phasor representation
$\vec{D}, \underline{\vec{D}}$	C/m^2	electric displacement and phasor representation
$\vec{H}, \underline{\vec{H}}$	A/m	magnetic field intensity and phasor representation
$\vec{B}, \underline{\vec{B}}$	T	magnetic induction and phasor representation
$\vec{J}, \underline{\vec{J}}$	A/m^2	current density and phasor representation
$\vec{M}$	A/m	magnetization
$\vec{P}$	C/m^2	polarization density
$\vec{S}, \underline{\vec{S}}$	W/m^2	Poynting vector and phasor representation
$\Phi_{mag}, \underline{\Phi}_{mag}$	Wb	magnetic flux linkage
Φ	V	scalar potential
Q	C	charge

q_V, $\underline{q}_V$	C/m^3	volume charge density
q_A, $\underline{q}_A$	C/m^2	surface charge density
q_L, $\underline{q}_L$	C/m	line charge density
$q_\perp$, $\underline{q}_\perp$	C/m^2	transverse charge distribution
$q_{\|\|}$, $\underline{q}_{\|\|}$	1/m	longitudinal distribution

p_ε	W/m^3	dielectric loss density
p_κ	W/m^3	resistive loss density
p_κ	W/m^3	magnetic loss density
$\bar{w}_E$	Ws/m^3	time-averaged electric energy density
$\bar{w}_H$	Ws/m^3	time-averaged magnetic energy density
P_ε	W	dielectric loss
P_κ	W	resistive loss
P_μ	W	magnetic loss
$\varepsilon_\mathbf{r}$, $\underline{\varepsilon}_\mathbf{r}$		relative permittivity
$\varepsilon'_\mathbf{r}$		real part of the complex relative permittivity, $\varepsilon'_\mathrm{r} = \mathrm{Re}\left\{\underline{\varepsilon}_\mathrm{r}\right\}$
$\varepsilon''_\mathbf{r}$		imag. part of the complex rel. permittivity, $\varepsilon''_\mathrm{r} = \mathrm{Im}\left\{\underline{\varepsilon}_\mathrm{r}\right\}$
$\mu_\mathbf{r}$, $\underline{\mu}_\mathbf{r}$		relative permeability
$\mu'_\mathbf{r}$		real part of the complex relative permeability, $\mu'_\mathrm{r} = \mathrm{Re}\left\{\underline{\mu}_\mathrm{r}\right\}$
$\mu''_\mathbf{r}$		imag. part of the complex rel. permeability, $\mu''_\mathrm{r} = \mathrm{Im}\left\{\underline{\mu}_\mathrm{r}\right\}$

ω	rad/s	angular frequency, $\omega = 2\pi f$
t	s	time (lab frame)
$\vec{F}_E$	N	electric force
$\vec{F}_\mathbf{L}$	N	Lorentz force, $\vec{F}_\mathrm{L} = \vec{F}_E + \vec{F}_B$
$\Delta\vec{p}$	Ns	impulse
$\vec{F}_B$	N	magnetic force
$\vec{p}$	Ns	momentum, $\vec{p} = m\vec{v}$

k_z	1/m	wave number

β		relative particle velocity
γ		Lorentz factor, $\gamma = \sqrt{1-\beta^2}^{\,-1}$
v	m/s	nominal particle velocity

General

$\delta(r)$	1/m	Dirac delta distribution in 1D position space, $r \in \mathbb{R}$
$\delta(\vec{r}_\perp)$	$1/\mathrm{m}^2$	Dirac delta distribution in 2D position space, $\vec{r}_\perp \in \mathbb{R}^2$
$\delta(\vec{r})$	$1/\mathrm{m}^3$	Dirac delta distribution in 3D position space, $\vec{r} \in \mathbb{R}^3$
δ_{m0}		Kronecker delta distribution, $m \in \mathbb{N}_0$
$\mathfrak{F},\ \mathfrak{F}^{-1}$		Fourier transform, inverse Fourier transform
$\mathfrak{G}$		Green function
$\Theta(\vec{r})$		Heaviside step function
$J_m(u),\ N_m(u)$		ordinary Bessel functions of 1st and 2nd kind
$\underline{I}_m(u),\ \underline{K}(u)$		modified Bessel functions of 1st and 2nd kind
$\underline{H}_m^{(1)}(u),\ \underline{H}_m^{(2)}(u)$		Hankel functions of 1st and 2nd kind
j		imaginary unit, $j = \sqrt{-1}$
$\mathfrak{L}$		linear differential Operator
Δ		Laplace operator, $\Delta = \nabla^2$
$\mathcal{O}$		Landau symbol
$\Delta_\perp$		transverse Laplace operator, $\Delta_\perp = \Delta - \frac{\partial^2}{\partial z^2}$
∇		nabla operator
$\mathbb{C}$		complex numbers
$\mathbb{N},\ \mathbb{N}_0$		natural numbers, natural numbers including 0
$\mathbb{R}$		real numbers
$\mathbb{Z}$		whole numbers

Electrical Engineering

f_0	Hz	frequency of 0th order harmonic
f_n	Hz	frequency of nth order harmonic, $f_n = nf_0$
$\underline{I}_n$	As	Fourier component of nth order
$I,\ \underline{I}$	A	current
$I_\mathbf{b}$	A	bunch current
$I_\mathbf{beam}$	A	beam current

$L_{\mathbf{bunch}}, L_{\mathbf{b}}$	m	(RMS) bunch length (distance)
$L_{\mathbf{syn}}$	m	nominal circumference of the synchrotron, $L_{\text{syn}} = 2\pi R_{\text{syn}}$
$R_{\mathbf{syn}}$	m	nominal radius of the synchrotron
$N_{\mathbf{b}}$		number of bunches
$N_{\mathbf{i}}$		number of ions per bunch
ω_0	rad/s	angular frequency of 0^{th} order harmonic, $\omega_0 = 2\pi f_0$
ω_n	rad/s	angular frequency of n^{th} order harmonic, $\omega_n = n\omega_0$
$Q_{\mathbf{beam}}$	C	beam charge
$Q_{\mathbf{bunch}}, Q_{\mathbf{b}}$	C	bunch charge
σ_z	m	standard deviation for GAUSSian bunch
M	H	mutual inductance
$\underline{S}_{11}$		input voltage reflection coefficient
$\underline{S}_{12}$		reverse voltage gain
$\underline{S}_{21}$		forward voltage gain
$\underline{S}_{22}$		output port voltage reflection coefficient
$\underline{\gamma}_{\mathbf{line}}$	Ω/m	propagation constant, $\underline{\gamma}_{\text{line}} = \sqrt{(R' + j\omega L')(G' + j\omega C')}$
λ	m	wavelength
θ_L	m	electrical length, $\theta_L = 2\pi L/\lambda$
T_0	s	period of 0^{th} order harmonic, $T_0 = 1/f_0$
T_n	s	period of n^{th} order harmonic, $T_n = nT_0$
$U, \underline{U}$	V	voltage
$W_{\mathbf{kin}}$	eV	kinetic energy

Wakefields and Coupling Impedances

$\underline{Z}_{\|\|}$	Ω	longitudinal coupling impedance
$\underline{Z}_{\perp}$	Ω/m	transverse coupling impedance
$\underline{Z}_{x}$	Ω/m	transverse horizontal coupling impedance
$\underline{Z}_{y}$	Ω/m	transverse vertical coupling impedance
$L_{\mathbf{wake}}$	m	wake length
d_x	m	beam displacement in x-direction
d_y	m	beam displacement in y-direction
$G_{\|\|},\ G_z$	V/C	longitudinal component of the wake function
$G_{\perp}$	V/C/m	transverse component of the wake function
G_x	V/C/m	horizontal horizontal component of the wake function
G_y	V/C/m	transverse vertical component of the wake function
$W_{\|\|},\ W_z$	V	longitudinal component of the wake potential
$W_{\perp}$	V/m	transverse component of the wake potential
W_x	V/m	horizontal horizontal component of the wake potential
W_y	V/m	transverse vertical component of the wake potential

Physical constants

c_0	m/s	velocity of light in vacuum, $c_0 = \sqrt{\varepsilon_0\mu_0}^{-1}$
ε_0	As/Vm	vacuum permittivity, $\varepsilon_0 = 8.854...\ 10^{-12}$As/Vm
μ_0	Vs/Am	vacuum permeability, $\mu_0 = 1.256...\ 10^{-6}$Vs/Am
Z_0	Ω	characteristic impedance of vacuum, $Z_0 = \sqrt{\mu_0/\varepsilon_0} = \mu_0 c_0 = (\varepsilon_0 c_0)^{-1} = 376.730...\ \Omega$

Computational Electrodynamics FIT notation

$\overset{\frown}{\mathbf{e}}$	V	electric grid voltage
$\overset{\frown}{\overset{\frown}{\mathbf{d}}}$	C	electric grid flux
$\overset{\frown}{\mathbf{h}}$	A	magnetic grid voltage
$\overset{\frown}{\overset{\frown}{\mathbf{b}}}$	Wb	magnetic grid flux
$\overset{\frown}{\overset{\frown}{\mathbf{j}}}$	A	grid current
$\mathbf{q}$	C	vector of discrete grid charge
$\mathbf{C}$, $\widetilde{\mathbf{C}}$		discrete curl operators on primary and dual grid
$\mathbf{M}_\varepsilon$		permittivity matrix
$\mathbf{M}_\mu$		permeability matrix
Δx	m	grid spacing in x- direction
Δy	m	grid spacing in y- direction
Δz	m	grid spacing in z- direction
N_x, N_y, N_z		number of gridpoints in x-, y- and z- direction
i, j, k		grid coordinate in x-, y- and z- direction
N_P		total number of gridpoints
n		grid point index
N_V		total number of gridpoints
α_t		time step reduction factor

Textbook references

[AS72] Milton Abramowitz and Irene Stegun. *Handbook of Mathematical Functions*. Dover Publications, 9th edition, 1972.

[Hin08] Frank Hinterberger. *Physik der Teilchenbeschleuniger und Ionenoptik*. Springer, 2nd edition, 2008.

[ITvM04] Ellen Ivers-Tiffee and Waldemar von Münch. *Werkstoffe der Elektrotechnik*. B. G. Teubner Verlag, 9th edition, 2004.

[Jac99] John David Jackson. *Classical Electrodynamics*. John Wiley & Sons, Inc., 3rd edition, 1999.

[Ng06] K. Y. Ng. *Physics of Intensity Dependent Beam In*. World Scientific, 1st edition, 2006.

[Saa03] Yousef Saad. *Iterative methods for sparse linear systems*. Siam, 2nd edition, 2003.

[SG09] Michael Stone and Paul Goldbart. *Mathematics for Physics*. Cambridge University Press, 1st edition, 2009.

[Wil96] Klaus Wille. *Physik der Teilchenbeschleuniger und Synchrotronstrahlungsquellen*. B. G. Teubner Verlag, 2nd edition, 1996.

[ZK98] Bruno W. Zotter and Semyon A. Kheifets. *Impedances and wakes in high-energy particle accelerators*. World Scientific, 1st edition, 1998.

Reports and paper references

[1] W. Ackermann, M. Krassilnikov, T. Weiland, W. Beinhauer, H.-D. Gräf, and A. Richter, “Simulation of particle dynamics in accelerators using the Ensemble Model,” in *Proceedings of the Particle Accelerator Conference*, 2003.

[2] A. M. Al-khateeb, “private communication.”

[3] A. M. Al-khateeb, R. W. Hasse, and O. Boine-Frankenheim, “Comparison of the longitudinal coupling impedance from different source terms,” *Nuclear Instruments and Methods in Physics Research Section A: Accelerators, Spectrometers, Detectors and Associated Equipment*, vol. 593, no. 3, pp. 171–176, 2008.

[4] S. Appel, “Simulation und Messung longitudinaler Raumladungseffekte in intensiven Ionenstrahlen im SIS18 Synchrotron,” Ph.D. dissertation, Technische Universität Darmstadt, 2011.

[5] M. C. Balk, “Feldsimulation starrer Teilchenstrahlen beliebiger Geschwindigkeit und deren Anwendung in der Schwerionenbeschleunigerphysik,” Ph.D. dissertation, Technische Universität Darmstadt, 2005.

[6] U. Blell, “private communication.”

[7] ——, “Measurement of the kicker coupling impedances in the SIS and ESR at GSI,” in *Proceedings of the Particle Accelerator Conference*, 1997.

[8] O. Boine-Frankenheim, “The FAIR accelerators: highlights and challenges,” in *Proceedings of the International Particle Accelerator Conference*, 2010.

[9] F. Caspers, “Bench methods for beam coupling impedance measurements,” CERN, Tech. Rep., 1992.

[10] F. Caspers, D. Möhl, and A. Schwinn, “A new bench method to simulate electromagnetic fields of slow beams,” in *Proceedings of the Particle Accelerator Conference*, 1990.

[11] F. Caspers, M. Morvillo, C. Gonzalez, and M. D’yachkov, “Measurements of complex permeability and permittivity of ferrites for the LHC injection kicker,” CERN, Tech. Rep., 1999.

[12] P. J. Channell, “The Moment Approach to charged particle beam dynamics,” *IEEE Transactions on Nuclear Science*, vol. 30, no. 4, p. 2607, 1983.

[13] M. Clemens, R. Schumann, and T. Weiland, “Algebraic properties and conservation laws in the Discrete Electromagnetism,” *Frequenz*, vol. 53, no. 11-12, pp. 219–225, 1999.

[14] M. Dehler, “Numerische Lösung der Maxwellschen Gleichungen auf kreiszylindrischen Gittern,” Ph.D. dissertation, Technische Universität Darmstadt, 1993.

[15] S. DeSantis, “Analysis of coupling impedance bench measurements using Bethe’s Diffraction Theory,” in *Proceedings of the Particle Accelerator Conference*, 2001.

[16] B. Doliwa, E. Arevalo, and T. Weiland, “Numerical calculation of transverse coupling impedances: Comparison to Spallation Neutron Source extraction kicker measurements,” *Physical Reviev Special Topics - Accelerators and Beams*, vol. 10, 2007.

[17] B. Doliwa and T. Weiland, “Numerical calculation of coupling impedances in kicker modules for non-relativistic particle beams,” in *Proceedings of the* 22^{rd} *Linear Accelerator Conference*, 2004.

[18] A. Faltens, E. C. Hartwig, D. Möhl, and A. M. Sessler, “Analog method for measuring the longitudinal coupling impedance of a relativistic particle beam with its environment,” in *Proceedings of the 8th International Conference on High- Energy Accelerators*, 1971.

[19] R. Fedele and V. G. Vaccaro, “The kicker coupling impedance,” INFN, Tech. Rep., 1991.

[20] R. L. Gluckstern, “Analytic methods for calculating coupling impedances,” CERN, Tech. Rep., 2000.

[21] R. L. Gluckstern and R. Li, “Analysis of coaxial wire measurement of longitudinal coupling impedance,” *Particle Accelerators*, vol. 29, pp. 159–165, 1990.

[22] S. Gutschling, “Zeitbereichsverfahren zur Simulation elektromagnetischer Felder in dispersiven Materialien,” Ph.D. dissertation, Technische Universität Darmstadt, 1998.

[23] H. Hahn, “On the validity of coupling impedance bench measurements,” BNL / SNS, Tech. Rep., December 2000.

[24] ——, “Interpretation of coupling impedance bench measurements,” BNL / SNS, Tech. Rep., 2003.

[25] ——, “Matrix solution for the wall impedance of infinitely long multilayer circular beam tubes,” *Physical Reviev Special Topics - Accelerators and Beams*, vol. 13, pp. 012 002–1–12 002–12, August 2010.

[26] H. Hahn and F. Pedersen, “On the coaxial wire measurements of the longitudinal coupling impedance,” BNL, Tech. Rep., 1978.

[27] P. Hammes, “Zur numerischen Berechnung von Streumatrizen im Hochfrequenzbereich,” Ph.D. dissertation, Technische Universität Darmstadt, 1999.

[28] E. Jensen, “An improved log-formula for homogenously distributed impedance,” CERN, Tech. Rep., 2000.

[29] T. Lau, “Numerische Methoden zur Simulation teilchengenerierter elektromagnetischer Felder in der Beschleunigerphysik,” Ph.D. dissertation, Technische Universität Darmstadt, 2006.

[30] E. Metral, “Resistive-wall impedance of an infinitely long multi-layer cylindrical pipe,” in *Proceedings of the Particle Accelerator Conference*, 2007.

[31] N. Mounet and E. Metral, “Electromagnetic field created by a macroparticle in an infinitely long and axisymmetric multilayer beam pipe,” CERN, Tech. Rep., 2009.

[32] G. Nassibian and F. Sacherer, “Methods for measuring transverse coupling impedances in circular accelerators,” *Nucl. Instrum. Meth.*, vol. 159, pp. 21–27, 1979.

[33] T. Oki, “The bridged-T network lumped kicker: A novel fast magnetic kicker system for a compact synchrotron,” *Nuclear Instruments and Methods in Physics Research Section A: Accelerators, Spectrometers, Detectors and Associated Equipment*, vol. 607, no. 3, pp. 489 – 497, 2009.

[34] W. K. H. Panofsky and W. A. Wenzel, “Some considerations concerning the transverse deflection of charged particles in radio-frequency fields,” *Review of Scientific Instruments*, vol. 27, pp. 967–968, 1956.

[35] S. Paret, “Transverse Schottky Spectra and Beam Transfer Functions of coasting ion beams with Space Charge,” Ph.D. dissertation, Technische Universität Darmstadt, 2010.

[36] A. Piwinsky, “Penetration of the field of a bunched beam through a ceramic vacuum chamber with metallic coating,” *IEEE Transactions on Nuclear Science*, vol. 24, no. 3, pp. 1364–1366, 1977.

[37] ——, “Wake fields and ohmic losses in round vacuum chambers,” DESY, Tech. Rep., 1992.

[38] K. Samuelsson, V. Hinrichsen, U. Blell, and P. Spiller, “Impedance of the pulse power converter for the SIS100 bipolar extraction kicker system,” in *Proceedings of the International Particle Accelerator Conference*, 2011.

[39] M. Sands and J. R. Rees, “A bench measurement of the energy losses of a stored beam to a cavity,” SLAC, Tech. Rep., 1974.

[40] K. Schindl, “Space charge,” CERN, Tech. Rep., 2000.

[41] R. Schuhmann and T. Weiland, “Conservation of Discrete Energy and related laws in the Finite Integration Technique,” *Progress in Electromagnetic Research*, vol. 32, pp. 301–316, 2001.

[42] R. Schumann, “Die nichtorthogonale Finite-Integrations-Methode zur Simulation elektromagnetischer Felder,” Ph.D. dissertation, Technische Universität Darmstadt, 1999.

[43] `www.cst.com`.

[44] `www.draka.com`.

[45] `www.ferroxcube.com`.

[46] `www.spectrum-soft.com`.

[47] P. Thoma, “Zur numerischen Lösung der Maxwellschen Gleichungen im Zeitbereich,” Ph.D. dissertation, Technische Universität Darmstadt, 1997.

[48] H. Tsutsui and L. Vos, “Transverse coupling impedance of a simplifed ferrite kicker magnet model,” CERN, Tech. Rep., 2000.

[49] H. Tsutsui, “Longitudinal impedances of some simplified ferrite kicker magnet models,” CERN, Tech. Rep., 2000.

[50] ——, "Some simplified models of ferrite kicker magnet for calculation of longitudinal coupling impedance," CERN, Tech. Rep., 2000.

[51] V. G. Vaccaro, "Longitudinal instabilitiy of a coasting beam above transition due to the action of lumped discontinuities," CERN, Tech. Rep., 1966.

[52] S. Vaganian and H. Henke, "The Panofsky-Wenzel theorem and general relations for the wake potential," *Particle Accelerators*, vol. 48, pp. 239–242, 1995.

[53] L. S. Walling, D. E. McMurry, D. V. Neuffer, and H. A. Thiesse, "Transmission-line impedance measurements for an advanced hadron facility," *Nuclear Instruments and Methods in Physics Research Section A: Accelerators, Spectrometers, Detectors and Associated Equipment*, vol. 281, pp. 433–447, 1989.

[54] T. Weiland, "A discretization method for the solution of Maxwell's equations for six-component fields," *Electronics and Communication (AEUE)*, vol. 31, no. 3, pp. 116–120, 1977.

[55] ——, "Advances in FIT / FDTD Modeling," in *Review of Progress in Applied Computational Electromagnetics*, 2002.

[56] T. Wietoska, "Optimierung der Ansteuerung von Ablenkmagneten in Teilchenbeschleunigern unter besonderer Berücksichtigung halbleiterbasierter Lösungen," Ph.D. dissertation, Technische Universität Darmstadt, 2008.

[57] K. S. Yee, "Numerical solution of initial boundary value problems involving Maxwell's equations in isotropic media," *IEEE Transactions on Antennas and Propagation*, vol. 14, pp. 302–307, 1966.

Own publications

[58] A. Al-khateeb, O.Boine-Frankenheim, A. Plotnikov, S. Yeub, and L. Haenichen, “Longitudinal impedance of a step-in for a round beam at arbitrary beam energy,” *Nuclear Instruments and Methods in Physics A*, vol. 626-627, pp. 1–7, 2011.

[59] L. Haenichen, “Enhancement of light extraction from OLEDs using gel layers with excavations,” US Patent 11 159 739, 2005.

[60] ——, “Application of time and frequency domain methods for coupling impedance calculation,” in *Proceedings of the 10th International Computational Accelerator Physics Conference*, San Francisco, CA, USA, 2009.

[61] ——, “Comparison of analytical and numerical methods results for broadband coupling impedance,” in *Proceedings of the 23rd Particle Accelerator Conference*, Vancouver, BC, Canada, 2009.

[62] L. Haenichen, O. Boine-Frankenheim, W. F. O. Mueller, and T. Weiland, “Calculation of beam coupling impedance for ferrite devices: theory und simulation,” in *Verhandlungen der 74. Frühjahrstagung der Deutschen Physikalischen Gesellschaft*, Bonn, Germany, 2010.

[63] ——, “Coupling impedance contribution of ferrite devices: theory and simulation,” in *Proceedings of the 1st International Particle Accelerator Conference*, Kyoto, Japan, 2010.

[64] L. Haenichen and F. Pschenitzka, “Using prismatic microstructured films for image blending in OLEDs,” US Patent 7 586 245, 2005.

[65] Y. W. Kang, A. Vassioutchenko, A. Aleksandrov, M. Champion, M. Champion, M. Crofford, P. Gibson, L. Haenichen, T. Hardek, P. Ladd, M. McCarthy, and D. Stout, “Development of an RFQ input power coupling system,” in *Proceedings of the 23rd Linear Accelerator Conference*, Knoxville, TN, USA, 2006.

Acknowledgement

At this point I would like to express my gratitude to all colleagues, friends and family, for enduring support, patience and understanding. In particular I would like to mention:

- Prof. Thomas Weiland for the scientific support, helpful advice and excellent working conditions with enjoyable atmosphere.
- Prof. Harald Klingbeil for his willingness to act as second examiner.
- Prof. Oliver Boine-Frankenheim for establishing contact to the GSI and CERN through workshops and exchange.
- Dr. Wolfgang F. O. Müller for sharing his knowledge about particle accelerators and helpful advice.
- Dr. Burkhard Doliwa, Dr. Erion Gjonaj and Dr. Stephan Koch for their assistance with regard to numerical methods and coding.
- Dr. Thomas Lau and Dr. Ahmed Al-khateeb for giving valuable insights into particle beam related electrodynamics.
- Dr. Benoit Salvant and the impedance theory group at CERN for discussion and exchange.
- Dr. Monica Balk and the CST support team for their unhesitant effort in answering my questions.
- Dipl.-Ing. Dragos Munteanu and Heike Seiler for tireless IT support and taking care of organizational matters.
- my office mates at TEMF Dr. Bastian Steiner, Dr. Peter Scholz and Dr. Todorka Banova for their company, enduring encouragement and relaxed atmosphere.
- my dear family and friends for their continued patience and support.
- the GSI and BMBF for funding.

Curriculum Vitae

Personal data

Full name : Harald Lukas Hänichen

Date of birth : 17th March, 1979
Place of birth : Dresden

Education and professional background

8/2012 - current	**Employee / Research and Development** Bruker BioSpin GmbH Permanent & Resistive Magnet R&D
2/2007 - 2/2012	**Research associate / doctoral candidate** Institut für Theorie Elektromagnetischer Felder Technische Universität Darmstadt *Calculation of beam coupling impedances for synchrotron accelerators*
1/2007	**Graduation as Diplomingenieur der Elektrotechnik** *Investigations on higher order mode couplers for the SNS superconducting cavities*
2/2006 - 9/2006	**Research visitor at Oak Ridge National Laboratory** Spallation Neutron Source, Oak Ridge, USA
10/2004 - 3/2005	**Internship at OSRAM Opto Semiconductors** OLED R&D Department, San Jose, USA
9/1999	**Enrollment as student at the TU Darmstadt** Elektrotechnik und Informationstechnik
10/1998 - 8/1999	**Military service at the German armed forces**
6/1998	**High school graduation** Christian Wirth Schule, Usingen